CANADIAN THESES

THÈSES CANADIENNES

NOTICE

The quality of this microfiche is heavily dependent upon the quality of the original thesis submitted for microfilming. Every effort has been made to ensure the highest quality of reproduction possible.

If pages are missing, contact the university which granted the degree.

Some pages may have indistinct print especially if the original pages were typed with a poor typewriter ribbon or if the university sent us an inferior photocopy.

Previously copyrighted materials (journal articles, published tests, etc.) are not filmed.

Reproduction in full or in part of this film is governed by the Canadian Copyright Act, R.S.C. 1970, c. C-30. Please read the authorization forms which accompany this thesis.

AVIS

La qualité de cette microfiche dépend grandement de la qualité de la thèse soumise au microfilmage. Nous avons tout fait pour assurer une qualité supérieure de reproduction.

S'il manque des pages, veuillez communiquer avec l'université qui a conféré le grade.

La qualité d'impression de certaines pages peut laisser à désirer, surtout si les pages originales ont été dactylographiées à l'aide d'un ruban usé ou si l'université nous a fait parvenir une photocopie de qualité inférieure.

Les documents qui font déjà l'objet d'un droit d'auteur (articles de revue, examens publiés, etc.) ne sont pas microfilmés.

La reproduction, même partielle, de ce microfilm est soumise à la Loi canadienne sur le droit d'auteur, SRC 1970, c. C-30. Veuillez prendre connaissance des formules d'autorisation qui accompagnent cette thèse.

THIS DISSERTATION
HAS BEEN MICROFILMED
EXACTLY AS RECEIVED

LA THÈSE A ÉTÉ
MICROFILMÉE TELLE QUE
NOUS L'AVONS REÇUE

Canada

CORRECTION OF FLUCTUATING PRESSURE IN PNEUMATIC TUBINGS AND ITS APPLICATION TO A BUILDING MODEL

by

NAZMI LAWEN

A thesis
presented to the University of Ottawa
in partial fulfillment of the
requirements for the degree of
Master of Applied Sciences
in
Departement of Civil Engineering

OTTAWA, Ontario, 1984

ABSTRACT

The use of pneumatic tubings for the pressure study in wind engineering projects is an unavoidable element which introduces the problem of distorting the measured fluctuating pressure signals. In order to regulate this distortion, it is necessary to obtain a near unity amplitude transfer function and a linear phase transfer function with frequency between the pressure at the model taps and the pressure measured by the remote transducer.

Methods for measuring and correcting the transfer function have been discussed in detail in Part I of this study. A new technique has been developed at the NAE/NRCC involving an equipment to correct the signal digitally using the known transfer function of the tubing. This technique is used in this study to correct the transfer functions of standard pvc tubes of various lengths and the experimental results have been checked with existing theory. Also a parametric analysis for a single pressure measuring system is presented to demonstrate the influence of various parameters on the transfer function. The technique is found to be effective in eliminating the resonant peaks in the transfer functions for tubes of various lengths. Also the theory is found to predict the transfer function with a high degree of accuracy.

In Part II of this study, a 1:1000 scaled model of the CAARC standard tall building was tested in a simulated boundary layer wind flow. The tests were carried out along the specification of the Commonwealth Advisory Aeronautical Research Council (CAARC). Measurements of the fluctuating pressure have been taken at sixty pressure tap for various wind directions. The pressure spectra have been detected at various pressure taps locations. The influence of wind direction on the pressure distribution has been discussed in detail and results have been compared with those obtained from various other establishments that undertook similar testing on the CAARC model. The degree of agreement of the results from this study with the other results was good and within the range of reasonable experimental accuracy. The close agreement in the results gives us confidence in the technique established in the simulation of the natural wind in the wind tunnel and in the experimental data obtained on the dynamic behaviour of the modelled structures. Also from a comparison of the results with the NBC wind code shows that the code is conservative in estimating the wind induced response of tall buildings.

ACKNOWLEDGEMENTS

The author wishes to express his profound appreciation to Dr. H. Tanaka for suggesting this topic and for his advice, encouragement, and support over the period that this study has taken place.

Thanks are due to Dr. B. Tryggvason and Mr. M. Savage of the NAE/NRCC for the help renderd in carrying out some of the experiments and for their assistance in setting up the laboratory equipments at the NAE/NRCC.

CONTENTS

LIST OF TABLES

LIST OF FIGURES

LIST OF SYMBOLS

A	cross sectional area of tube
a_o	mean velocity of sound
C_p	local mean pressure coefficients
C_{σ_p}	local fluctuating pressure coefficients
C_M	base overturning moment coefficients
D_x	narrow dimension of building cross section
D_y	wide dimension of building cross section
f	frequency (Hz)
H	building height
$i = \sqrt{-1}$	imaginary unit
I_u	intensity of turbulence
J_i	Bessel function of first kind of order i
k	polytropic constant for the pressure transducer volume
L	tube length
L_u	integral scale of turbulence
M_x, M_y	base overturning moments in x and y directions respectively
N	number of tubes and volumes
P	amplitude of fluctuating pressure
$\bar{P}$	mean local pressure
P_i	amplitude of fluctuating input pressure

P_0	amplitude of fluctuating output pressure
P_r	Prandtl number
P_s	mean pressure
R	inner radius of the tube
$S_p(f)$	power spectral density of pressure fluctuations
$S_u(f)$	power spectral density of velocity fluctuations
V_f	free-stream wind velocity
V_h	reference velocity at top of building
V_g	mean gradient velocity
V_z	local mean velocity
V_t	volume inside the tube
V_v	volume inside the pressure transducer
Z	height above ground
α	power-law index
β	wind angle
δ	thickness of boundary layer
γ	specific heat ratio
μ	absolute fluid viscosity
ξ	fractional pressure excess
ρ	air density
σ	dimensionless increase in transducer volume
σ_p	standard deviation value (rms) of pressure fluctuations
σ_u	standard deviation value (rms) of velocity fluctuations
ω	circular frequency

PART I :CORRECTION OF OSCILLATING PRESSURE IN PNEUMATIC TUBINGS

Chapter I

INTRODUCTION

The common practice in measuring fluctuating pressure on building models in wind tunnels is to connect the pressure taps of the models with pneumatic tubing to a Scanivalve, which consists of a pressure transducer and a multiport switching system. In this manner pressure can be measured at any point on the model with only one transducer. However, the use of pneumatic tubing systems introduces amplitude and phase distortion in fluctuating pressure signals. It is known that the frequency response of the single tube-transducer system is not flat; i.e., the amplitude of the pressure signal is amplified and the phase is distorted. For the exact measurement of dynamic pressure fluctuation, it is desirable to obtain a transmitted pressure signal having a frequency response curve close to unity and with a phase-lag function varying linearly with increasing frequency.

It has also been shown that the dynamic response of the system for very short tubes is virtually flat up to moderate frequencies (100 Hz at approximatly 5% accuracy for single, 1.35 mm diameter tubes) [1]. But for practical reasons most experiments require longer tubes to be used to connect the

pressure taps to pressure transducers. Thus, it would be difficult to maintain the amplitude and phase conditions properly as the tube lengths become long and correction methods become essential. Formulae and techniques to correct the response of a pressure measuring system have been considered by many authors. The brief summary of them follows.

Iberall, A. S. derived a theoretical formula to obtain the dynamic response of pressure fluctuations through instrument lines considering the fundamental flow equations [2]. A more detailed theoretical and experimental investigation, based on the earlier work by Iberall was developed by Bergh, H. and Tijdeman, H. [3], from which the dynamic response through a series connection of N tubes and N volume elements can be found. Another method proposed by both Irwin, H.P.A.H., and Cooper, K.R. [4], and Surry, D. and Stathopoulos, T. [1], which involves the use of correcting restrictors in the tubes, is an attempt to eliminate the acoustic resonance errors. They showed that an optimally flat response curve can be obtained by the proper choice of size and position of restrictors in pneumatic tubes. Recently Irwin, H.P.A.H., and Cooper, K.R. [4], also developed a method in which fluctuating pressure signal is corrected digitally for amplitude distortion and phase-lag using the inverse transfer function of the tubing system. The inverse transfer function (I.T.F.) has been proven to be

very efficient in correcting the transfer function of the pressure measuring system for various tube lengths. Recently Gumley S.J. [6] applied the formulae developed by Bergh and Tijdeman to wind engineering instruments and in a later work [7] he extended these theories to tubing networks comprising several tubes in parallel for measuring fluctuating averaged pressures.

In the present study, the I.T.F. method has been implemented to correct the fluctuating pressure signals measured in a pressure study on the CAARC standard tall building model. Furthermore, experimental investigation was carried out to determine the transfer function for standard 1.35 mm diameter poly-vinyl chloride (pvc) tubes of various lengths and their frequency response has been corrected digitally. Also comparison of the results has been made with those obtained using the theory of Bergh and Tijdeman [3] and the effect of varying the parameters for a single pressure measuring system has been theoretically investigated.

Chapter II

THEORETICAL DEVELOPMENT

2.1 DYNAMIC RESPONSE OF THE PRESSURE MEASURING SYSTEM

For a simple system consisting of a single tube which transmits the inlet pressure at one end to a pressure transducer at the other end, Fig. 1, the frequency response curve of the system is not flat and the magnitude and phase of the signal are distorted. If the system is characterized by the tube length, its internal diameter, and the transducer s internal volume, then the transfer function can simply be represented as the ratio of the fluctuating output pressure to the fluctuating input at each frequency as follows:

$$P.T.F. = P_{out}(\omega) \; / \; P_{in}(\omega) \qquad (1)$$

in which

P.T.F. = pressure transfer function,

P_{out} = fluctuating output pressure,

P_{in} = fluctuating input pressure, and

ω = circular frequency.

Neglecting the effect of viscosity, heat conductivity, and the internal volume of the pressure transducer, which is

presumably much less than the volume inside the tube, the above equation can be represented, for sinusiodally fluctuating pressure, by

$$P_{out}(\omega) / P_{in}(\omega) = 1/COS(\omega L/a_o) \qquad (2)$$

where

L = tube length, and

a_o = speed of sound.

Eq. (2) is the equation for a simple organ pipe resonance, and for small air velocity in the tube compared to the speed of sound a_o[8]. However , the simple organ pipe theory cannot be used since the output pressure is amplified drastically and tends to be infinity at resonance. Also, it neglects the viscosity ,heat conductivity, and the transducer inner volume.

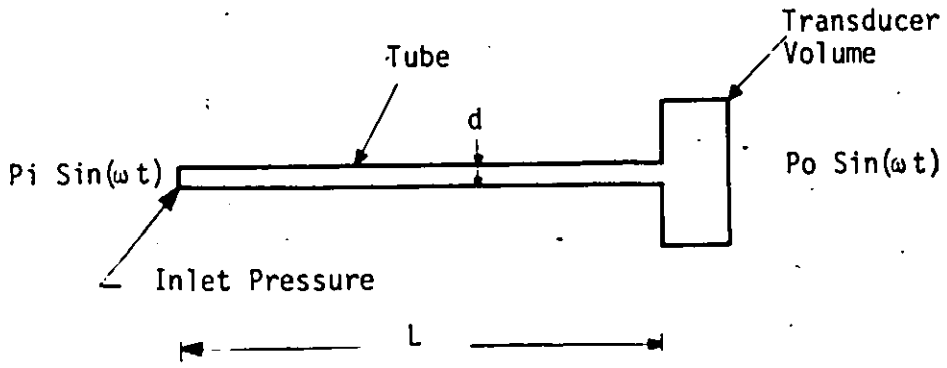

Figure 1: Tube-Pressure Sensitive System

Iberall [2] derived an elementery theoretical formula for the attenuation and phase-lag for a tube-pressure sensitive system. Assuming that the fluid is incompressible and that the sinusoidal disturbances of the pressure at the tube entrance are of small amplitude compared to their mean, the theory was derived from the fundamental flow equations, i.e. Navier-Stokes equations, the equation of continuity, the energy equation and the equation of state . He found that the amplitude of the pressure excess, $(P - P_o)$, at the end of the tube to that at the inlet is given by :

$$\bar{\xi}_L / \bar{\xi}_o = \frac{1}{\chi_o i + 1} \qquad (3)$$

where

$$\chi_o = \lambda_o \omega$$

$$\lambda_o = 32 \frac{\mu_o}{P_o} \left(\frac{L}{D}\right)^2 \frac{V}{AL} ,$$

P = pressure,

P_o = mean pressure at the entrance,

$\bar{\xi}_L$ = maximum amplitude of the pressure excess at the instrument side,

$\bar{\xi}_o$ = amplitude of the fractional pressure excess ($\Delta p/p_o$) at the origin (x=0),

ω = circular frequency,

μ_o = mean fluid dynamic viscosity,

A = cross sectional area of the tube,

D = inside diameter of tube,

L = tube length,

V = instrument volume, and

$i = \sqrt{-1}$ imaginary unit

The real part of the above equation is the attenuation in amplitude of the pressure excess, whereas the imaginary part is the phase-lag. Later, Iberall modified the elemantery theory to take into account the effect of fluid compressibility, the finite pressure excess, the fluid acceleration, the finite length of tubing, and heat conduction. The detailed theory can be found in the reference [2].

Based on the theoretical work of Iberall, Bergh and Tijdeman generalized the theory for calculating the transfer function for pneumatic tubing system. In their derivation they have assumed that:

1. the flow is laminar in the tube,
2. the length-to-diameter ratio of the tube was large,
3. the tube wall has very high heat conductivity, and
4. magnitude of the fluctuating pressures is very small about their absolute mean.

For a series connections of N-tubes and N-volumes (Fig. 2), following recursion formula has been obtained that relates the sinusoidal pressure in successive nodal volumes by the appropriate transfer function for the tubing between them.

$$\frac{P_j}{P_{j-1}} = \left[\cosh(\phi_j L_j) + \frac{V_{vj}}{V_{tj}} \left(\sigma_j + \frac{1}{K_j}\right) n_j \phi_j L_j \, \mathrm{Sinh}(\phi_j L_j) + \right.$$

$$\frac{V_{t_{j+1}} \phi_{j+1} L_j J_o(\alpha_j) J2(\alpha_{j+1})}{V_{t_j} \phi_j L_{j+1} J_o(\alpha_{j+1}) J_2(\alpha_j)} \cdot \frac{\mathrm{Sinh}(\phi_j L_j)}{\mathrm{Sinh}(\phi_{j+1} L_{j+1})} \cosh(\phi_{j+1} L_{j+1})$$

$$\left. - \frac{P_{j+1}}{P_j}\right]^{-1} \qquad (4)$$

in which

$$\phi_j = \frac{w}{a_{oj}} \sqrt{\frac{J_o(\alpha_j)}{J2(\alpha_j)}} \sqrt{\frac{\gamma}{n_j}}$$

$$\alpha_j = i^{3/2} R_j \sqrt{\frac{\rho_s w}{\mu}}$$

$$n_j = \left[1 + \frac{\gamma - 1}{\gamma} \frac{J_2(\alpha_j \sqrt{P_r})}{J_o(\alpha \sqrt{P_r})}\right]^{-1}$$

L = tube length,

k = a polytropic index for expansion in volume element,

σ = a dimensionless increase in transducer volume due to diaphragm deflection,

ω = circular frequency,

a_o = mean velocity of sound,

P_s = mean pressure,

P_j = amplitude of pressure disturbance,

ρ = mean density,

$\gamma = c_p/c_v$ = specific heat ratio,

R = inner tube radius,

$P_r = \sqrt{\mu c_p/\lambda}$ = Prandtl number,

μ = absolute fluid viscosity,

λ = thermal conductivity,

V_t = inside volume of the tube,

V_v = inside volume of the pressure transducer, and

J = the ith order Bessel function of first kind.

The above formula can be used to find the dynamic response of a system where abrupt change of the diameter occurs.

Also, in a later investigation [9], the authors found that equation (4) should be modified for the cross flow velocity of the main stream across the tapping entrance.

For a single pressure system consisting of a tube connected to a transducer at one end, the dynamic response function would be obtained by setting j = n = 1 in the general formula.

Thus,

$$\frac{P_1}{P_o} = \left[\cosh(\phi L) + \frac{V_v}{V_t}\left(\sigma + \frac{1}{K}\right)n\phi L.\sinh(\phi L)\right]^{-1} \qquad (5)$$

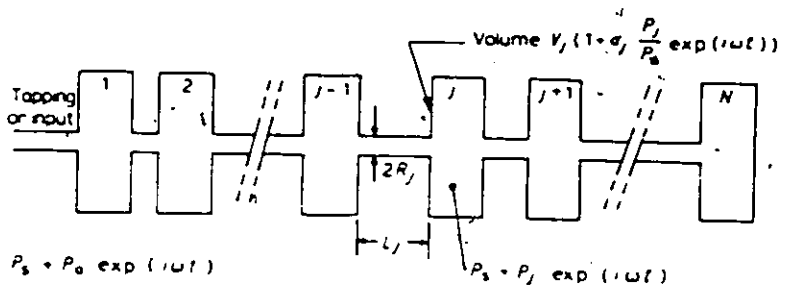

Figure 2: Series Connections of Tubes and Volumes

2.2 REDUCTION AND CORRECTION OF THE TRANSFER FUNCTION

Methods using restrictor devices to reduce the amplitude of a distorted signal for a single tubing system have been thoroughly examined by both Irwin et al [4] and Surry and Stathopoulos [1]. The method requires the introduction of restrictors (small tube connectors of significantly reduced area) which act as dampers in the system and eliminate the acoustic resonance errors. They have shown that an optimum condition can be obtained by proper combinations of tube length-restrictor position. Fig. 3 shows the dynamic response that can be achieved by using the optimum position of restrictors in tubes ranging in length up to 5 ft. The same figure also shows that the amplitude deviation of the response function can be reduced to less then 5 % of unity over the frequency range of 0 - 100 Hz. Very long tubing (5 ft.) has been found not to need any restrictors since the

damping exceeds the required damping to suppress the first resonant peak.

Also, it has been found that the restrictor method does not correct the phase-lag, but in fact even exaggerate it. However, the problem of phase distortion is not very essential in most of the wind engineering experiments conducted on models using short pneumatic tubing systems.

Another method was introduced by Irwin and Cooper to correct the transfer function digitally using the Fast Fourier Transform technique. The method simply works by recording the distorted pressure signal and correcting it digitally using the response function of the system which is assumed known.

Let the inlet oscillating pressure be given by

$$P_{in}(t) = \sum_{-\infty}^{+\infty} A_n . \exp(in\omega t) \qquad (6)$$

and similarly the oscillating pressure at the transducer as

$$P_{out}(t) = \sum_{-\infty}^{+\infty} B_n . \exp(in\omega t) \qquad (7)$$

where A_n and B_n are the complex Fourier coefficients, $i = \sqrt{-1}$ (imaginary unit), and ω = circular frequency.

For a known transfer function T_n, it can be written

$$B_n = T_n \times A_n \qquad (8)$$

from which the complex Fourier coefficient of the inlet pressure can be evaluated as follows :

$$A_n = B_n / T_n \qquad (9)$$

The Fourier transform B_n of the distorted signal can be measured first, and from equation (9) A_n can be determined if the transfer function of the system is known. Finally the undistorted pressure signal $P_{in}(t)$ would be obtained by computing the inverse Fourier transform of A_n.

This method has been found very effective in correcting the amplitude and phase-lag of the transfer function for tubes of various lengths.

Chapter III

EXPERIMENTAL INVESTIGATION

3.1 MEASUREMENT OF THE TRANSFER FUNCTION

In the present work, the transfer function of various tube lengths has been measured using the fast Fourier transform technique and the following procedures explain the experimental steps that have been performed.

In order to obtain a sinusiodally fluctuating pressure signal, a static pressure supply of preset magnitude is fed to a fluidic signal generator which in turn receives a white noise voltage signal. The oscillating pressure signals have the same form as the input voltage signal. The fluctuating pressure signals were transmitted to a differential pressure transducer (Setra System Inc. Model 237, ± 0.1 psi) through a very short tube. The same signals were transmitted to another transducer of the same type and properties, through a 1.35 mm (0.053 in.) diameter standard pvc tube of preselected length. The fluctuating pressure signals received by both transducers were fed to a Hewelt Packard 5452A Fourier Analyzer . The signals were digitized at a rate of 500 points per second and stored in blocks of 524 points. Then, the transfer function of the system was computed and displayed on the CRT display of the Fourier

Analyzer. Fig. 4 shows a block diagram of the instruments used in the experiment. As it is expected the measured transfer function has a resonant peak and the signal shows no similarity to the original signal which has a flat response curve.

This process has been repeated and the transfer functions of various tube length have been measured. Figs. 5 - 10 show the measured transfer functions for tube lengths ranging from 1/2 ft. (0.15 m) to 5.0 ft. (1.52 m).

3.2 CORRECTION OF THE MEASURED TRANSFER FUNCTION

Using the technique developed by Irwin and Cooper to correct the transfer function digitally, an additional apparatus is added to the system described in the previous section. The apparatus, which is called the "TRANSDUCER RESPONSE EQUALIZER" (TRE), receives the distorted pressure signals from the pressure transducer, then corrects the amplitude and the phase-lag using the inverse transfer function. The pressure signals are transmitted to the Fourier Analyzer, where the transfer function is being computed and displayed on the CRT display of the Analyzer. Path B in Fig. 4 shows the assemblage of the apparatus to correct the transfer function.

Figs. 5 - 10 show the corrected transfer functions for the same tubing system used in the previous experiment. As expected, the overall magnitudes of the corrected response

functions are within unity over the range of frequencies of our interest.

3.3 MEASUREMENT OF THE T.R.E. INVERSE TRANSFER FUNCTION

Path C of Fig. 4 shows the apparatus assenblage for this experiment. The white noise voltage signals were directly fed to the "TRANSDUCER RESPONSE EQUALIZER". The signals were transmitted to the Fourier Analyzer, where the inverse transfer function of the preselected tube length had been computed and displayed.

3.4 DISCUSSION OF THE RESULTS

3.4.1 EXPERIMENTAL

Figs. 5 - 10 show the frequency response function for a single pressure measuring system for several tubing lengths. All the tubes tested had a standard 1.35 mm (0.053 in.) diameter and ranged in length from 1/2 ft. (0.15 m) to 5.0 ft. (1.52 m). Curve A shows the uncorrected transfer function for each tube over a frequency range of 0 Hz - 400 Hz. As expected, the measured transfer functions are not a faithful representation of the original input, and the magnitude of the signal has been distorted. Comparison between these curves shows that for longer tube length the peak resonance occurs at lower excitation frequencies and the peak magnitude of the signal reduces significantly. It is also noted that for tube lengths over 5 ft. (1.52 m), the

resonance peak is totally eliminated. The reason of this observation can be explained by the excess damping provided by the longer tubes, which eliminates the resonant peaks in the response function.

Furthermore, it was noted that for very short tube length (the order of 1/2 ft.) the response function was almost flat and near unity up to a frequency of approximately 100 Hz. For a 1.35 mm diameter , 1/2 ft. (.15 m) long standard pvc tube, the magnitude of the transfer function at frequency f = 75 Hz is 6 % over unity. Since most of the experiments on buildings are tested typically over a frequency range of up to 100 Hz, short tubing length can be used for pressure measurement with satisfactory results.

Curve B in Figs. 5 - 10 represents the transfer function after correction by the TRE. Comparison of curves A and B , for each tubing system, shows that the first resonant peak which causes the most significant error reading is flattened and the overall magnitude of the fluctuating signal is within unity. For 2 ft. (.61 m) tube, the first resonant peak magnitude of 2.7 is reduced to 1.05 at resonant frequency f = 95 Hz and the maximum deviation from unity is the order of 8 %.

In order to obtain a flat response function of unity amplitude, the transfer function obtained from the TRE itself should be the inverse of the amplitude corrected transfer function for the various tube lengths. The

frequency response function of the TRE of preselected tube lengths is presented by curves C in Figs. 5 - 10. As mentioned above, the transfer function represented by curve C is found to be approximately the inverse function of curve B. The agreement is fairly good for short tube lengths. The slight shift in the transfer function is a result of the phase-lag,

3.5 COMPARISON WITH THEORETICAL FORMULA

It is useful to check the validity of experimental results by comparing with theoretical derivation. The transfer function of a single tube pressure measuring system derived by Bergh and Tijdeman [3] has been used to compare the experimental results.

Figures 11 - 16 show good agreement in results obtained from both methods. Specific assumptions have been made in deriving the theory, and violation of these assumptions could lead to discrepancy in the results. The theoretical formula assumes an ideal tube with constant inner diameter. Also the internal volume of the transducer is assumed constant for all cases and not to be changed by the deflection of the diaphragm. In reality, the internal diameter of tubes is not necessarily constant because of the local deviations of material and its flexibility, and the changes in the inner volume of pressure transducer may not be as exact as specified by the manufacturer. Furthermore,

the degree of discrepancy was higher for tubes of short length (1/2 ft.). This may be the result of violating the assumption 2 of section 2.1 which assumed that the length-to-diameter ratio of the tube was large. The maximum amplitude deviation detected was the order of 5% for the tube length of 1 ft. (0.30 m).

Both methods have been proven to be reliable and good results may be obtained with a careful measurement and estimation of the system parameters.

3.6 RESULTS OF CHANGE IN THE PARAMETERS

It has been shown earlier, in the mathematical model derived by Bergh and Tijdeman, that the transfer function for a single tubing system varies as a function of the following parameters:

- -the tube length and diameter,
- -the transducer cavity volume,
- -the increase in transducer volume due to diaphragm deflection,
- -the polytropic constant for the pressure expansion in the transducer volume, and
- -fluid properties.

Changing one of the above parameters while keeping the others constant has been done to check how the transfer function would be affected. Figures 17 - 20 show that by keeping the tube length constant and varying the inner

diameter of the tube, the resonant peak decreases for smaller diameter and shifts towards lower frequencies. Fig. 20 shows that for a given tube length and diameter (l = 5ft.(1.52 m), d = 1/2 mm) the transfer function has no resonant peak. Fig. 21 illustrates that there is no considerable change in the transfer function unless the internal volume of the transducer is drastically increased. The change in the polytropic constant by taking the extreme value (k = 1.0 for isothermal, and k = 1.4 for isentropic) shows no significant effect on the transfer function as is shown in Fig. 22. Finally the variations of the mean static pressure seem to have considerable influence on the transfer function and the resonant peak decreased significantly as the mean pressure decreased, see Fig. 23.

Chapter IV

CONCLUSION

The use of the Transducer Response Equalizer to digitally correct the distorted fluctuating pressure signals has proven to be effective and the peak resonance for various tube lengths has been found to be suppressed resulting in the nearly flat frequency response functions.

Comparison of the experimental results with those derived from the theory by Bergh and Tijdeman has proven that the latter can predict the transfer function with good accuracy. Also from the parametric study, it was shown that the length and diameter of the tubes and the mean static pressure had the most significant effect on the transfer function. The internal volume of the pressure transducer and the polytropic constant showed minimal effect. It has also been proven by Bergh and Tijdeman that the material of the tubes does not have influence on the transfer function.

The Transducer Response Equalizer utilized in this study is employed in correcting the measurement of fluctuating pressure signals on the CAARC Standard Tall Building Model in Part II of this study. From the good agreement in the results in the present study, it is concluded that the TRE is a very effective and simple method to correct the

deviation in pneumatic tubing systems for the measurement of fluctuating pressure components. Furthermore, this equipment can be implemented in nearly all of wind engineering experiments conducted in low speed wind tunnels, thus avoiding the need for theoretical and calibration correction functions for experimental results.

PART II: PRESSURE MEASUREMENT ON THE 1:1000 SCALED MODEL OF THE CAARC STANDARD TALL BUILDING

Chapter V

INTRODUCTION

In recent years, the desire for more realistic design criteria for structures has focused increased research attention upon the prediction of aerodynamic forces on them. All buildings and structures are subjected to wind with turbulence inherently existing in the atmospheric boundary layer, and due to the advent of structures with decreasing structural damping, increasing slenderness, thinner cladding and larger glass areas, knowledge of the fluctuating loading is of prime interest to take advantage of the potential gains involved in the sophisticated design.

While significant progress has been made with regard to the problem of wind induced forces on buildings and structures and also the response of them to these forces, some of the research effort has been concentrated on the simulation of natural wind characteristics in wind tunnels for experimental investigations on buildings and other structures. Building models which reflect the pertinent geometric and/or mechanical characteristics of the prototype object to be placed in the simulated atmospheric surface layer developed in low-speed wind tunnels of appropriate size. This technique offers the most convenient method for

the systematic measurement of pressure coefficients and response. For tall buildings, these simulations have been usually achieved to scale ratios from 1:200 to 1:500 . The models are placed in a wind tunnel of sufficient size to allow development of a turbulent boundary layer to a depth closely representative of the atmospheric surface layer. This technique introduces the need to know not only the characteristics of flows being simulated but also the faithfullness with which they are actually reproduced in the simulations. Nevertheless, correlations of the pressure and response measurements between model and full scale are in certain cases remarkably good.

Since the primary purpose of wind tunnel testing on building models is either to determine the dynamic response of the building as a whole by means of an aeroelastic model or the magnitude of the wind induced local pressures by means of a pressure model, it has been found that the experimental approach with regard to the simulation of natural wind characteristics caused diversity in opinions among the researchers. As an attempt to bring about the various approaches used, it was decided during one of the Commonwealth Advisory Aeronautical Research Council (CAARC) specialists meeting on "non - aeronautical aerodynamics" at the National Physical Laboratory (NPL), Teddington, England, in 1969, to specify a standard building of simple design in a given wind environment as a common

problem for investigation, and to propose certain measurments on aeroelastic and pressure models of this. The selection of building characteristics is intended to be representative of a class of contemporary buildings, and the specification of wind characteristics was partially specified to give more flexibility in the simulation for the existing laboratory facilities. Successful results have been obtained from various establishments that undertook similar tests on 1:200 - 1:600 scale models of the CAARC Standard Tall Building.

This study goes further to investigate pressure tests on a relatively exaggerated pressure model of 1:1000 scale ratio. The building model has been tested at the 2 ft. x 3 ft. (0.61m x 0.91m) wind tunnel existing at the University of Ottawa. The turbulent boundary layer generated in the wind tunnel was representative of an atmospheric boundary layer over suburban areas. The series of testing involved measuring the mean, standard deviation and power spectral density of the fluctuating pressure at the various tap locations and with various wind directions. The experimental results have been summarized at the end of this report. The fluctuating pressure distribution on the four faces of the model, and the power spectra of the fluctuating pressure are thoroughly discussed and compared with published results from other establishments that undertook similar testing. Also results were compared with the

definition of wind load on tall buildings by the National Building Code of Canada (NBC).

Chapter VI

CAARC STANDARD TALL BUILDING

6.1 INTRODUCTION

During a meeting of the CAARC co-ordinators in the field of aerodynamics that was held at the National Physical Laboratories, Teddington, England on March 1969, the problem mentioned in chapter V was discussed and a decision was made to propose a standard building for testing purpose in wind tunnel and comparison of the experimental results. It was decided that the building should have a fairly simple design in given wind conditions, and the prime testing objectives were to measure the dynamic response and the mean and standard deviation of the fluctuating pressures. Simulation of the atmospheric boundary layer was assumed to be representative of wind flow over a fetch of uniformly rough terrain. This assumption gives more freedom for the researchers since it is difficult in some facilities to simulate specific conditions.

Wardlaw, R. and Moss, G. [10] prepared the specifications for a standard tall building to compare simulated natural winds in wind tunnels. Various institutions have done measurements on the proposed CAARC standard tall building

and comparison of the results has been reported and discussed by Melbourne, W.H. [11]. It was concluded in the report that the measured results were in "fairly good" agreement.

6.2 MODEL SPECIFICATION

6.2.1 BUILDING GEOMETRY

The proposed model building is a rectangular prismatic shape with dimensions 100 ft. x 150 ft. and height 600 ft. (30.48 x 45.72 x 183.88 m). The rectangular cross section does not change along the height. The building has a flat top without parapets, and the exterior walls are flat without mullions or other geometric disturbances. Figure 24 shows the detailed dimensions and the definition of wind, the location of surface pressure tap holes and their numerical identification.

6.2.2 DYNAMIC PROPERTIES

Only the fundamental, linear mode of vibration shall be considered, the movement being taken as a rigid body rotation about a centre at the ground level. The weight distribution is uniform throughout the structure and is 10 lb/ft^3(160 Kg/m^3). The structural damping is assumed to be 1 % of critical and the natural frequency is equal to 0.2 Hz with respect to both axis.

6.2.3 WIND STRUCTURE

The natural boundary layer wind is to be representative of the wind blowing over a long fetch of forest or urban development with building heights in the range of 20 - 50 ft. (6 -15 m). It was suggested that the power-law exponent of the mean velocity profile should be about 0.28 .

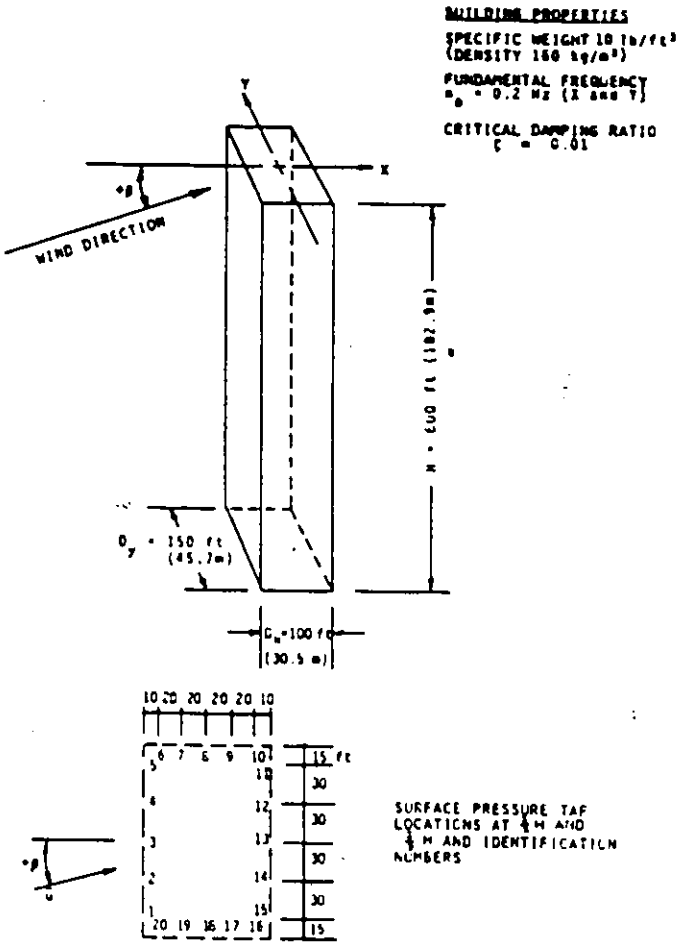

Figure 24. CAARC Standard Tall Building: Properties and Dimensions.

6.3 MODEL MEASUREMENTS

6.3.1 WIND CHARACTERISTICS

The following properties of the wind would be required to facilitate the comparison of the wind characteristics:

- -Profile of mean velocity,
- -Profile of longitudinal component of turbulence intensity, and
- -Power spectrum of longitudinal velocity component at a height of 400 ft (121.92 m).

The reference values for pressure and velocities are to be taken at the building height of 600 ft. (182.88 m).

6.3.2 PRESSURE MEASUREMENTS

The pressure measurement is to be carried out at the 2/3 height of building (400 ft. above ground) on each face of the building and additional measurements may be made at different heights. The wind direction was not specified in the original proposal. The mean and the root-mean-square of the fluctuating pressure components are of primary interest. Additional measurements of the power spectra were suggested.

Chapter VII

CHARACTERISTICS OF THE EXPERIMENTAL MODELS

7.1 PRESSURE MODEL OF CAARC BUILDING

The model has a rectangular prismatic shape 1.2 in. x 1.8 in. x 7.2 in. (3.05 cm x 4.57 cm x 18.29 cm) heigh (corresponding to 100 x 150 x 600 ft. high on the scale ratio of 1:1000) with 90 degree corners and constant cross section with height. It is made of plexiglass of 1/16 in. (0.16 cm) uniform thickness. Sixty pressure tap holes were drilled on the four faces of the model and distributed equally at 1/3 and 2/3 of the building height from the ground level, and at 1/4 in. (0.63 cm) below the top. Each level has 20 pressure taps with 5 taps on each face located at equal distances. Figs. 25 and 26 show details and dimensions of the 1:1000 scaled model of the CAARC standard building with the location of the pressure taps and numbering system. Typical pvc tubings with internal diameter of 1.35 mm (0.053 in.) and 2 ft. (0.61 m) long were used to connect the pressure taps to a Scanivalve which houses a differential pressure transducer. At the points of measurement, thin brass tubes of 1/2 in. (1.27 cm) long were placed normal to the outer surface of the model. Fig. 25 shows a section of the building model and a detail of the construction of pressure taps.

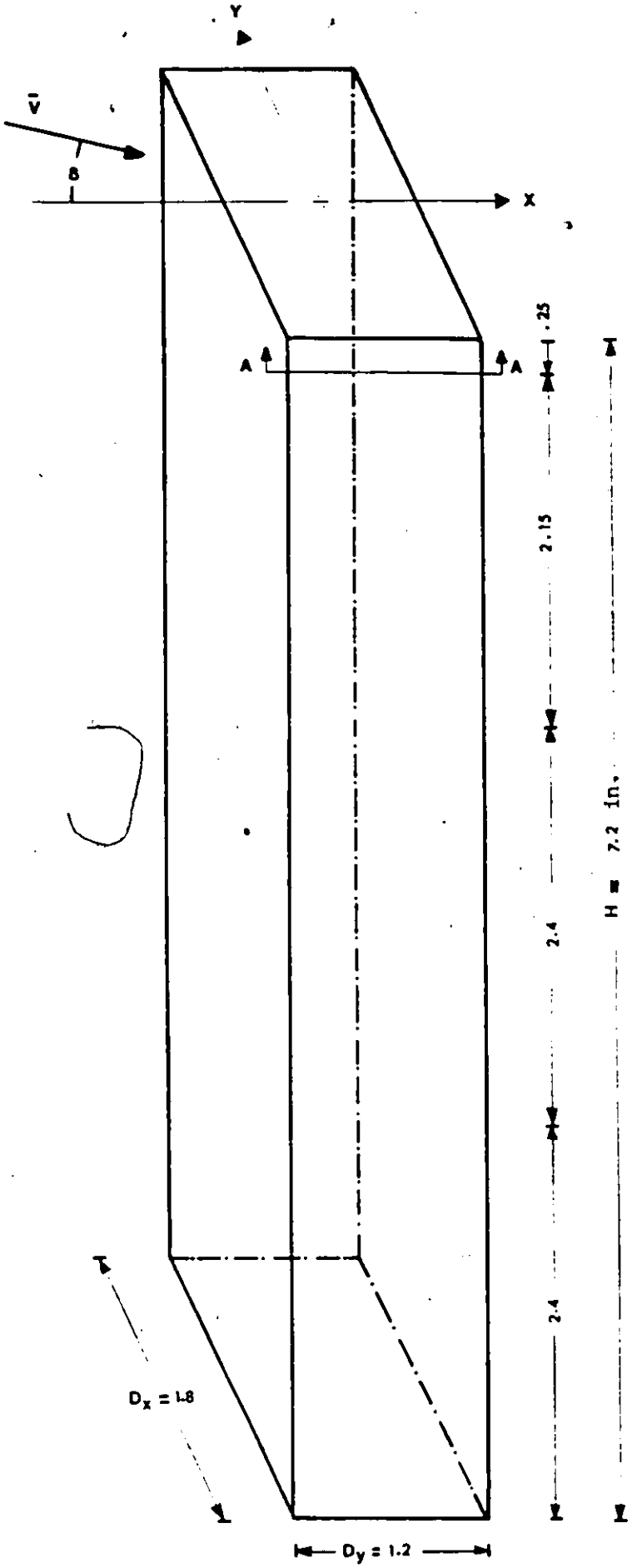

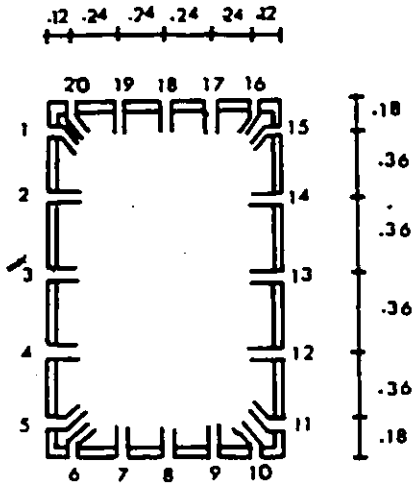

Section A-A

Surface Pressure Taps Locations At H, 2/3 H, 1/3 H, and Identification Numbers. (Brass Tubing :L = .75in.)

Figure 25 . 1:1000 Scaled Plexiglass Pressure Model of CAARC Standard Tall Building.

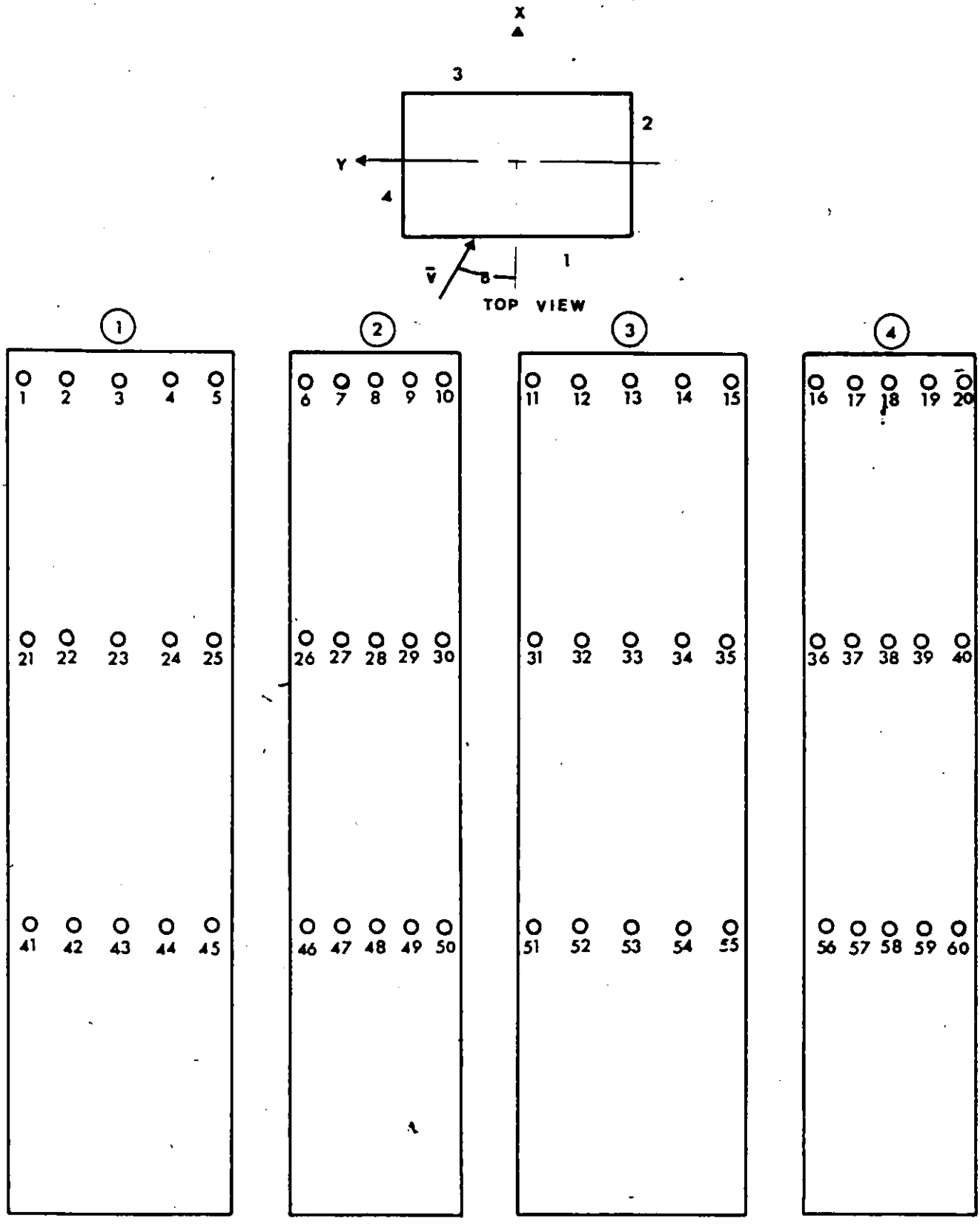

Figure 26. Numbering Scheme for Pressure Taps.

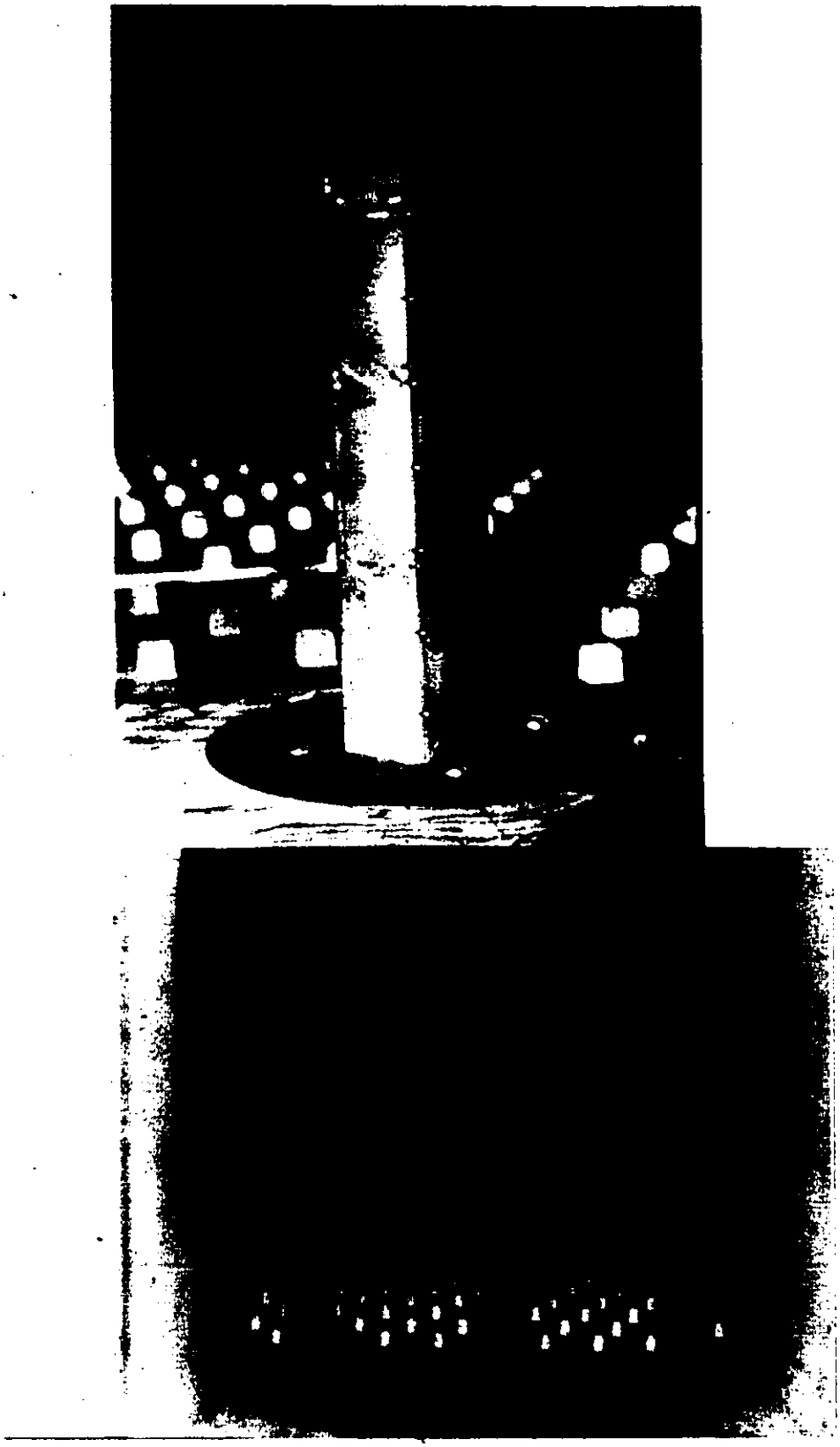

Figure 27. View of the Model in the Wind Tunnel.

The model was rigidly mounted on a turntable which provides angular rotation to change wind azimuth. The surface of the turntable was placed at the same level as the simulated ground surface in the test section and the turntable could be rotated 360 degrees so the wind direction can be varied relative to the model. The pressure tubings were led from the points of measurements through a hole at the centre of the turntable and out of the tunnel to the Scanivalve. Maximum model blockage as a percentage of tunnel working section area was approximatly 1.8 %, and therefore it was considered that no correction should be required for the pressure data. View of the model installed in the wind tunnel is shown in Fig. 27.

7.2 SIMULATION OF THE ATMOSPHERIC SURFACE LAYER

Several techniques have been used to simulate the growth of turbulent boundary layers in test section of wind tunnels which are relatively short in length. A simple and effective method consisting of spires and floor roughness elements has been implemented in this experiment. This technique was thoroughly investigated [12] at the National Aeronautical Establishment (NAE), National Reaserch Council Canada (NRCC), and the resulting wind characteristics using various types of spires have been reported in references [13,14].

The low speed wind tunnel existing at the University of Ottawa has an open circuit (Eiffel type) with a working section of 2 ft. x 3 ft. (61 cm x 91 cm). A set of three 16.0 in. (40.64 cm) high triangular spires are mounted at the entrance to the test section, and followed by rows of cubic roughness elements placed at a spacing of 2.5 in. (6.35 cm) centre to centre in staggered arrays to develop a shear flow layer over a 7 ft. (2.1 m) long test section with a proper mean speed profile and turbulence structure. A description of the detailed configuration of the wind tunnel floor and the model location are presented in Figs. 28 and 29.

With the above described simulation, a turbulent shear layer with a power law index of $\alpha = 0.28$ and a boundary layer thickness of $\delta = 14$ in. (36 cm) was obtained at the

model location. The details of the experimental investigation on wind simulations have been reported by Mak, c. [15] and are also discussed in a later section of the present study.

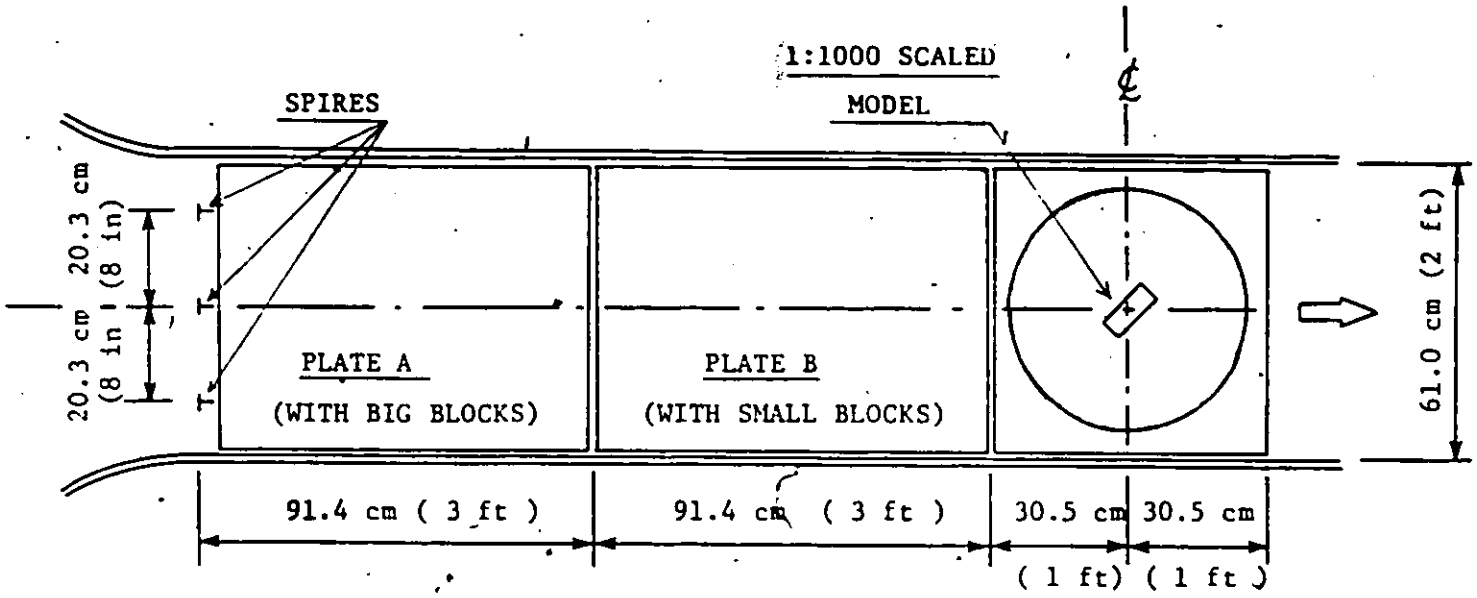

BIG BLOCKS : 1.3 x 1.3 x 1.9 cm
(0.5 x 0.5 x 0.75 in)

SMALL BLOCKS :1.3 x 1.3 x 1.3 cm
(0.5 x 0.5 x 0.5 in)

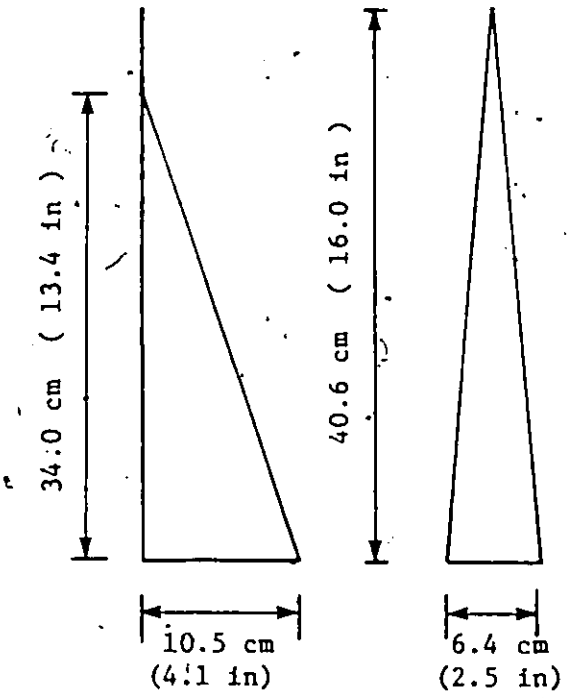

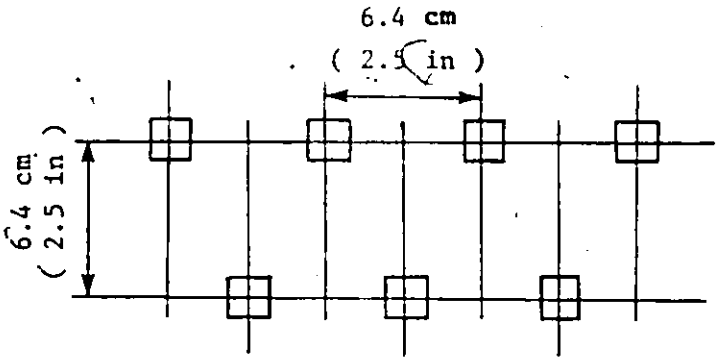

ARRANGEMENT OF BLOCKS

Figure 28. Design for Production of Simulated Atmospheric Boundary Layer Flow, (15).

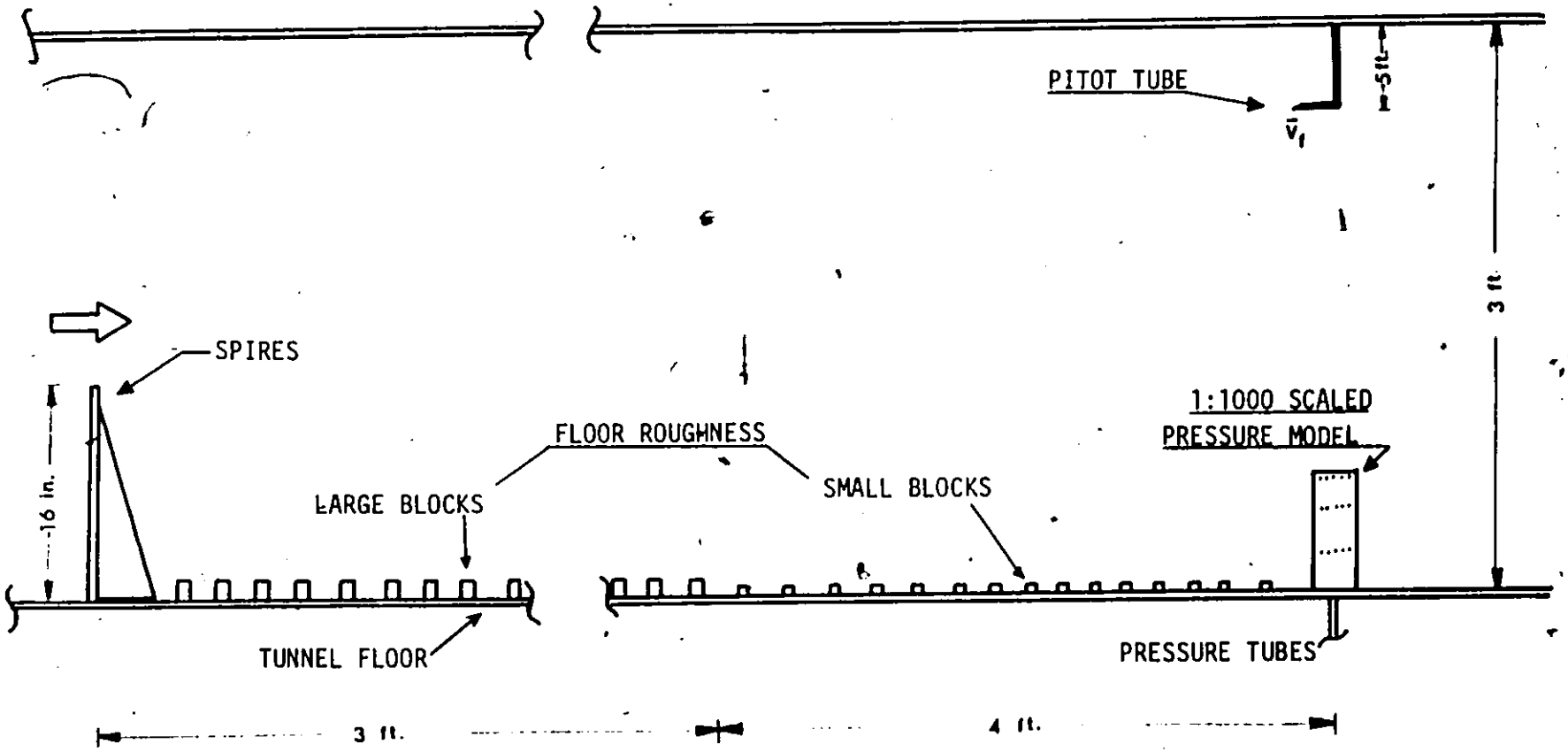

Figure 29. Sketch of Tunnel Side View.

7.3 INSTRUMENTATION FOR PRESSURE MEASUREMENTS

Fig. 30 shows a block diagram of the instruments that have been used in measuring the fluctuating pressure on the building model and the properties of the simulated turbulent wind. Some detailed description of each instrument follows.

1. Inclined Manometer

   The R. Fuess 134b Micromanometer was used to measure the reference wind speed in the tunnel. It consists of a U-tube filled with alcohol of specific gravity 0.8, and can be adjusted to different inclinations. The pressure is supplied through plastic tubings from an NPL type Pitot static tube which is installed in the free stream flow above the tunnel test section. Measurement of the wind speed is done by taking the difference of static and dynamic pressure at the Pitot tube.

2. Scanivalve

   Model 48D3 Scanivalve, (Scanivalve Inc.), was used as a pressure sampling scanner for measurement at multiple pressure channels. It allows the measurement of 48 pressure inputs. The Scanivalve houses a Model 237 ± 0.1 psi. Setra differential pressure transducer (Setra Systems Inc.). The pressure difference was measured with respect to the static pressure in the uniform free-stream, supplied by the Pitot static tube.

3. Voltmeter

The Model 1076 TSI Voltmeter is a true root-mean-square (rms) Voltmeter. It was used in the experiment to measure the fluctuating pressure signals that were initially received by the pressure transducer and then transmitted to the voltmeter. The mean and the rms of the fluctuating pressures at each tap location were displayed digitally with specified averaging time.

4. Transducer Response Equalizer

The Transducer Response Equalizer (TRE) was developed at the NAE/NRCC. It was used to correct the distortion introduced by the use of pneumatic tubings in the measurements of fluctuating pressure. This instrumeht corrects the pressure signal using the inverse transfer function of the tubing-transducer system as is described in Part I of the present study. Correction can be done for various tube lengths and the choice of types of pvc tubings.

5. Pneumatic Tubings

Standard pvc tubes with the internal diameter of 0.035 in. and 2 ft. long were used to connect the pressure taps to the Scanivalve ports.

6. Power Supply

A KG 25 - 0.2 , Kepco, Power Supply was used to activate the differential pressure transducer.

7.4 EXPERIMENTAL SET-UP

7.4.1 MEASURMENTS OF THE WIND STRUCTURE

Measurements of the wind properties, such as the profiles of the mean velocity, the intensity of the longitudinal turbulence component and the power spectrum of longitudinal velocity were carried out for the comparison of the present results to the data from various other establishments.

The use of the spires-roughness elements technique has assured the development of a fully turbulent boundary layer flow over the model location. The above properties of the wind have been measured in an earlier experiment and details of testing procedures are found in Ref. [15].

7.4.2 MEASUREMENTS OF PRESSURE

The building model was fully immersed into the turbulent boundary layer generated by the upstream roughness. The pressure measurements were carried out in a constant free-stream velocity of 50 fps. (15.2 m/s). The model has sixty pressure taps which can be connected via pvc tubes to the 48D3 Scanivalve which houses the sensitive, low pressure, high frequency-response differential pressure transducer. Forty-six pressure inputs were measured at one

time and the other two ports of the Scanivalve were used to measure the static and dynamic pressure signals from the Pitot static tube. The fluctuating pressure signals received by the differential pressure transducer were transmitted to the digital voltmeter where the mean and rms of the signals were evaluated and recorded respectively. Due to the small bore of the pressure tubing, the length of the tubing, and the small Scanivalve internal passages and internal volume, a correction of the distorted pressure signals was required for this measurement. This correction was made by using the technique and procedures given in Part I of the present study. Thus, the Transducer Responce Equalizer was connected to the circuit so the received distorted signals from the transducer would be corrected digitally for the selected length and type of tubings. The measurements were made for various wind directions ranging from 0° to 90° by increment of 10°, because of the symmetry of the model.

The fluctuating pressure signals, of selected pressure taps, were also measured and recorded on FM Magnetic tape, and the power spectra of the recorded signals were calculated using the wave analyzer (Fourier Analyzer A5401) at the NAE/NRCC.

7.5 EXPERIMENTAL RESULTS

7.5.1 . WIND PROPERTIES

Analysis of the wind properties, as mentioned earlier, was carried out by Mak [15], and the following is a summary of his investigations:

Fig. 31 shows the longitudinal velocity profile and it is represented by the power law with an exponent $\alpha = 0.28$. In addition ,the intensity of turbulence is plotted on the same figure and the thickness of the boundary layer at the model location was found to be close to 15 in. (38 cm).

The mean wind velocity V(z) at height z can be expressed by

$$V(z) = V(g)\ (z/\delta)^{\alpha} \qquad (1)$$

where α = the power-law index ($\alpha = 0.28$),

δ = the thickness of the boundary layer ($\delta = 38$ cm), and

$V(g)$ = the gradient height.

It was also found that the turbulence intensity varies from 9 % at the elevation of the model top to 20 % near the tunnel floor level.

The mathematical models of the power spectrum of the longitudinal velocity have been studied by many researchers. The following expression by von Karman is known to be one of

those showing good agreement with the reality both in natural wind and in wind tunnels [16]:

$$\frac{f\,S_u(f)}{\sigma_u^2} = \frac{4\,(f\,L_u/V)}{\{\,1 - 70.7\,(f\,L_u/V)^2\,\}^{5/6}} \qquad (2)$$

Where

V = the longitudinal wind velocity,

L_u = the integral scale of turbulence,

$\frac{fL_u}{V}$ = reduced frequency,

$S_u(f)$ = power spectral density of the longitudinal wind velocity at frequency f, and

σ_u^2 = mean-square value of the velocity fluctuations.

Fig. 32 shows the measured longitudinal velocity spectrum. Compared with the von Karman curve, Fig. 33, the integral scale of turbulence is found to be approximatly 0.14 m.

The Reynolds number in this experiment is found to be equal to 3.8×10^4 and it is based on the wide dimension of the building model and the mean wind velocity measured at the top of the model.

7.6 PRESSURE RESULTS

7.6.1 MEAN AND RMS PRESSURE COEFFICIENTS

All pressure measurements were made at a tunnel speed of 50 fps (15.24 m/s) at the Pitot static tube location 2.6 ft. (0.79 m) above the tunnel floor. Tables 1 to 10 contain the experimental data which are represented in terms of dimensionless pressure coefficients. Generally, as a result of the turbulent boundary layer , the pressure coefficients distribution commonly exhibits drastic variation in both the mean and the fluctuating values.

The local mean pressure coefficient is defined as the local mean pressure normalized by the free-stream dynamic pressure and it is expressed as :

$$C_{\bar{p}} = \frac{\Delta \bar{P}}{\frac{1}{2} \rho \bar{V}_f^2} \qquad (3)$$

Where

$\Delta P = \bar{P} - P_s$

$\bar{P}$ = local mean pressure,

P_s = free-stream static pressure,

ρ = the air density, and

V_f = free-stream wind velocity.

Similarly, the local fluctuating pressure coefficient is defined as the rms of the local fluctuating pressure normalized by the free-stream static pressure and can be written as :

$$C_{\sigma_p} = \frac{\sigma_p}{\frac{1}{2} \rho \bar{V}_f^2} \qquad (4)$$

Where

σ_p = standard deviation value of pressure fluctuations.

To facilitate the comparison of the data from various establishments, it was suggested that the pressure coefficients would be normalized with the velocity taken at the top of the building. Hence, the coefficients were then multiplied by the factor $(V_h/V_f)^2$, where V_h is the wind velocity at the building top which can be given from Eq. (2).

7.6.2 BASE OVERTURNING MOMENT COEFFICIENTS

The base overturning moments were calculated by taking the average fluctuating pressure on each face of the model. Assigning an appropriate area for each group of five taps , the load can be estimated and then multiplied by the moment arm of that area.

To render the comparison of the results easier, the mean and the standard deviation of the base overturning moment in both x and y directions were normalized by $\frac{1}{2} \rho \bar{V}^2 H^2 D_y$

Thus, we obtain

$$C_{\bar{M}_x} = \frac{M_x}{Q} \qquad (5.a)$$

$$C_{\bar{M}_y} = \frac{M_y}{Q} \qquad (5.b)$$

$$C_{\sigma M_x} = \frac{\sigma M_x}{Q} \qquad (5.c)$$

$$C_{\sigma M_y} = \frac{\sigma M_y}{Q} \qquad (5.d)$$

Where

$$Q = \tfrac{1}{2} \rho \bar{V}^2 H^2 D_y$$

M_x , M_y = mean base overturning moment in the x and y directions, and

σ_{M_x} , σ_{M_y} = standard deviation of base overturning moments in the x and y directions.

Table 11 represents a summary of the above coefficients for the model under various wind directions.

7.6.3 PRESSURE PATTERNS

The equal pressure contour lines were constructed from the mean and the rms values of the pressure coefficients that had been obtained at each pressure tap location. They were constructed by joining equal values of the pressure coefficients on each face, resulting in a series of lines along which the pressure is considered to be constant. Figs. 34 - 49 show the typical results of pressure distribution using contour lines on four faces of the model.

7.6.4 PRESSURE SPECTRA

The fluctuating signals received from the pressure transducer were recorded on a magnetic tape and then fed to a Hewlett Packard 5452A Fourier Analyzer. Each pressure signal was digitized at a rate of 500 - 1000 points per second and stored in blocks of 524 points. The pressure spectra were obtained over the frequency range of up to 500 Hz and normalized as is given in the left hand side of Eq. (2). The resulting pressure spectra were plotted using the on-line HP plotter.

7.7 DISCUSSION OF EXPERIMENTAL RESULTS

7.7.1 PRESSURE DISTRIBUTION AROUND BLUFF BODIES IN GENERAL

It is well known that, in a turbulent flow, the wind velocity increases with the height above ground level. The retardation of flow at lower elevation is caused by the presence of obstacles in the flowpath. Considering a flow over a bluff body such as a tall building, it is easily understood that the flow is separated by the front face and a wake is formed behind the body (Fig. 50). Because of the effect of the inertia force, the wind flow is unable to accelerate around the corner, depending on the wind speed and the geometry of the corner, and separation will occur. Along the separation boundary, a shear layer would be created and it is characterized by the generation of discrete vortices. The point of separation depends on the size and the shape of the body and the wind velocity. For most of the tall buildings the separation point occurs along the sharp corners.

The flow conditions in the wake region can be defined by smaller velocities compared to the mean, upstream flow and a negative pressure compared to the free-stream. The flow stream may also be more complicated, Fig. 51, due to the fluctuation of the oncoming wind and the vortices created in the shear layer. Results of a turbulent flow past a bluff body have shown the dependence of wake and vortex formation on the Reynolds number, Ref. [17].

Theoretical investigation of the above problem has been known to be difficult due to the complexity of the turbulent flow and its interaction with various possibilities of structural shapes. Nevertheless, the flow around building models and other structures can be experimentally investigated in the wind tunnel under similar conditions to the actual problems.

7.7.2 PRESSURE PATTERNS

7.7.2.1 ANGLE OF ATTACK $\beta = 0^{\circ}$, FACING TO WIDE FACE

1- WINDWARD FACE

Figure 34 shows the patterns of pressure contours for the mean pressure coefficients on the wide face, Face 1, which is perpendicular to the wind direction. The contour lines are nearly vertical and the pressure over the face is positive, decreasing in magnitude downwards which depicts the presence of a pressure gradient, which is probably caused by both the oncoming boundary layer and the downward flow on the surface. As a result of the downward flow along the frontal face, higher velocity stream would be generated at lower level of the building as well as the surrounding ground levels. Also, the effects will be extended to the smaller surrounding structures in the immediate vicinity. It is also noticed that the magnitude of pressure decreases towards the edges of the front face as a result of the accelerated flow around the side and upper corners. There

is a formation of an oval concentric shape of the flow pattern at an approximate height of 2/3 H and it represents the centre of the stagnation pressure. The symmetry of the contour lines obtained with respect to a vertical plane through the centre of the face reflects the orthogonality of the model to the mean flow direction.

The variations in the pressure patterns over the front face may be summariezed as follows:

The presence of the bluff body in the flow stream deccelerates the oncoming flow in the longitudinal direction and at a point along the vertical centre line of the body there will exist, for reasons of symmetry, a stagnation pressure varying with the height. Hence, the flow separates symmetrically accelerating in the lateral directions to allow the fluid to pass. Also the layer of air close to the surface, as discussed in Ref. [18], will be subjected to a vertical pressure gradient resulting in a strong downward flow; this effect causes a streamflow of high velocities at the ground level near the structure. Above the stagnation point, The flow will accelerate upward and past the top of the structure. Thus, the top of the structure will be under suction.

The variations in the rms patterns of the pressure contours for the front face are shown in Fig. 34. It is noted that there is a downward decrease in the fluctuating pressure magnitude. That can be attributed to the presence

of higher turbulence around the upper level of the model. For reasons of symmetry and uniformity of the simulated turbulent flow, the rms pressure patterns have shown similarity about a vertical central line along the front face.

2- LEEWARD FACE

Fig. 36 shows the detail of the pressure distribution on the rear face of the model, Face 3. As a result of the suction created in the wake region behind the model, the pressures found on the rear face are negative with the magnitude decreasing slowly towards the centre of the face and throughout the height. A relatively small upward flow will be created as a result of the upward pressure gradient. The superposition of the flow near the top end results in substantial reduction of the suction on the roof. The minimum suction is centred at 2/3 H of the rear face and the maximum suction is found at the upper corner due to the accelerated flow.

The same figure, Fig. 36, illustrates the rms pressure patterns on the rear face. It is noted that the pressure fluctuations are decreasing towards the centre line of the face, and the minimum magnitude is observed at the same height of minimum suction. Meanwhile, the maximum fluctuation is observed along the edges of the rear face, and they seem to be related to the high turbulence generated by the vortices in the shear layer. The pressure

distribution also shows similarity in the contours due to the symmetry of the turbulence and orthogonality of the model with the mean wind direction.

3- PARALLEL FACES

Figs. 35 and 37 show the pressure patterns for the parallel faces of the model. The pressures are negative with increasing magnitude around the corners near the top and near the front edges. The increase in magnitude is a result of the location of separation point near the front corners where the flow is most accelerated.

The rms pressure distributions show increase in the magnitude at lower height and towards the rear edges. It means that the fluctuating component is greater at lower height where there is more turbulence created by the shear layer vortices.

7.7.2.2 ANGLE OF ATTACK $\beta = 90^{\circ}$, FACING TO NARROWER FACE

The pressure patterns around the building model as its short side faces the wind are given in Figs. 38 - 41. The figures illustrate the mean and the rms pressure distributions over the four faces of the building. The observed results may be summarized as follows:

The contour lines show similarity to the pattern of the case when the wide side is facing upstream, except the positive pressure is a little higher in magnitude. Also, the location of the stagnation point is shifted upward. The

fluctuating pressure increases with the height towards the top corner.

The mean and rms pressure distributions on the leeward face, Face 2, show similarity to the previous case of the wide face located in the wake region. The leeward face is under suction but smaller than before in magnitude.

Faces 1 and 3 are parallel to the mean wind direction and the mean pressure is negative, the maximum suction is observed at near the front edges and decreases towards the rear edges. The relatively decreasing pressure magnitude is a result of the downstream flow reattachment which still exhibits negative pressure but lower in magnitude, also the fluctuating components of pressure are increased along the vertical centre line and show no uniformity in distribution.

7.7.2.3 PRESSURE PATTERNS FOR WIND WITH VARIOUS ANGLES

AS it was discussed earlier, the wind direction plays an important role in the pressure distribution around the body. It is worthwhile to show the change in pressure contour lines over the four faces of the building as a function of the wind angle of attack.

Figs. 42 - 49 illustrate the mean and the fluctuating component of the pressure coefficients around the building model for $\beta = 30^{\circ}$ and for 60°. Taking Face 1 for instance, it is observed that the positive pressure decreases in magnitude and gradually changes to negative

pressure as a consequence of the shift in the separation point from the right edge corner to the left edge corner of Face 1. More inportant information on the flow patterns around the building can be obtained by comparison of these figures. They are summarized in the following section.

7.7.3 LOCAL PRESSURE VARIATIONS WITH WIND DIRECTION

Fig. 52 shows the mean and standard deviation of the pressure coefficients for Tap 3, located on the upper middle of Face 1, as a function of wind direction. The mean pressure coefficient varies from the maximum positive value of 0.76 for $\beta = 0^{\circ}$, to the peak negative pressure $Cp = -0.8$ at $\beta = 90^{\circ}$. The transition from positive to negative pressure occures at $\beta = 60^{\circ}$. Increasing the angle of attack, the pressure drops in magnitude to -0.6 at $\beta = 110^{\circ}$ and continues to be constant up to $\beta = 180^{\circ}$. The rms pressure coefficient decreases from 0.18 at $\beta = 0^{\circ}$ to the minimum value of 0.08 at $\beta = 60^{\circ}$, then increases to the peak value of 0.25 at $\beta = 90^{\circ}$. This curve slopes downward again reaching the value of 0.10 at $\beta = 110^{\circ}$ then it continues to be almost constant until it reaches the maximum of 0.15 at $\beta = 180^{\circ}$.

At lower elevations along the same vertical centre-line of Face 1, Figs. 53 - 54 illustrate the variations in Cp and $C\sigma_p$ of Taps 23 and 43 for various angles of attack. Comparison of Figs. 52, 53, and 54 finds similarity in the

general shape of the curves for Cp and C_{σ_p} except the transition from positive to negative pressure and the peak negative pressure are observed at somewhat different angles. The maximum positive pressure is always at $\beta = 0^{\circ}$ and the negative pressure near $\beta = 90^{\circ}$. The peak fluctuating pressure coefficient is always found near $\beta = 90^{\circ}$ as a consequence of the vortices generated from the shear layers after flow separation. The increase in the mean and fluctuating pressure coefficients at $\beta = 180^{\circ}$ predicts that the centre of background flow in the wake region is concentric with the vertical centre-line of the leeward face which is also associated with a high degree of turbulence.

The mean and rms pressure coefficients at the three taps, namely Tap 8, 28, and 48, located on Face 2, are shown in Figs. 55 - 57. The general shape of the curves exhibits similarity to the preceding case, except that the magnitude of the mean and fluctuating components of the pressure are higher and the shifting point from pressure to suction is observed near $\beta = 60^{\circ}$.

To find out the effect of varying the wind direction on the pressure located along the corners, Figs. 58 - 60 show the mean and rms pressure coefficients for Taps 1, 21, and 41 respectively. The mean pressure coefficient curves exhibit two peaks; Positive peak at $\beta = 30^{\circ}$ and negative peak at $\beta = 80^{\circ}$. The shifting point from positive to negative is always around $\beta = 60^{\circ}$. The rms curves have two

successive peaks near $\beta = 60^{\circ}$ and 90°. This may be explained as follows; The first peak is due to the high turbulence created at the separation point, the second peak is the result of the vortices shed from the shear layers.

In addition, curves for the mean and rms pressure coefficients for Taps 6, 26 and 46 are shown in Figs. 61 - 63. Thus, comparison with pressure Taps 1, 21, and 41 which are located on the wide face, can be made and the effect of varying the length-to-width ratio of the building model would be shown.

7.7.4 COMPARISON OF RESULTS WITH CAARC REPORT

The mean and standard deviation of the pressure coefficients for the CAARC model building are given in Tables 1 - 10 for various wind directions. A comparison of the experimental results of the present study at the 2/3 height of the building are made with the set of data arranged by Melbourne [11]. Tables 12 - 14 contain the experimental results obtained from six different establishments and results obtained in this study. The results show good degree of agreement and the mean pressure coefficients agree almost with the mean value of the other data. However, the standard deviation of the pressure coefficients showed some discrepancies for some angles of attack. It is interesting to note that the overall rms coefficients were higher in magnitude than the others. To facilitate the comparison, the same results are plotted in Figs. 64 - 67 for graphical representation.

In addition, Fig. 68 shows the effect of wind direction on the building response, presented as the mean and standard deviation of the base overturning moments. The dashed curve has been given by Melbourne to assist in comparing measurements with the scattered data obtained from the six establishments. However, Fig. 68 shows a good agreement of the mean base overturning moment coefficients found in this investigation with the fitted curve. In contrast to the mean, the rms of the base overturning moment coefficients shows a little more discrepancy.

This relatively poorer agreement may be attributed, as it was suggested by Melbourne, to the behaviour of the shear layers and attendant reattachment, which depend on the incident flow turbulence and even accoustic energy in the wind tunnel. It was also noticed that these effects on shear layer behaviour become more apparent when the flow direction is almost normal to a building face.

It should be mentioned that the response results, from the six establishments, have been obtained using aeroelastic models. Thus, the good agreement in the results proves the efficacy of using either model.

7.7.5 COMPARISION OF RESULTS WITH THE NATIONAL BUILDING CODE OF CANADA

The National Building Code of Canada (NBC) provides the detailed procedure to estimate the dynamic response of tall buildings subjected to wind loading [19]. This procedure is based on the gust-factor method which is a modified approach of the statistical method derived by A. G. Davenport [20]. It consists of a series of calculations involving the building properties, the wind structure as a function of the surrounding terrain, and the final results are the gust effect factor Cg, which is multiplied by the reference wind pressure q, the exposure factor Ce and the pressure coefficient Cp to obtain the static design pressure. The result is expected to be equivalent to the peak load under the actual turbulent wind. The dynamic response of the CAARC standard building can be found following this detailed procedure and it can be also presented in terms of the base overturning moment coefficients for two different angles of attack, $\beta = 0°$ and $\beta = 90°$. The results are summarized and compared below. It is evident, from the results, that NBC overestimates the wind loading effects on the building.

The overestimation of the results by NBC is probably caused by two factors; first of all, the assumed pressure distribution diagram in the code, Fig. 69, which should be compared with the experimental pressure distribution, Figs. 34 and 36. The comparison shows that the design code coefficients are much larger than the experimental

observation. They are assumed to be constant over the face, while in fact the experimental observation shows that they vary along the width and height of the face. Secondly, due to the gust effect factor which was found to result in higher values for slender structure and for structures with low natural frequency or low damping ,Ref. [21].

ANGLE OF ATTACK,	0°	90°
EXPERIMENTAL, C_M	0.59	0.34
N.B.C. , C_M	0.81	0.72

7.7.6 POWER SPECTRA ANALYSIS

The pressure spectra at various locations and wind directions have been detected and shown in Figs. 70 - 86. The following discussion is to compare and to illustrate the general features of these spectra for various cases.

Figs. 70, 71, and 72 show the pressure spectra for Taps 3, 23, and 43 respectively with the wider side of the building facing upstream. They are characterized by a wide bandwidth which is more pronounced at 2/3 H. A narrower bandwidth pressure spectrum has been obtained for Tap 25 which is located on the corner of the upstream face at 2/3 H (Fig. 73). For the face parallel to the wind direction, a very sharp peak in the pressure spectra appears at the frequency of approximately 30 Hz and the peak tends to be sharper at lower elevation (see Figs. 74, 75, and 76). Fig. 77 shows a similar pressure spectrum at Tap 26 with a sharp peak. The narrow bandwidths are associated with the shear layer which produces higher correlated vortices. The pressure spectra measured on the leeward face have a wide bandwidth, as are seen in Figs. 78 - 80, and the bandwidth is wider at lower elevation. The significant broadening of the bandwidth of the spectra on the rear face is a consequence of the increase in the intensity of turbulence present in the wake region and an increase in the available energy at lower frequencies.

Figs. 81 - 83 show the spectra for the pressure Taps 3, 23, and 43 respectively for 30 degrees wind direction. Comparing with the previous case for 0 degree wind direction, it is seen that the pressure spectra have narrower bandwidth, the tendency is more pronounced at lower level. At the pressure Taps 8, 28, and 48, the spectra have wide bandwidth and characterized by double peaks (see Figs. 84, 85, and 86).

Measurement of the pressure spectra on the CAARC standard building were made at the other establishements, but for different conditions. The pressure spectra most common to all are given in Fig. 87 for pressure Taps 3, and 13 and for 0° wind direction. Comparison of Figs. 71 and 79 with Fig. 87 shows good correlation with the data presented.

Chapter VIII

CONCLUSION

Based on the experimental results obtained in this study, it is clear that the atmospheric boundary layer can be simulated in the wind tunnel to obtain similar wind flow conditions for the building pressure study. The consistency in the experimental results of the fluctuating pressure on the 1:1000 scaled CAARC Standard Tall Building Model has proven the success of the proper simulation and the method used in the experiment. Furthermore, it has been found that very accurate and reliable results have been obtained using an extremely exaggerated linear scale of 1:1000. The pressure distributions and the pressure spectra show the expected levels on the four faces of the model for various wind directions. The mean pressure has shown good agreement with the results from the other six establishments. Meanwhile, the standard deviation has an overall higher magnitude, presumably due to the higher simulated turbulence and to the behaviour of the shear layers. The pressure spectra measured at various locations have shown the expected curve shapes; wide bandwidth for the leeward face, less wide for the windward face, and very narrow bandwidths with sharp peak for the parallel faces.

Comparison of the results with the National Building Code of Canada has proven the latter is very conservative in estimating the wind load response of tall buildings.

However the different approach employed in similating the natural wind characteristics, the size of the model, and the size of the wind tunnel, very consistent and reliable results can be obtained from experiments subjected to wind induced loading.

REFERENCES

1. Surry, D., and Stathopoulos, T., "An Experimental Approach to the Economical Measurement of Spatially Averaged Wind Loads," J. Ind. Aerody., Vol. 2, 1979, PP:385-397.

2. Iberall, A. S., "Attenuation of Oscillatory Pressures in Instrument Lines," RP2115, Journal of Reaserch of the National Bureau of Standards, Vol. 45, 1950, PP:85-108

3. Bergh, H., and Tijdeman, H., "Theoretical and Experimental Results for the Dynamic Response of Pressure Measuring Systems," Report NLR-TR F238, National Aerospace Laboratory, The Nertherlands, 1965.

4. Irwin, H.P.A.H., Cooper, K. R., and Girard, R., "Correction of Distortion Effects Caused by Tubing Systems in Measurements of Fluctuating Pressures," Journal of Industrial Aerodynamics, Vol. 5, 1979, PP:93-107.

5. Stathopoulos, T., "Technique of Pneumatically Averaging Pressures," Research Report Engineering Science, BLWT-2, University of Western Ontario, Dec., 1975.

6. Gumley, S. J., "A Detailed Design Method for Pneumatic Tubing Systems," Proc. Sixth. Int. Conf. on Wind Engineering, Gold Coast, Australia, 1983.

7. Gumley, S. J., "Tubing Systems for Pneumatic Averaging of Fluctuating Pressures," Journal of Wind Engineering and Industrial Aerodynamics, Vol. 12, 1983, PP:189-228.

8. Temkin, S., "Elements of Accoustics," John Wiley & Sons, N.Y., 1981, PP:130-140.

9. Tijdeman, H., and Bergh, H., "The Influence of the Main Flow on the Transfer Function of Tube-Transducer Systems Used for Unsteady Pressure Measurements," Report NLR MP72023U, Nayional Aerospace Laboratory, The Nertherlands, 1965.

10. Wardlow, R. L., and Moss, G. F., "A Simulated Tall Building Model for Comparision of Simulated Natural Winds in Wind Tunnels," C.A.A.R.C., c.c.662m Tech.25, Jan., 1970.

11. Melbourne, W. H., "Comparision of Mesurements on the CAARC Standard Tall Building Model in Simulated Model Wind Flows," Journal of Wind Engineering and Industrial Aerodynamics, Vol. 6, July, 1980, PP:73-88.

12. Irwin, H.P.A.H., "Design and Use of Spires for Natural Wind Simulation," National Reaserch Council of Canada, NAE Report, LRT-LA-233, Aug., 1979.

13. Standen, N. M., "A Spire Array for Generating Thick turbulent Shear Layers for Natural Wind Simulation in Wind Tunnels," T.R. LTR-LA-94, National Aeronautical Establishment, NRC, Ottawa, 1972.

14. Melbourne, W. H., "Comparision of Pressure Measurements Made on A Large Isolated Building in Full and Model Scale," Proc. Third Int. Conf. on Wind Effects on Building and Structures, Tokyo, 1971, PP:253-262.

15. Mak, Y. C., "Effect of Tuned Mass Damper on Wind-Induced Response of Tall Building," T.R. presented in partial fulfillment of the requirement for the degree of M.Eng., University of Ottawa, 1982.

16. Lumley, J. and Panofsky, H., "The Structure of Atmospheric Turbulence," John Wiley & Sons, 1964.

17. Simiu, E., and Scanlan, H. R., "Wind Effect on Structures: An Introduction to Wind Engineering," John Wiley & Sons, 1977.

18. Baines, W. D., "Effect of Velocity Distibution on Wind Loads and Flow Patterns on Building," Proc. First Int. Conf. on Wind Effects on Buildings and Structures, Teddington, 1963, PP:198-225.

19. National Building Code of Canada 1977, Supplement No.4, issued by The Associate Committee on The National Building Code, National Reaserch Council, Ottawa, Canada.

20. Davenport, A. G., "Gust Loading Factors," Journal of the Structural Division, ASCE, Vol.93, No.ST3, Proc. Paper 5255, June, 1967, PP:11-34.

21. Davenport, A. G., and Dalgleish, W. S., "A Preliminary Appraisel of Wind Loading Concepts of The 1970 Canadian National Building Code," Proc. Third Int. Conf. on Effects on Buildings and Structures, Tokyo, 1971, PP:441-450.

Appendix A

TABLES FOR PART I

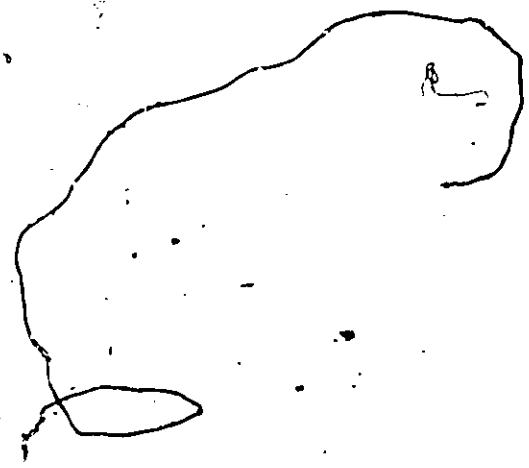

TABLE 1

MEAN AND STANDARD DEVIATION PRESSURE COEFFICIENTS FOR $\beta = 0^{\circ}$

ELEVATION Z								
H			2/3 H			1/3 H		
TAP	$C_{\bar{p}}$	C_{σ_p}	TAP	$C_{\bar{p}}$	C_{σ_p}	Tap	$C_{\bar{p}}$	C_{σ_p}
1	.61	.17	21	.57	.15	41	.56	.15
2	.76	.18	22	.78	.15	42	.55	.10
3	.77	.18	23	.81	.16	43	.59	.14
4	.76	.18	24	.78	.15	44	.56	.14
5	.57	.16	25	.55	.14	45	.38	.14
6	-.66	.21	26	-.65	.25	46	-.70	.27
7	-.68	.22	27	-.65	.24	47	-.72	.28
8	-.66	.22	28	-.66	.27	48	-.73	.28
9	-.65	.22	29	-.68	.28	49	-.73	.27
10	-.64	.20	30	-.74	.30	50	-.75	.29
11	-.59	.17	31	-.51	.20	51	-.57	.21
12	-.59	.16	32	-.46	.15	52	-.55	.17
13	-.60	.15	33	-.45	.14	53	-.52	.15
14	-.59	.15	34	-.47	.17	54	-.54	.18
15	-.57	.17	35	-.54	.20	55	-.57	.20
16	-.65	.22	36	-.74	.29	56	-.75	.30
17	-.67	.23	37	-.69	.29	57	-.72	.29
18	-.70	.23	38	-.68	.28	58	-.74	.29
19	-.66	.24	39	-.67	.27	59	-.74	.29
20	-.65	.25	40	-.66	.27	60	-.72	.28

TABLE 2

MEAN AND STANDARD DEVIATION PRESSURE COEFFICIENTS FOR $\beta = 10^{\circ}$

ELEVATION Z								
H			2/3 H			1/3 H		
TAP	$C_{\bar{p}}$	C_{σ_p}	TAP	$C_{\bar{p}}$	C_{σ_p}	TAP	$C_{\bar{p}}$	C_{σ_p}
1	.67	.18	21	.64	.16	41	.62	.15
2	.78	.18	22	.80	.15	42	.60	.10
3	.73	.18	23	.82	.15	43	.59	.14
4	.68	.18	24	.71	.15	44	.53	.13
5	.45	.15	25	.44	.13	45	.31	.12
6	-.54	.14	26	-.53	.15	46	-.56	.16
7	-.55	.14	27	-.55	.16	47	-.59	.18
8	-.56	.15	28	-.55	.17	48	-.59	.18
9	-.59	.15	29	-.60	.18	49	-.61	.19
10	-.61	.16	30	-.60	.24	50	-.67	.25
11	-.55	.14	31	-.44	.13	51	-.50	.14
12	-.54	.13	32	-.44	.11	52	-.47	.11
13	-.53	.12	33	-.46	.14	53	-.48	.14
14	-.50	.12	34	-.49	.15	54	-.49	.15
15	-.45	.13	35	-.50	.17	55	-.50	.16
16	-.43	.15	36	-.56	.28	56	-.52	.23
17	-.49	.20	37	-.73	.31	57	-.64	.29
18	-.69	.25	38	-.93	.32	58	-.82	.32
19	-.96	.29	39	-1.00	.32	59	-.95	.30
20	-1.10	.30	40	-1.00	.32	60	-.98	.30

TABLE 3

MEAN AND STANDARD DEVIATION PRESSURE COEFFICIENTS FOR $\beta = 20°$

ELEVATION Z								
H			2/3 H			1/3 H		
TAP	$C_{\bar{p}}$	C_{σ_p}	TAP	$C_{\bar{p}}$	C_{σ_p}	TAP	$C_{\bar{p}}$	C_{σ_p}
1	.78	.18	21	.70	.16	41	.69	.15
2	.75	.18	22	.77	.15	42	.61	.10
3	.69	.17	23	.75	.14	43	.58	.13
4	.54	.16	24	.62	.13	44	.49	.12
5	.32	.14	25	.36	.12	45	.27	.11
6	-.46	.10	26	-.38	.10	46	-.42	.10
7	-.45	.09	27	-.40	.10	47	-.45	.09
8	-.46	.10	28	-.42	.10	48	-.45	.10
9	-.47	.10	29	-.44	.11	49	-.47	.11
10	-.49	.11	30	-.46	.13	50	-.51	.14
11	-.45	.10	31	-.35	.10	51	-.39	.09
12	-.42	.09	32	-.34	.08	52	-.39	.08
13	-.41	.09	33	-.34	.08	53	-.40	.09
14	-.38	.09	34	-.35	.08	54	-.40	.09
15	-.38	.09	35	-.35	.08	55	-.40	.09
16	-.32	.08	36	-.25	.12	56	-.30	.11
17	-.18	.09	37	-.22	.19	57	-.25	.17
18	-.18	.16	38	-.38	.30	58	-.36	.26
19	-.41	.28	39	-.70	.31	59	-.57	.30
20	-.98	.24	40	-.83	.21	60	-.80	.24

TABLE 4

MEAN AND STANDARD DEVIATION PRESSURE CORFFICIENTS FOR $\beta = 30^{\circ}$

ELEVATION Z								
H			2/3 H			1/3 H		
TAP	$C_{\bar{p}}$	C_{σ_p}	TAP	$C_{\bar{p}}$	C_{σ_p}	TAP	$C_{\bar{p}}$	$C_{\sigma p}$
1	.89	.19	21	.83	.16	41	.80	.13
2	.75	.17	22	.78	.14	42	.56	.10
3	.61	.16	23	.68	.13	43	.50	.12
4	.47	.15	24	.52	.11	44	.38	.10
5	.18	.12	25	.21	.09	45	.14	.09
6	-.48	.07	26	-.43	.08	46	-.46	.09
7	-.49	.08	27	-.44	.09	47	-.47	.08
8	-.49	.09	28	-.47	.09	48	-.48	.09
9	-.53	.09	29	-.49	.09	49	-.50	.09
10	-.54	.10	30	-.50	.10	50	-.55	.11
11	-.50	.09	31	-.42	.09	51	-.44	.10
12	-.47	.09	32	-.41	.08	52	-.46	.08
13	-.44	.08	33	-.44	.08	53	-.45	.08
14	-.45	.07	34	-.43	.08	54	-.44	.08
15	-.43	.08	35	-.42	.08	55	-.44	.07
16	-.28	.07	36	-.26	.07	56	-.27	.07
17	-.05	.09	37	-.05	.07	57	-.09	.08
18	.05	.09	38	.05	.10	58	-.03	.10
19	.09	.11	39	.05	.24	59	-.01	.18
20	.23	.28	40	-.29	.26	60	-.30	.26

TABLE 5

MEAN AND STANDARD DEVIATION PRESSURE COEFFICIENTS FOR $\beta = 40^{\circ}$

ELEVATION Z								
H			2/3 H			1/3 H		
TAP	$C_{\bar{p}}$	C_{σ_p}	TAP	$C_{\bar{p}}$	C_{σ_p}	TAP	$C_{\bar{p}}$	C_{σ_p}
1	.71	.16	21	.76	.15	41	.71	.12
2	.63	.15	22	.63	.13	42	.44	.09
3	.44	.13	23	.48	.12	43	.36	.11
4	.29	.12	24	.33	.10	44	.22	.09
5	.03	.10	25	.09	.08	45	.02	.08
6	-.46	.08	26	-.41	.09	46	-.41	.09
7	-.47	.08	27	-.41	.09	47	-.44	.09
8	-.45	.08	28	-.43	.09	48	-.42	.09
9	-.47	.08	29	-.44	.09	49	-.46	.09
10	-.49	.09	30	-.46	.09	50	-.50	.12
11	-.46	.09	31	-.43	.09	51	-.44	.10
12	-.46	.09	32	-.42	.08	52	-.44	.08
13	-.44	.09	33	-.41	.08	53	-.43	.08
14	-.44	.08	34	-.40	.08	54	-.41	.08
15	-.43	.08	35	-.39	.08	55	-.41	.08
16	-.15	.08	36	-.11	.08	56	-.16	.08
17	.13	.11	37	.14	.09	57	.08	.08
18	.28	.12	38	.26	.10	58	.19	.09
19	.34	.13	39	.36	.11	59	.28	.11
20	.41	.18	40	.43	.22	60	.30	.20

TABLE 6

MEAN AND STANDARD DEVIATION PRESSURE COEFFICIENTS FOR $\beta = 50^{\circ}$

ELEVATION Z								
H			2/3 H			1/3 H		
TAP	$C_{\bar{p}}$	C_{σ_p}	TAP	$C_{\bar{p}}$	C_{σ_p}	TAP	$C_{\bar{p}}$	C_{σ_p}
1	.55	.15	21	.62	.14	41	.60	.12
2	.36	.13	22	.46	.11	42	.34	.08
3	.23	.12	23	.31	.10	43	.26	.09
4	.12	.10	24	.17	.08	44	.11	.08
5	-.11	.08	25	-.04	.07	45	-.07	.07
6	-.45	.09	26	-.41	.09	46	-.42	.08
7	-.46	.08	27	-.41	.08	47	-.42	.08
8	-.46	.09	28	-.42	.09	48	-.43	.09
9	-.47	.09	29	-.42	.09	49	-.45	.09
10	-.48	.09	30	-.43	.10	50	-.48	.11
11	-.51	.09	31	-.47	.10	51	-.47	.10
12	-.49	.09	32	-.46	.08	52	-.45	.08
13	-.48	.09	33	-.45	.08	53	-.45	.08
14	-.47	.09	34	-.44	.08	54	-.42	.08
15	-.45	.09	35	-.42	.08	55	-.42	.08
16	-.01	.10	36	.01	.09	56	-.04	.08
17	.34	.13	37	.29	.11	57	.23	.10
18	.48	.14	38	.45	.12	58	.34	.10
19	.60	.16	39	.59	.13	59	.44	.12
20	.77	.18	40	.74	.16	60	.53	.15

TABLE 7

MEAN AND STANDARD DEVIATION PRESSURE COEFFICIENTS FOR $\beta = 60^{\circ}$

ELEVATION Z								
H			2/3 H			1/3 H		
TAP	$C_{\bar{p}}$	C_{σ_p}	TAP	$C_{\bar{p}}$	C_{σ_p}	TAP	$C_{\bar{p}}$	C_{σ_p}
1	.15	.26	21	.14	.26	41	.10	.25
2	.14	.10	22	.23	.09	42	.15	.06
3	.04	.09	23	.12	.07	43	.09	.07
4	.05	.08	24	.01	.07	44	-.01	.06
5	-.20	.07	25	-.15	.06	45	-.16	.06
6	-.41	.08	26	-.37	.08	46	-.38	.09
7	-.41	.08	27	-.40	.08	47	-.40	.08
8	-.42	.08	28	-.39	.08	48	-.41	.08
9	-.42	.09	29	-.39	.08	49	-.41	.08
10	-.45	.09	30	-.40	.09	50	-.42	.11
11	-.50	.09	31	-.51	.11	51	-.50	.11
12	-.49	.08	32	-.46	.09	52	-.48	.08
13	-.48	.09	33	-.44	.09	53	-.45	.08
14	-.47	.09	34	-.43	.08	54	-.44	.08
15	-.46	.09	35	-.42	.08	55	-.42	.08
16	.14	.12	36	.17	.10	56	.07	.10
17	.49	.14	37	.48	.12	57	.35	.11
18	.63	.16	38	.61	.13	58	.45	.12
19	.73	.16	39	.71	.14	59	.55	.14
20	.84	.17	40	.76	.16	60	.59	.14

TABLE 8

MEAN AND STANDARD DEVIATION PRESSURE COEFFICIENTS FOR $\beta = 70^{\circ}$

ELEVATION Z								
H			2/3 H			1/3 H		
TAP	$C_{\bar{p}}$	C_{σ_p}	TAP	$C_{\bar{p}}$	C_{σ_p}	TAP	$C_{\bar{p}}$	C_{σ_p}
1	-.79	.26	21	-.63	.23	41	-.63	.24
2	-.09	.18	22	-.20	.28	42	-.18	.15
3	-.09	.08	23	-.05	.13	43	-.04	.13
4	-.15	.07	24	-.09	.08	44	-.09	.08
5	-.27	.07	25	-.20	.07	45	-.19	.07
6	-.37	.09	26	-.31	.08	46	-.34	.08
7	-.37	.09	27	-.33	.08	47	-.34	.08
8	-.35	.09	28	-.32	.08	48	-.35	.08
9	-.39	.09	29	-.32	.08	49	-.34	.08
10	-.42	.09	30	-.31	.09	50	-.34	.09
11	-.51	.11	31	-.50	.15	51	-.55	.14
12	-.48	.10	32	-.44	.11	52	-.47	.10
13	-.48	.10	33	-.42	.10	53	-.48	.10
14	-.47	.09	34	-.40	.10	54	-.45	.09
15	-.49	.10	35	-.37	.09	55	-.44	.09
16	.38	.15	36	.39	.12	56	.25	.11
17	.69	.16	37	.68	.14	57	.50	.13
18	.81	.17	38	.77	.15	58	.60	.14
19	.84	.18	39	.83	.15	59	.65	.14
20	.86	.17	40	.78	.15	60	.59	.14

TABLE 9

MEAN AND STANDARD DEVIATION PRESSURE COEFFICIENTS FOR $\beta = 80^{\circ}$

ELEVATION Z								
H			2/3 H			1/3 H		
TAP	$C_{\bar{p}}$	C_{σ_p}	TAP	$C_{\bar{p}}$	C_{σ_p}	TAP	$C_{\bar{p}}$	C_{σ_p}
1	-1.05	.21	21	-.88	.20	41	-.95	.19
2	-.85	.28	22	-.83	.26	42	-.69	.18
3	-.40	.22	23	-.55	.30	43	-.37	.26
4	-.24	.14	24	-.33	.24	44	-.23	.20
5	-.29	.11	25	-.25	.17	45	-.22	.13
6	-.36	.11	26	-.31	.11	46	-.32	.11
7	-.37	.11	27	-.30	.11	47	-.33	.10
8	-.39	.11	28	-.29	.10	48	-.32	.09
9	-.39	.11	29	-.28	.09	49	-.32	.09
10	-.40	.12	30	-.31	.10	50	-.35	.10
11	-.52	.16	31	-.56	.23	51	-.54	.20
12	-.56	.16	32	-.50	.18	52	-.54	.16
13	-.59	.15	33	-.50	.17	53	-.57	.17
14	-.58	.14	34	-.49	.15	54	-.56	.15
15	-.53	.11	35	-.46	.13	55	-.51	.13
16	.54	.16	36	.50	.14	56	.33	.13
17	.81	.17	37	.71	.15	57	.56	.14
18	.91	.17	38	.79	.15	58	.60	.14
19	.87	.18	39	.80	.16	59	.62	.14
20	.74	.18	40	.60	.15	60	.48	.13

TABLE 10

MEAN AND STANDARD DEVIATION PRESSURE COEFFICIENTS FOR $\beta = 90^{\circ}$

ELEVATION Z								
H			2/3 H			1/3 H		
TAP	$C_{\bar{p}}$	C_{σ_p}	TAP	$C_{\bar{p}}$	C_{σ_p}	TAP	$C_{\bar{p}}$	C_{σ_p}
1	-.99	.29	21	-.75	.24	41	-.82	.27
2	-.83	.27	22	-.79	.26	42	-.80	.17
3	-.70	.25	23	-.79	.27	43	-.67	.26
4	-.51	.22	24	-.65	.27	44	-.56	.25
5	-.37	.19	25	-.50	.27	45	-.40	.21
6	-.32	.14	26	-.35	.16	46	-.36	.14
7	-.30	.13	27	-.32	.13	47	-.35	.11
8	-.37	.12	28	-.31	.10	48	-.34	.10
9	-.38	.13	29	-.32	.13	49	-.34	.11
10	-.39	.14	30	-.35	.16	50	-.35	.13
11	-.41	.28	31	-.50	.27	51	-.42	.20
12	-.57	.25	32	-.65	.27	52	-.55	.22
13	-.80	.24	33	-.79	.28	53	-.71	.27
14	-.94	.23	34	-.79	.26	54	-.86	.28
15	-.86	.20	35	-.75	.24	55	-.83	.25
16	.65	.28	36	.53	.15	56	.34	.14
17	.89	.18	37	.79	.16	57	.57	.15
18	.91	.18	38	.82	.16	58	.61	.15
19	.86	.18	39	.78	.15	59	.56	.15
20	.65	.17	40	.56	.15	60	.38	.14

TABLE 11

BASE OVERTURNING MOMENT COEFFICIENTS

β	$C_{\bar{M}_x}$	$C_{\bar{M}_y}$	$C_{\sigma_{M_x}}$	$C_{\sigma_{M_y}}$
0°	.59	-.01	.17	.27
10	.58	-.09	.15	.25
20	.51	-.005	.14	.22
30	.50	.13	.15	.13
40	.43	.22	.155	.14
50	.35	.28	.16	.12
60	.26	.32	.17	.11
70	.12	.35	.19	.095
80	.05	.34	.22	.097
90	.01	.33	.24	.100

TABLE 12

CAARC BUILDING MODEL MEAN PRESSURE COEFFICIENT AT Z =(2/3)H

	TAP 1	2	3	4	5	6	7	8	9	10	
	.59	.84	.87	.80	.54		-.76	-.77		-.84	City
	.49	.76	.80	.80	.53	-.66	-.69	-.70	-.73	-.77	Bristol
	.55	.78	.81	.78	.55	-.64	-.70	-.74	-.75	-.76	Monash
0°	.57	.81	.86	.84	.57	-.66	-.68	-.72	-.71	-.77	NAE(a)
	.54	.76	.81	.78	.49	-.85	-.85	-.88	-.86	-.66	NAE(b)
	.57	.76	.80	.76	.56	-.49	-.52	-.54	-.54	-.58	NPL
	.56	.78	.81	.78	.55	-.65	-.65	-.66	-.68	-.74	Ottawa
	.86	.83	.71	.53	.20	-.46	-.47	-.48	-.50	-.52	Bristol
	.80	.79	.66	.44	.23	-.48	-.49	-.51	-.51	-.52	Monash
30°	.87	.82	.72	.53	.24	-.40	-.42	-.44	-.45	-.48	NAE(a)
	.79	.74	.65	.51	.25	-.35	-.35	-.36	-.36	-.37	NPL
	.83	.78	.68	.52	.21	-.43	-.44	-.47	-.49	-.50	Ottawa
	.14	.23	.14	0	-.20	-.48	-.49	-.51	-.50	-.50	City
	-.03	.24	.14	.01	-.16	-.41	-.42	-.43	-.43	-.43	Bristol
60°	.22	.35	.17	-.04	-.12	-.44	-.43	-.45	-.44	-.44	Monash
	.15	.28	.21	.07	-.12	-.38	-.39	-.39	-.41	-.39	NAE(a)
	.18	.25	.19	.07	-.09	-.32	-.33	-.33	-.33	-.33	NPL
	.14	.23	.12	.01	-.15	-.37	-.40	-.39	-.39	-.40	Ottawa
	-.75	-.79	-.80	-.71	-.57		-.34	-.32		-.38	City
	-.73	-.77	-.78	-.69	-.61	-.40	-.37	-.34	-.39	-.42	Bristol
	-.70	-.75	-.69	-.62	-.55	-.34	-.32	-.32	-.32	-.34	Monash
90°	-.68	-.74	-.73	-.61	-.49	-.33	-.28	-.28	-.28	-.33	NAE(a)
	-.98	-1.01	-.81	-.77	-.66	-.50	-.45	-.45	-.43	-.56	NAE(b)
	-.64	-.70	-.67	-.54	-.41	-.27	-.25	-.23	-.25	-.27	NPL
	-.75	-.79	-.79	-.65	-.50	-.35	-.32	-.31	-.32	-.35	Ottawa

(continued)

TABLE 12 (Continued)

TAP	11	12	13	14	15	16	17	18	19	20	
		-.55	-.53		-.61	-.84	-.82	-.82	-.79	-.75	City
	-.58	-.51	-.50	-.53	-.59	-.76	-.71	-.70	-.70	-.66	Bristol
0°	-.56	-.53	-.51	-.53	-.56	-.77	-.75	-.74	-.70	-.64	Monash
	-.54	-.48	-.45	-.49	-.51	-.77	-.71	-.73	-.69	-.65	NAE(a)
	-.66	-.62	-.58	-.59	-.66	-.64	-.90	-.91	-.86	-.86	NAE(b)
	-.38	-.35	-.34	-.35	-.38	-.56	-.54	-.54	-.53	-.50	NPL
	-.51	-.46	-.45	-.47	-.54	-.74	-.69	-.68	-.67	-.66	Ottawa
											City
	-.44	-.43	-.43	-.44	-.43	-.23	.04	.01	-.01	-.47	Bristol
	-.43	-.45	-.45	-.42	-.39	-.18	.0	-.04	-.22	-.47	Monash
30°	-.40	-.41	-.41	-.39	-.38	-.15	.0	.07	-.02	-.36	NAE(a)
	-.32	-.32	-.33	-.34	-.34	-.12	.0	.08	.03	-.30	NPL
	-.42	-.41	-.44	-.43	-.42	-.26	-.05	.05	.05	-.29	Ottawa
	-.61	-.60	-.56	-.53	-.53	.15	.47	.64	.76	.83	City
	-.53	-.50	-.47	-.47	-.45	.20	.53	.70	.84	.88	Bristol
	-.51	-.51	-.49	-.44	-.41	.22	.49	.60	.69	.78	Monash
60°	-.53	-.49	-.46	-.44	-.41	.22	.51	.68	.81	.86	NAE(a)
	-.37	-.35	-.36	-.35	-.34	.23	.46	.62	.73	.78	NPL
	-.51	-.46	-.44	-.43	-.42	.17	.48	.61	.71	.76	Ottawa
		-.70	-.81		-.76	.57	.81	.87	.81	.56	City
	-.59		-.77	-.79	-.75	.50	.77	.84	.78	.54	Bristol
	-.55	-.62	-.69	-.74	-.70	.56	.75	.79	.75	.56	Monash
90°	-.49	-.61	-.73	-.74	-.68	.55	.82	.88	.82	.55	NAE(a)
	-.65	-.81	-.90	-.99	-.96	.45	.73	.77	.75	.46	NAE(b)
	-.41	-.54	-.67	-.70	-.64	.52	.72	.77	.72	.52	NPL
	-.50	-.65	-.79	-.79	-.75	.53	.79	.82	.78	.56	Ottawa

TABLE 13

CAARC BUILDING MODEL RMS PRESSURE COEFFICIENT AT Z = (2/3)H

TAP	1	2	3	4	5	6	7	8	9	10	
	.14	.14	.15	.15	.13	.16	.19	.18	.21	.23	Bristol
	.15	.18	.19	.18	.15	.22	.22	.23	.26	.27	Monash
0°			.20					.31			NAE(a)
			.22					.27			NAE(b)
	.13	.12	.13	.12	.13	.11	.16	.17	.18	.19	NPL
	.15	.15	.16	.15	.14	.25	.24	.27	.28	.30	Ottawa
	.16	.16	.13	.12	.09	.06	.07	.07	.07	.09	Bristol
30°	.15	.14	.16	.12	.08	.07	.08	.07	.06	.08	Monash
			.15					.17			NAE(a)
											NPL
	.16	.14	.13	.11	.09	.08	.09	.09	.09	.10	Ottawa
	.27	.11	.06	.06	.05	.06	.07	.06	.06	.07	Bristol
60°	.28	.12	.06	.06	.05	.06	.07	.07	.07	.06	Monash
			.09					.15			NAE(a)
											NPL
	.26	.09	.07	.07	.06	.08	.08	.08	.08	.09	Ottawa
	.22	.23	.25	.23	.23	.13	.11	.09	.11	.13	Bristol
	.22	.23	.23	.22	.25	.10	.08	.08	.10	.10	Monash
			.30					.18			NAE(a)
90°			.31					.10			NAE(b)
	.18	.20	.22	.20	.20	.08	.08		.08	.08	NPL
	.24	.26	.27	.27	.27	.16	.13	.10	.13	.16	Ottawa

(continued)

TABLE 13 (Conitnued)

TAP	11	12	13	14	15	16	17	18	19	20	
	.17	.14	.11	.13	.16	.23	.20	.25	.22	.20	Bristol
	.18	.17	.13	.17	.18	.26	.26	.23	.21	.22	Monash
0°			.15					.31			NAE(a)
			.11					.31			NAE(b)
	.09	.06	.05	.06	.09	.19	.18	.18	.16	.11	NPL
	.20	.15	.14	.17	.20	.29	.29	.28	.27	.27	Ottawa
	.07	.06	.06	.06	.06	.05	.06	.15	.24	.24	Bristol
	.08	.07	.08	.06	.07	.08	.06	.18	.32	.24	Monash
30°			.10					.10			NAE(a)
											NPL
	.09	.08	.08	.08	.08	.07	.07	.10	.24	.26	Ottawa
	.10	.07	.06	.06	.06	.09	.13	.13	.17	.18	Bristol
	.12	.07	.07	.07	.07	.10	.14	.13	.15	.18	Monash
60°			.10					.09			NAE(a)
											NPL
	.11	.09	.09	.08	.08	.10	.12	.13	.14	.16	Ottawa
	.23	.24	.25	.24	.23	.14	.16	.16	.17	.15	Bristol
	.26	.21	.22	.22	.22	.14	.15	.16	.14	.13	Monash
90°			.31					.12			NAE(a)
	.20	.20	.22	.20	.18	.12	.13	.12	.13	.12	NPL
	.27	.27	.28	.26	.24	.16	.16	.16	.15	.15	Ottawa

Table 14. CAARC Building Model Wind Tunnel And Modelling Information.

Testing Establishment	Working Section Dimension (m)	Model Scale Parameters		Blockage ratio $\frac{\text{Max. model area}}{\text{Working section}}$	Model Boundary Layer Development
		Length Ratio	Velocity for model pressure measurements		
City University	0.76 x 0.60	$\frac{1}{690}$	15	3.9 %	3 off 0.5 m high elliptic wedge vorticity generators and castellated barrier followed by a 1.6 m fetch of 17 x 17 x 20 mm high roughness elements in staggered array at 90 x 60 m centres.
University of Bristol	2 x 1	$\frac{1}{500}$	12	2.0 %	Semi-elliptic wedge vorticity generators and 100 mm step followed by an array of 50 mm high cups.
Monash University	2 x 2	$\frac{1}{400}$	30	1.3 %	4 off, 2 m high, 4° triangular vorticity generators followed by a 12 m fetch of 20 x 20 x 30 mm roughness elements.
National Aeronatical Establishment	9.1 x 9.1	$\frac{1}{400}$	15	0.06 %	(a) 6 off 1.2 m high spires followed by 7.1 m fetch of 76 mm cube roughness elements on 0.3 m centres staggered array. (b) A 22 m fetch of 76 mm cube roughness elements on 0.3 m centres staggered array. (Spires are not used in this configuration).
National Physical Laboratory	2.7 x 2.1	$\frac{1}{240}$	18.3	2.5 %	Graded horizontal grid of 25.4 mm diameter rods, plus six 76 mm wide vertical slats. Model placed 3.7 m from grid, surrounded roughness for approximately 1.5 m.
University of Western Ontario	2.4 x 2.1	$\frac{1}{500}$		0.6 %	Graded grid of horizontal rods, 300 m high, followed by 25 mm cube roughness elements.
University of Ottawa	0.91 x 0.61	$\frac{1}{1000}$	15.52	1.8 %	3 - 0.406 m high spires followed by 0.914 m fetch of 13 x 13 x 19 mm floor roughness and 0.914m fetch of 13 mm cube roughness elements on 64 mm centres staggered array.

Appendix B

FIGURES FOR PART I

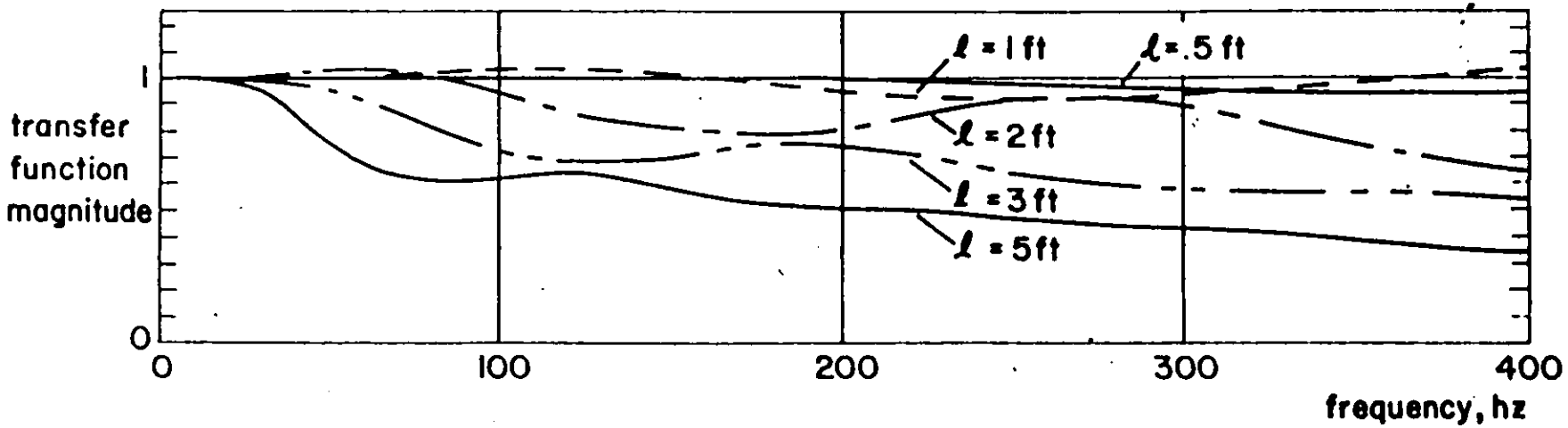

Figure 3. Optimum Transfer Functions With Restrictors in Various Tube Lengths (4).

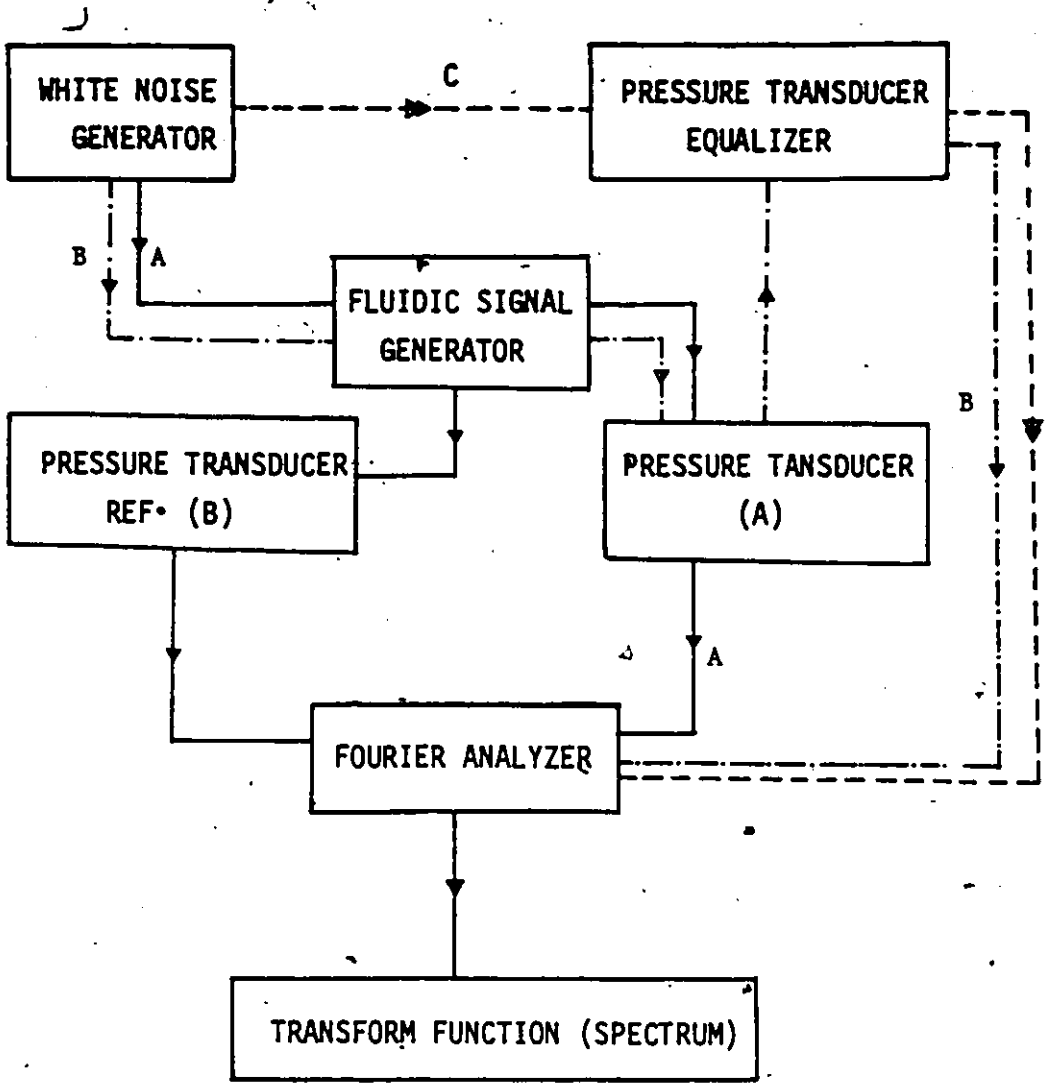

Figure 4. Calibration Aparatus.

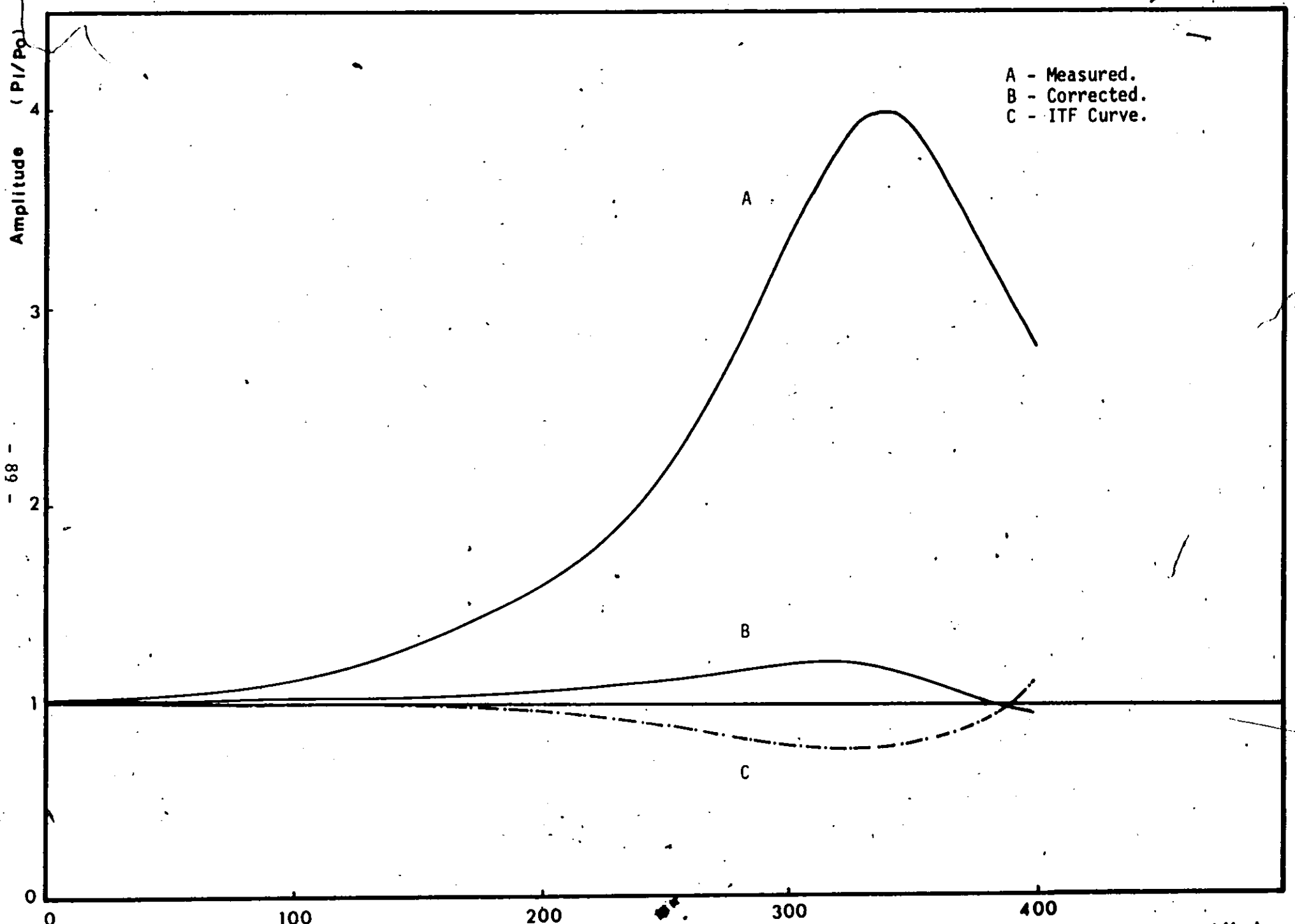

Figure 5. Measured Transfer Function for 1/2 ft. Tube Length.

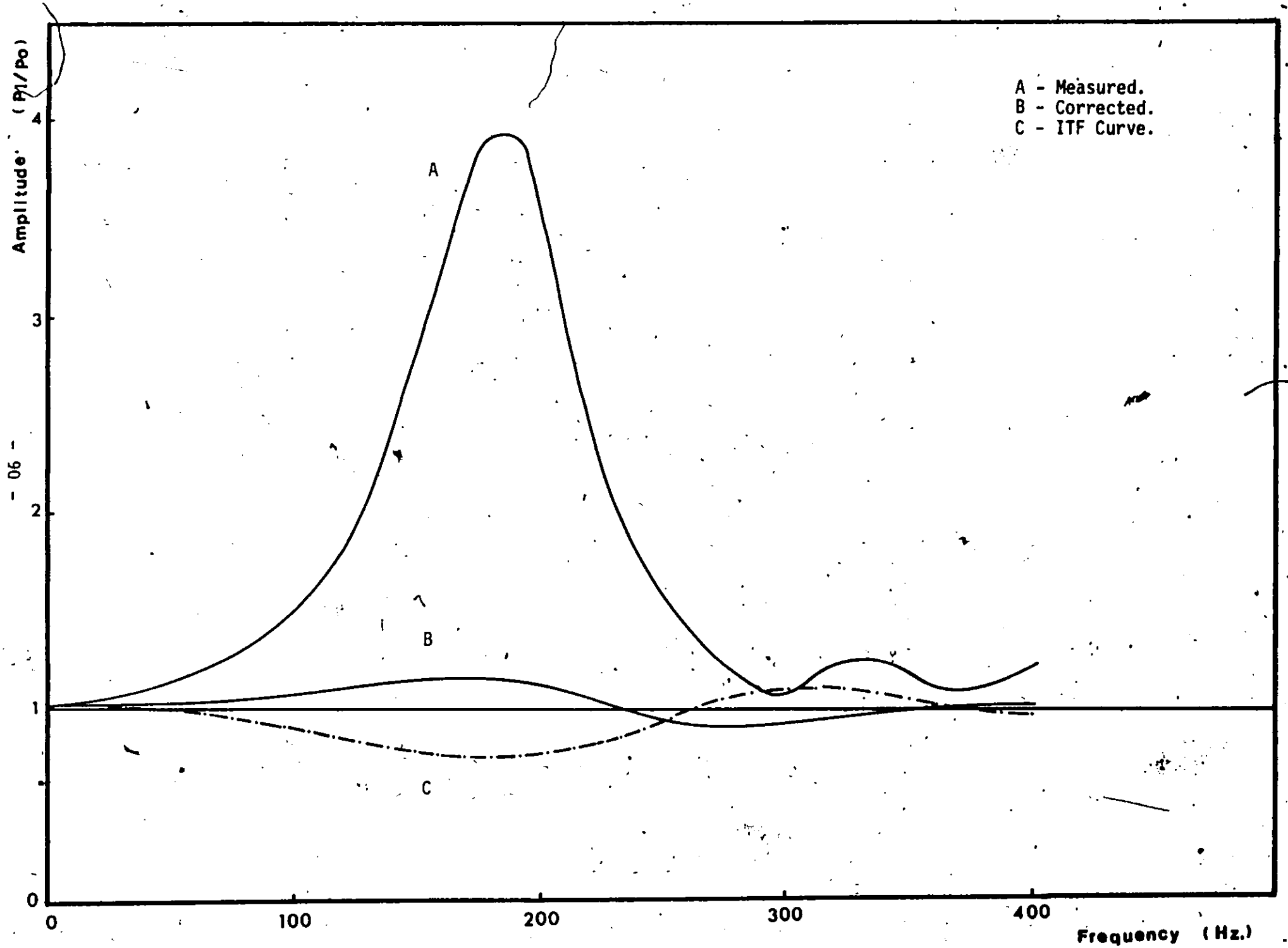

Figure 6. Measured Transfer Function for 1 ft. Tube Length.

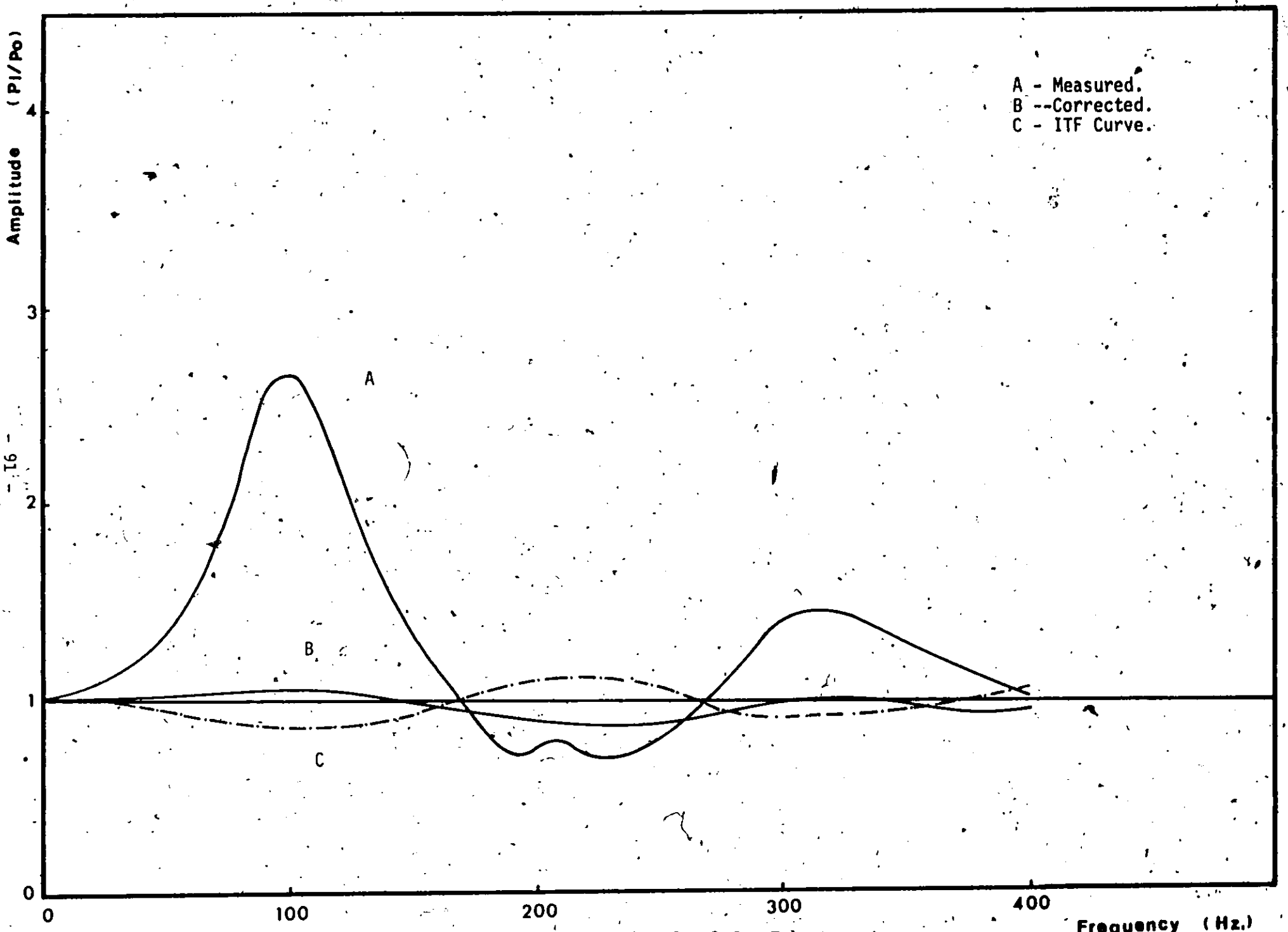

Figure 7. Measured Transfer Function for 2 ft. Tube Length.

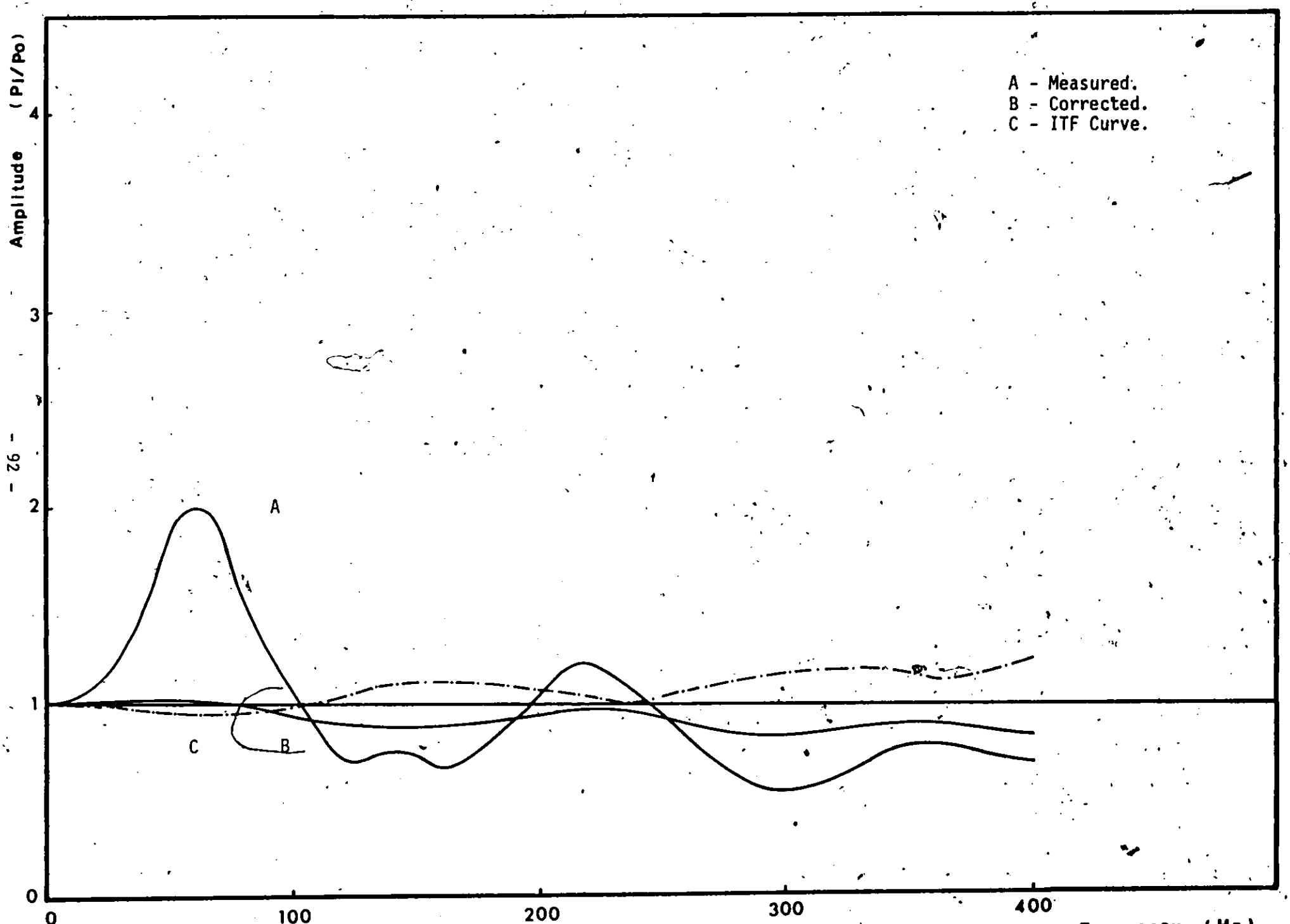

Figure 8. Measured Transfer Function for 3 ft. Tube Length.

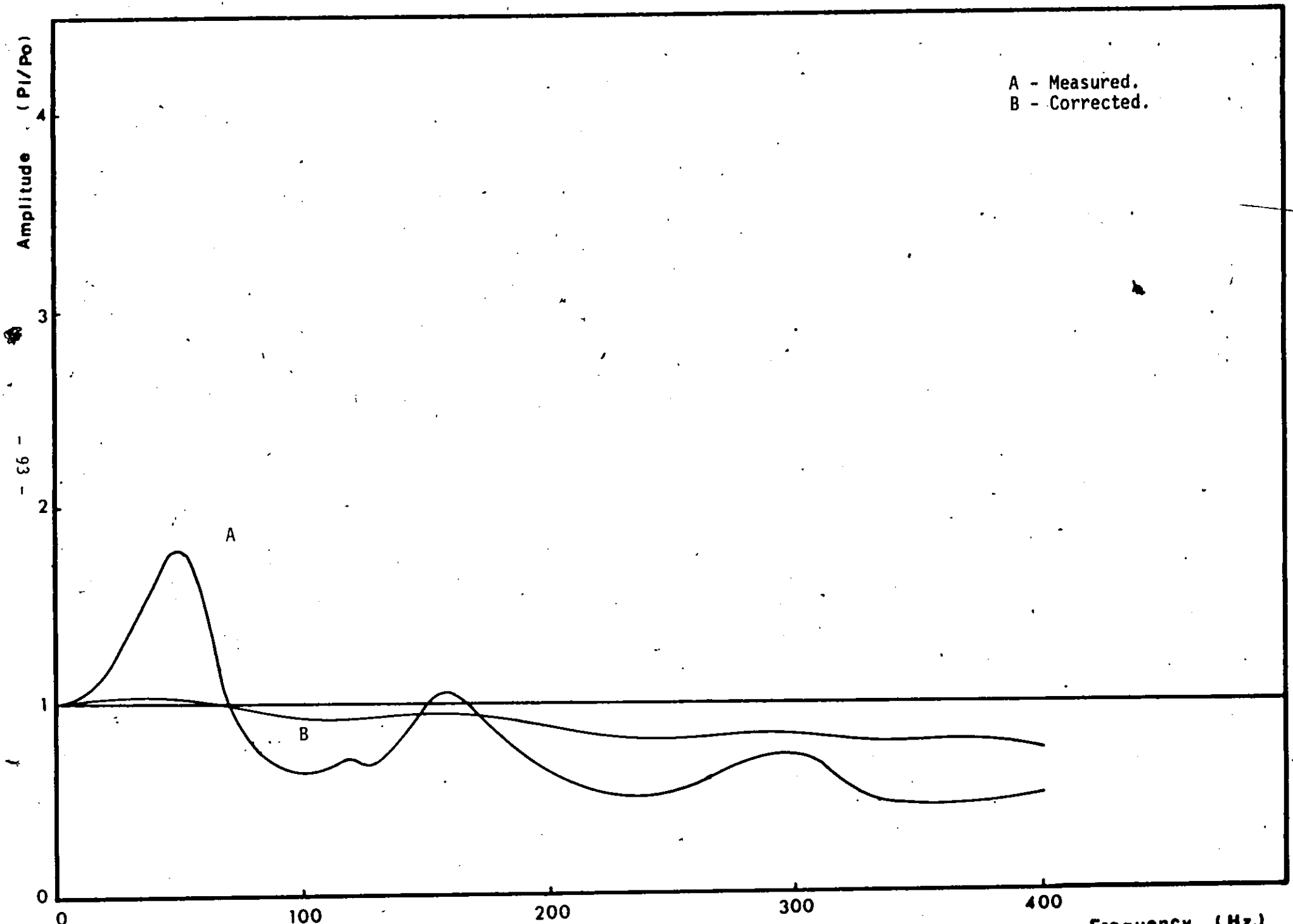

Figure 9. Measured Transfer Function for 4 ft. Tube Length.

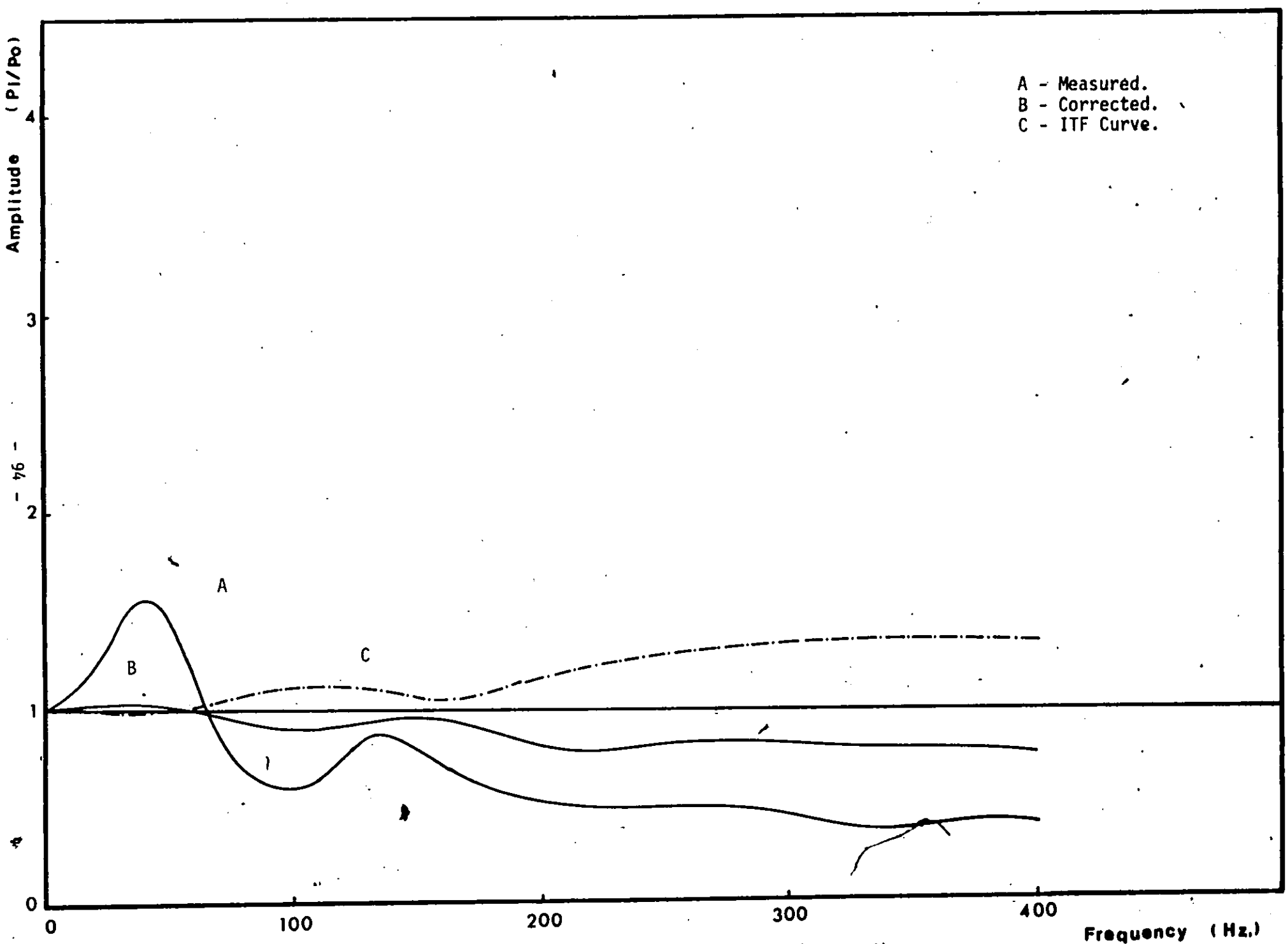

Figure 10. Measured Transfer Function for 5 ft. Tube Length.

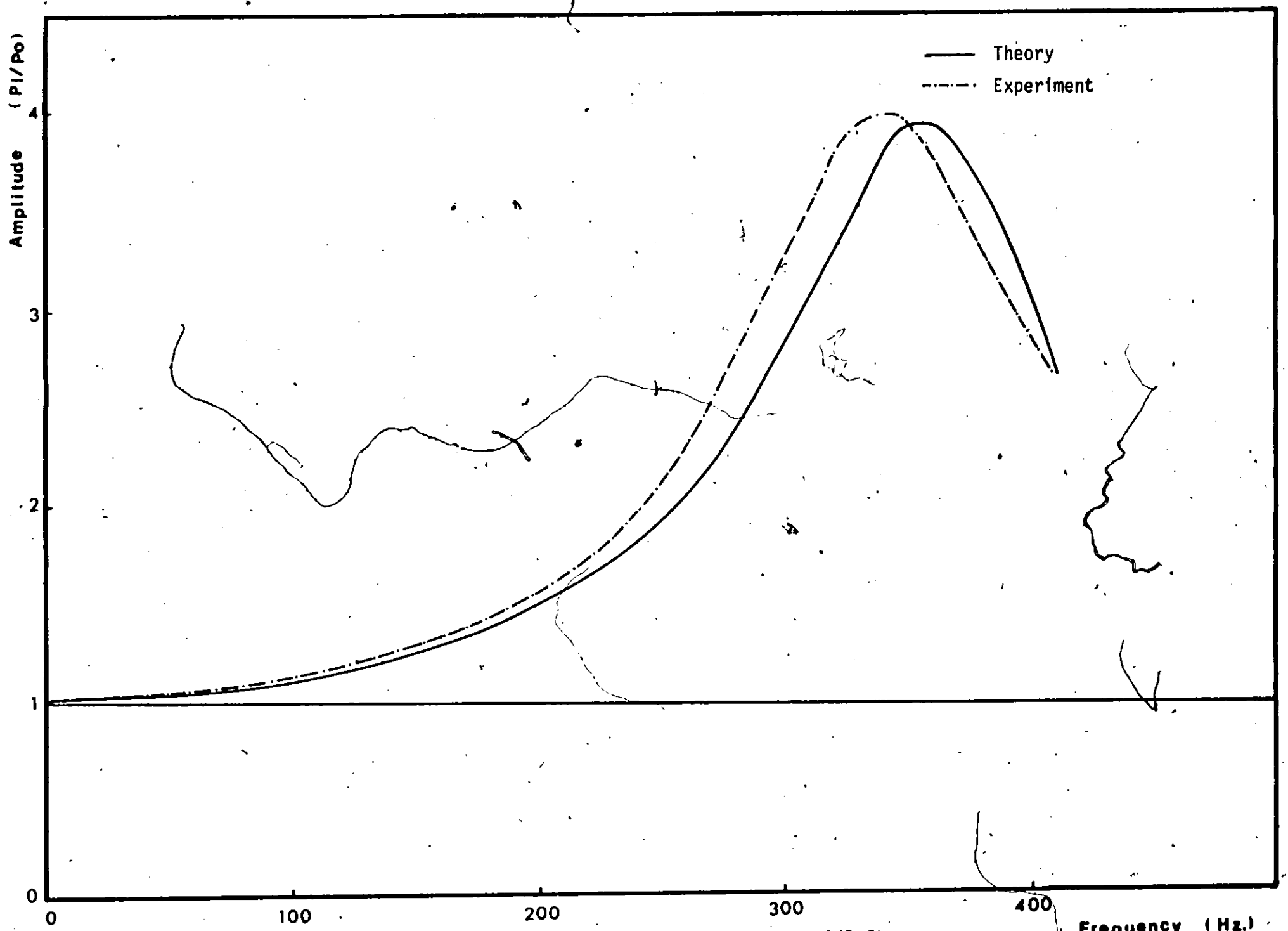

Figure 11. Measured Transfer Function Compared with Theory for L = 1/2 ft.

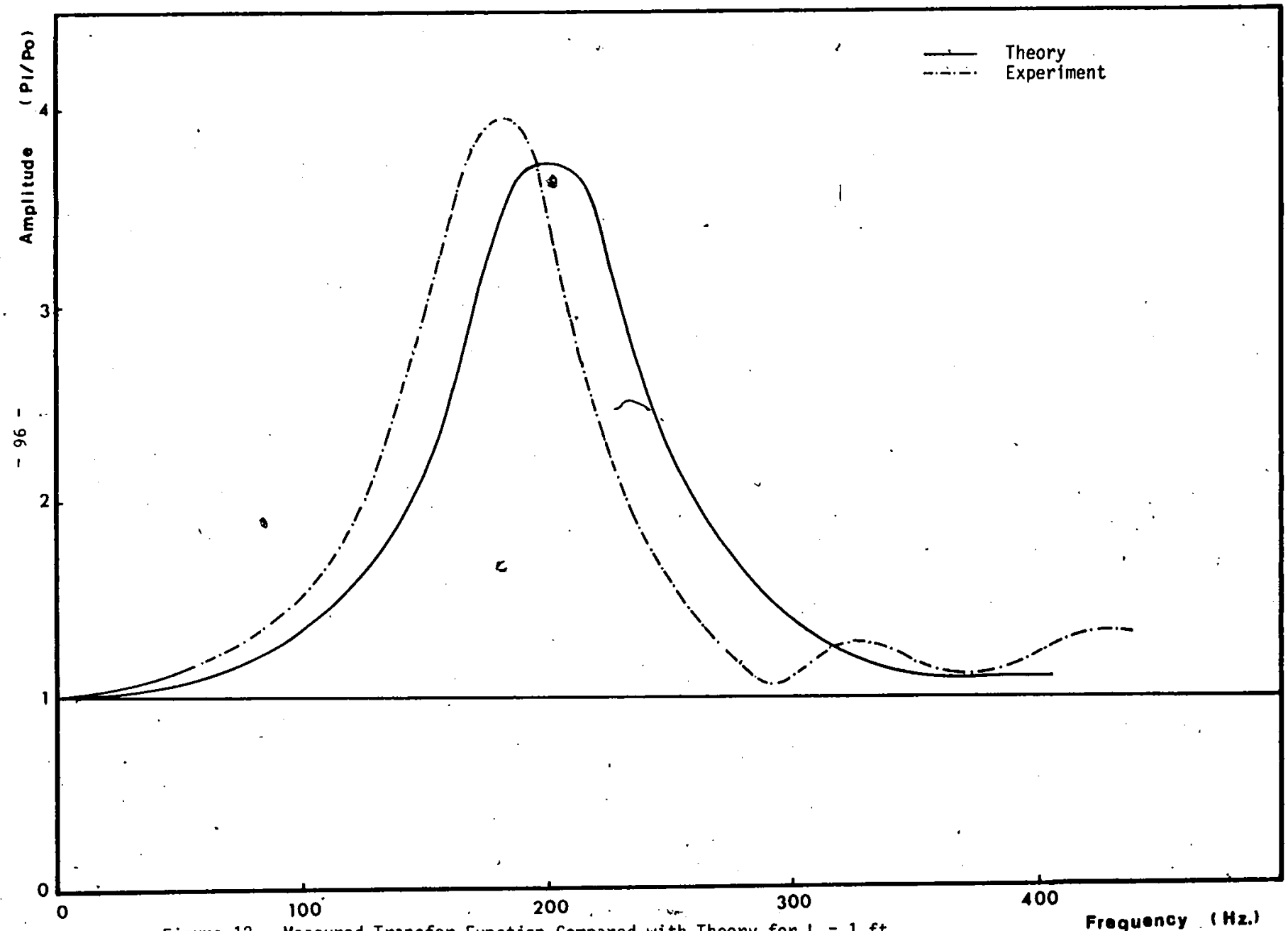

Figure 12. Measured Transfer Function Compared with Theory for L = 1 ft.

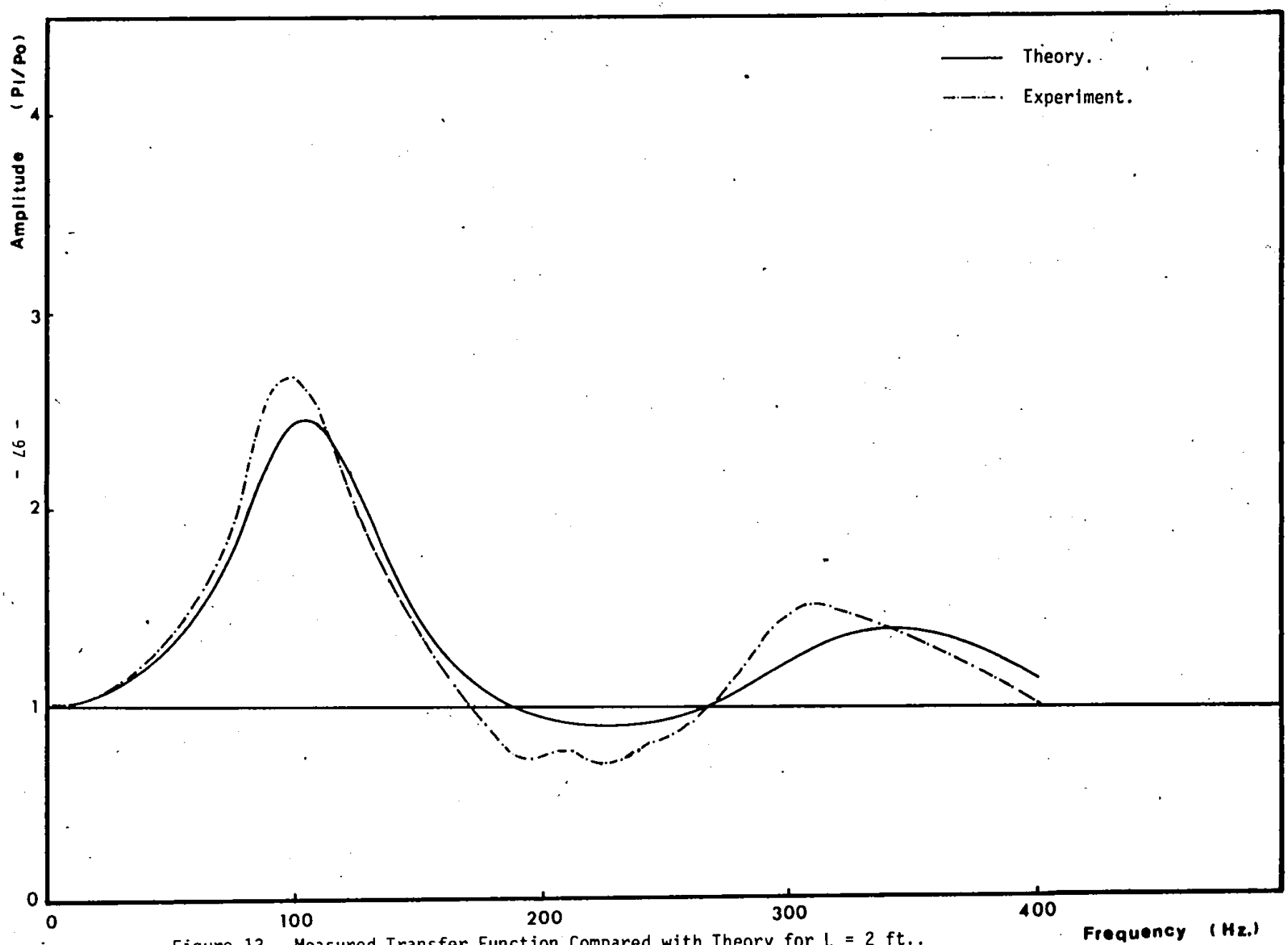

Figure 13. Measured Transfer Function Compared with Theory for L = 2 ft..

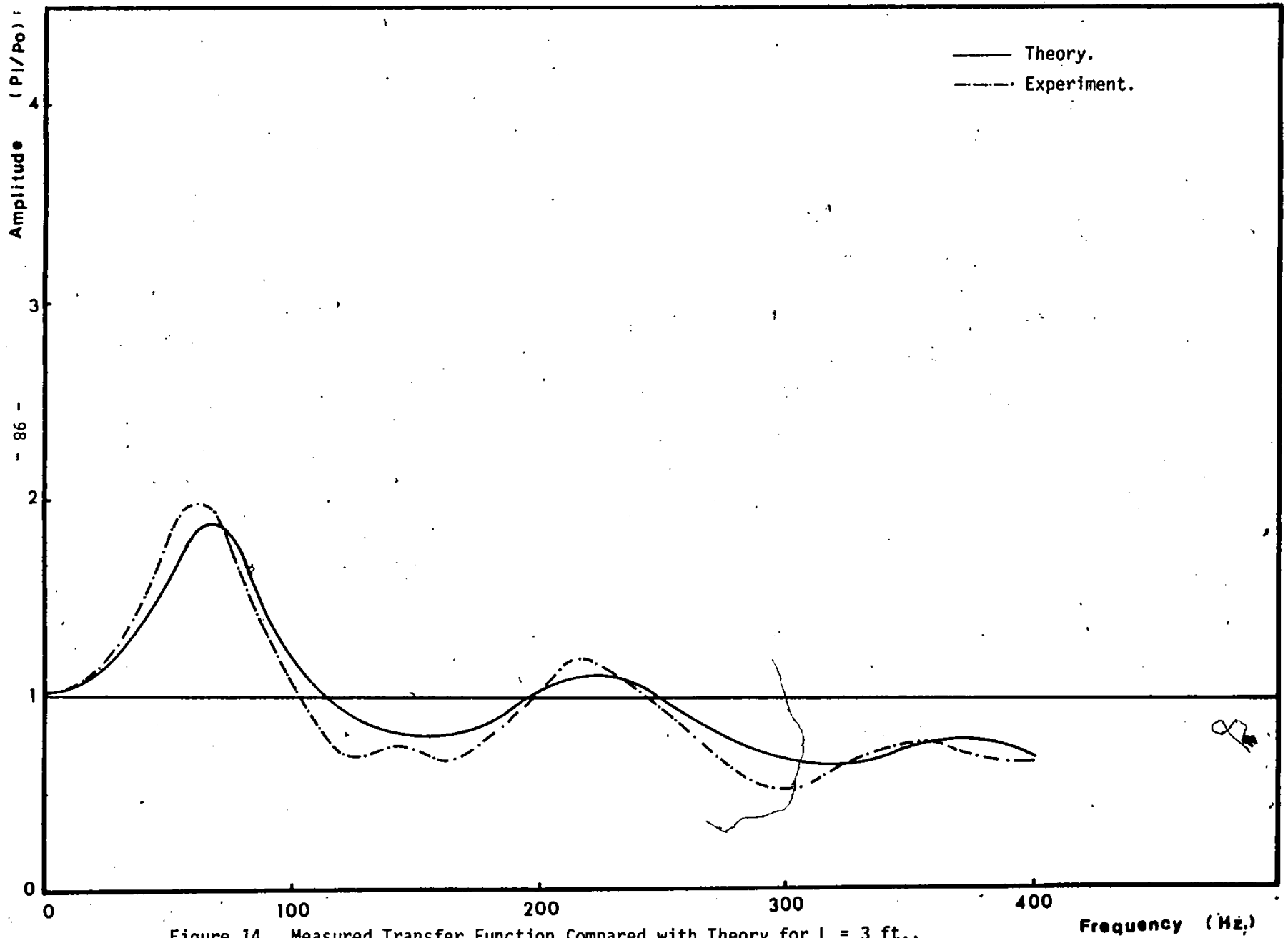

Figure 14. Measured Transfer Function Compared with Theory for L = 3 ft..

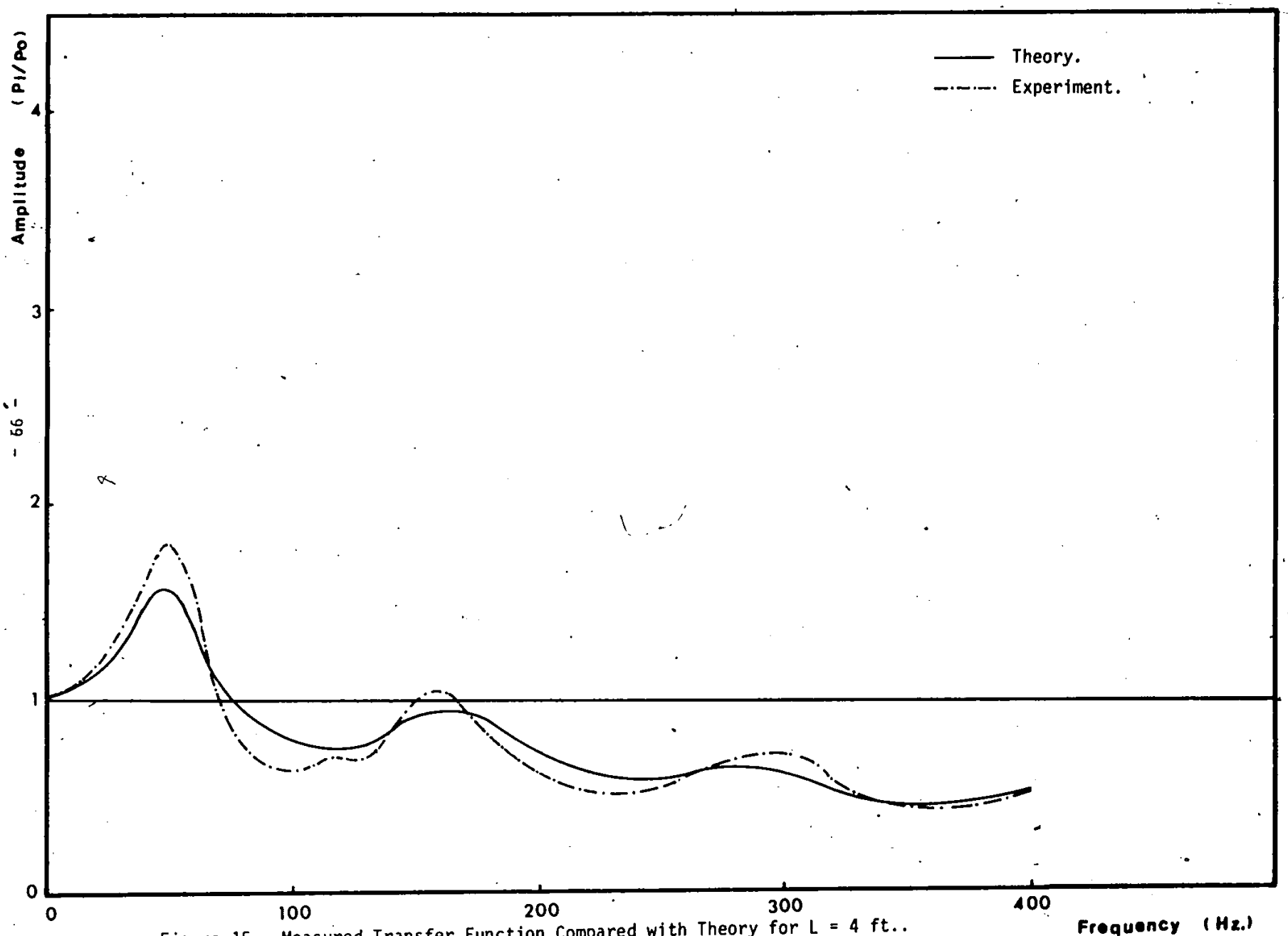

Figure 15. Measured Transfer Function Compared with Theory for L = 4 ft..

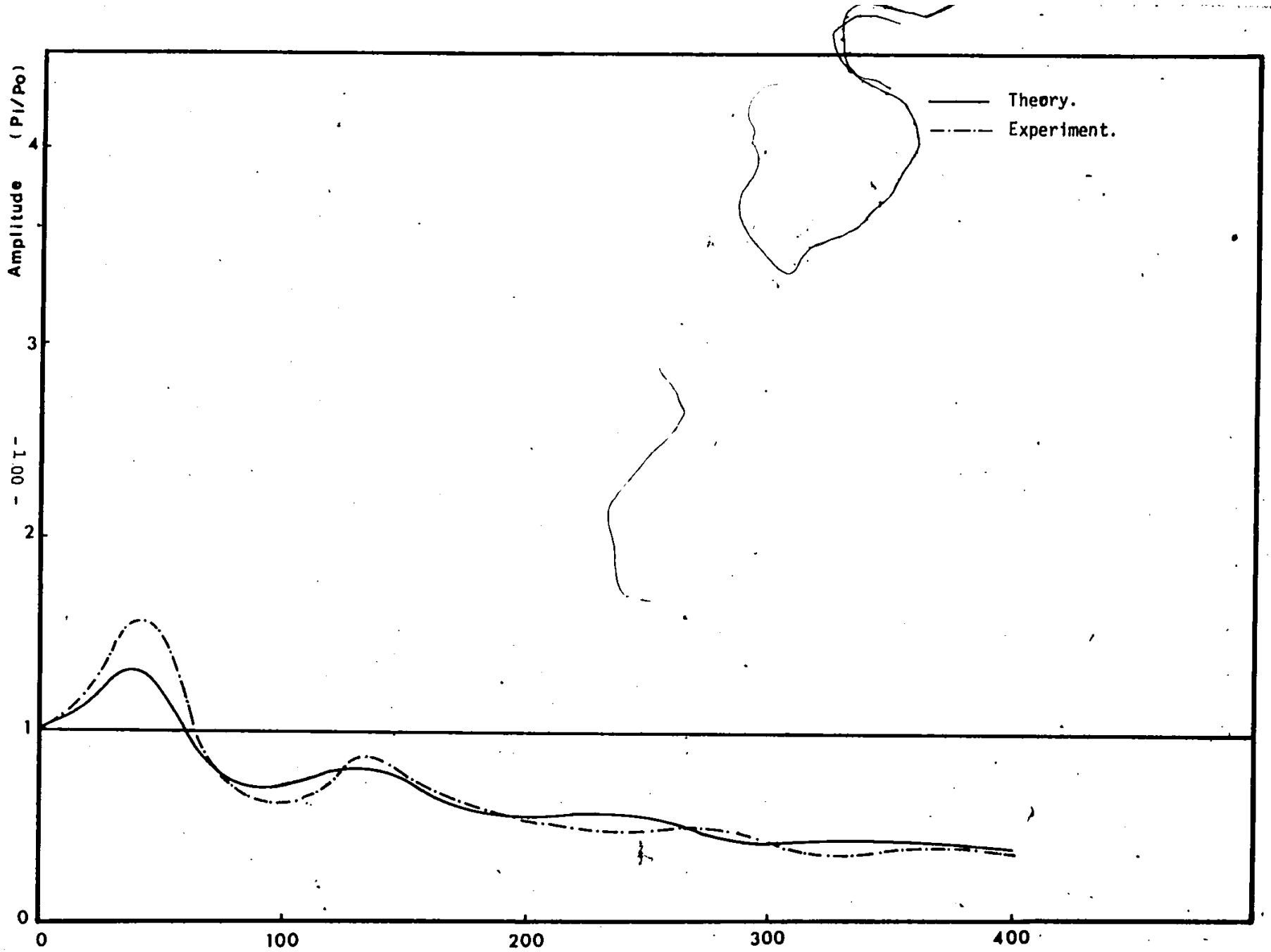

Figure 16. Measured Transfer Function Compared with Theory for L = 5 ft..

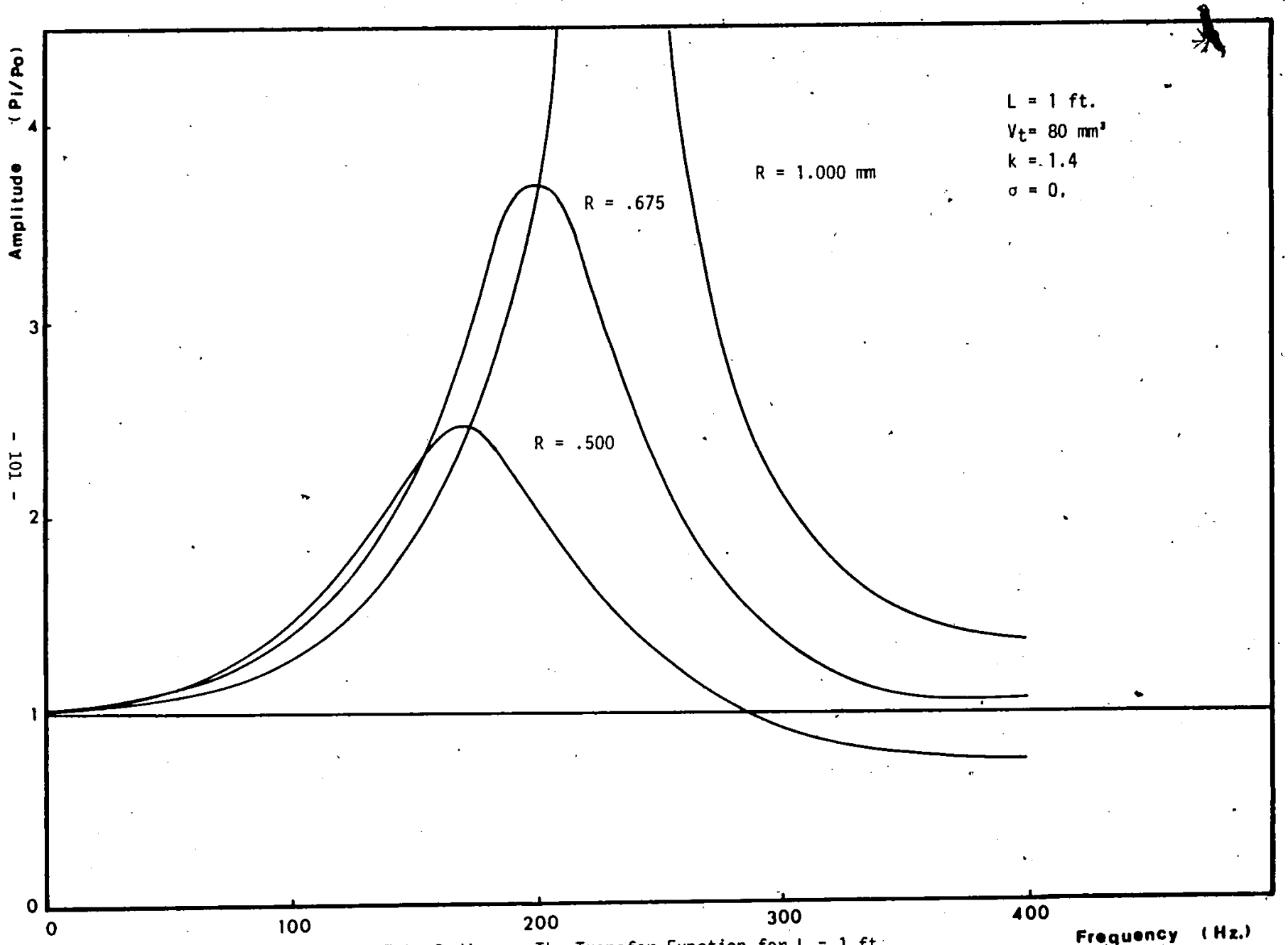

Figure 17. Effect of Tube Radius on The Transfer Function for L = 1 ft..

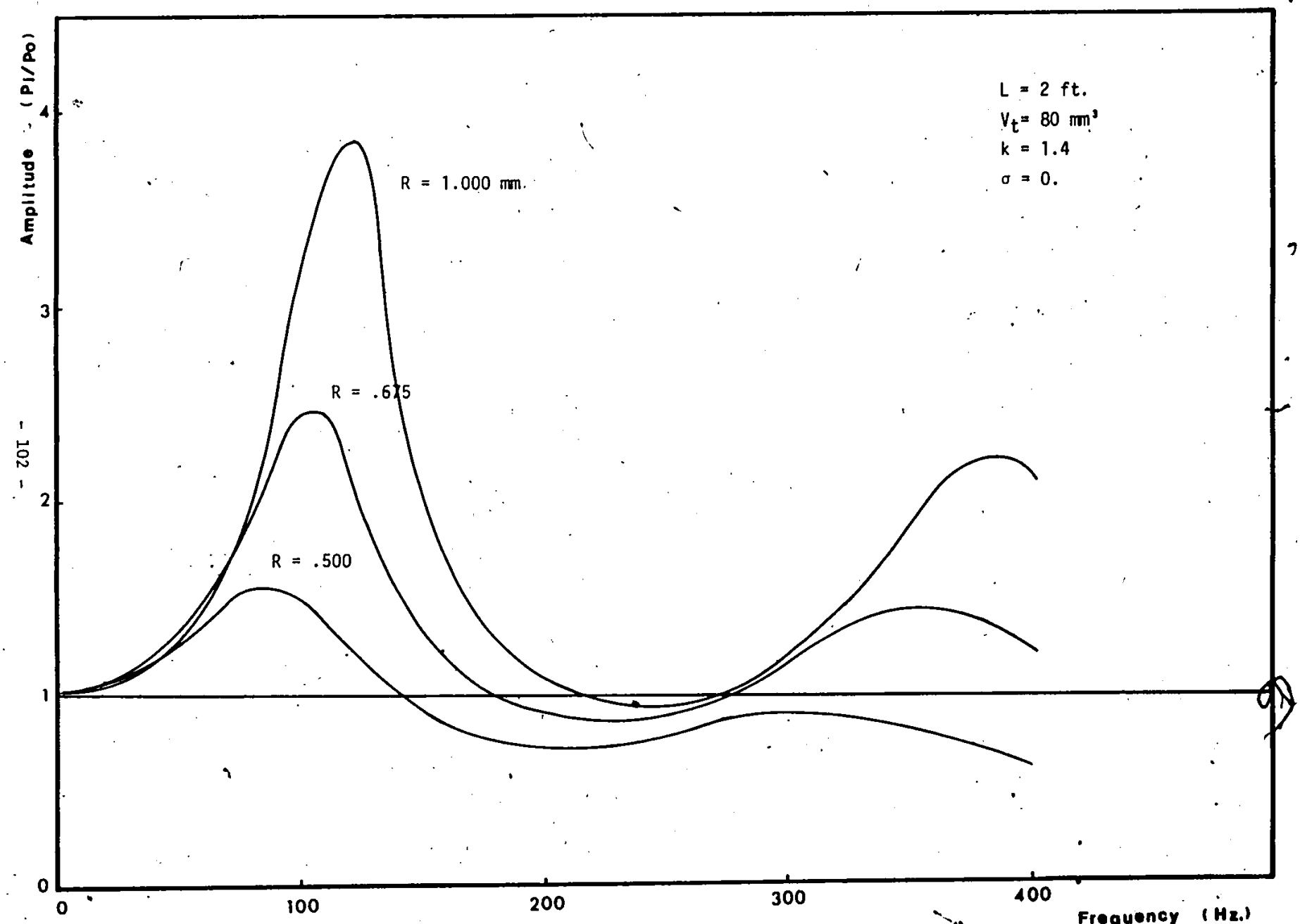

Figure 18. Effect of Tube Radius on the Transfer Function for L = 2 ft..

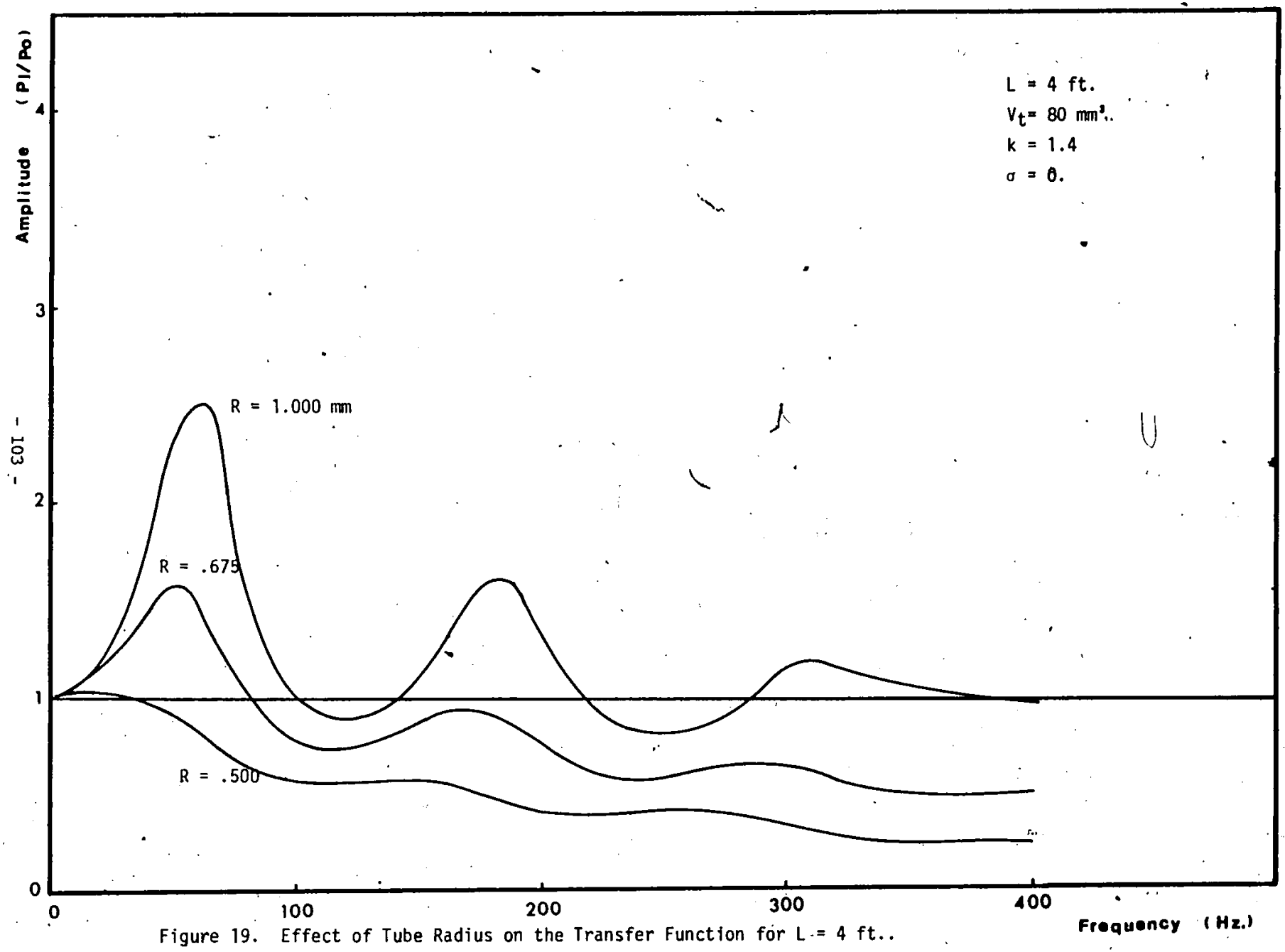

Figure 19. Effect of Tube Radius on the Transfer Function for L = 4 ft..

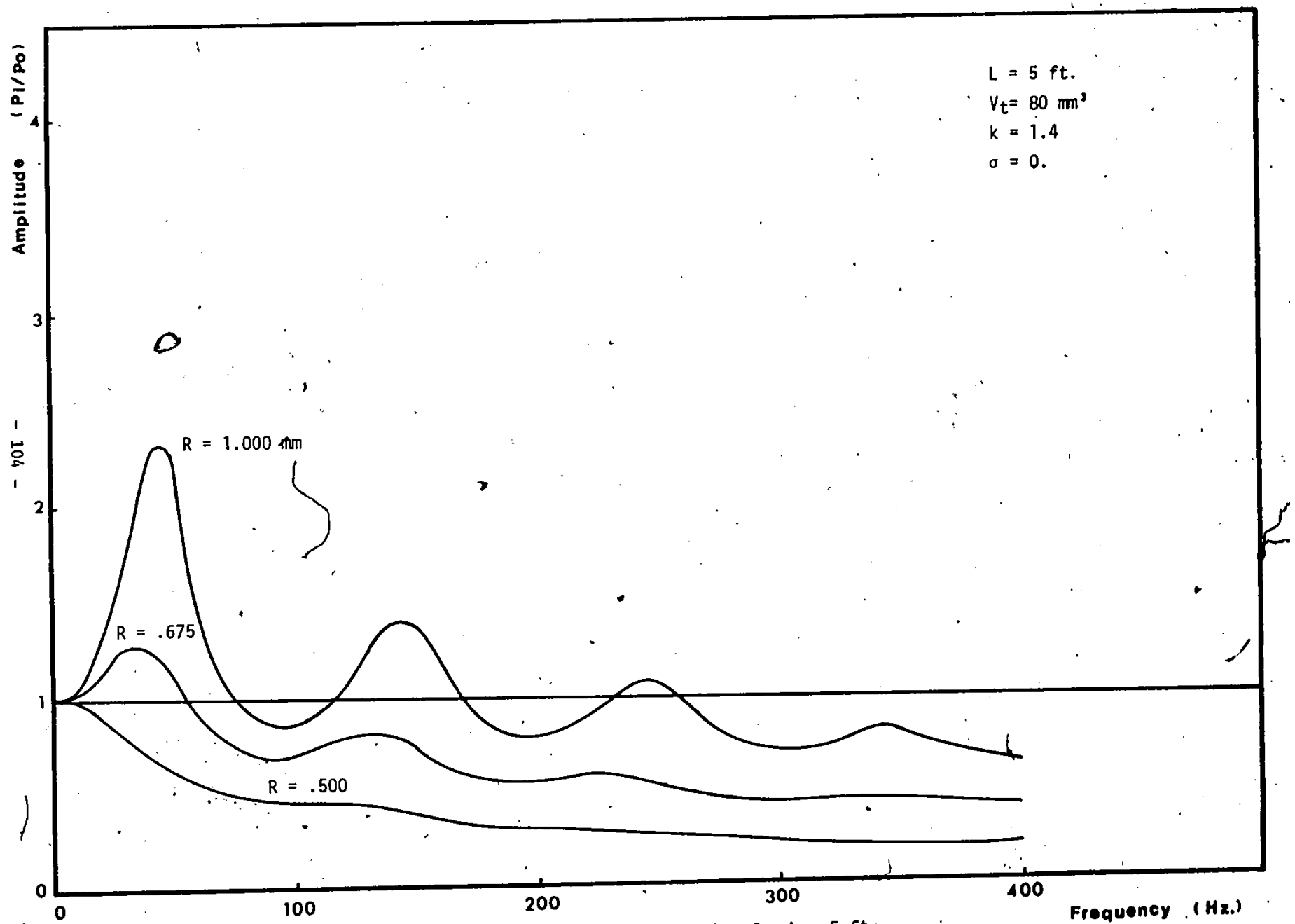

Figure 20. Effect of Tube Radius on the Transfer Function for L = 5 ft..

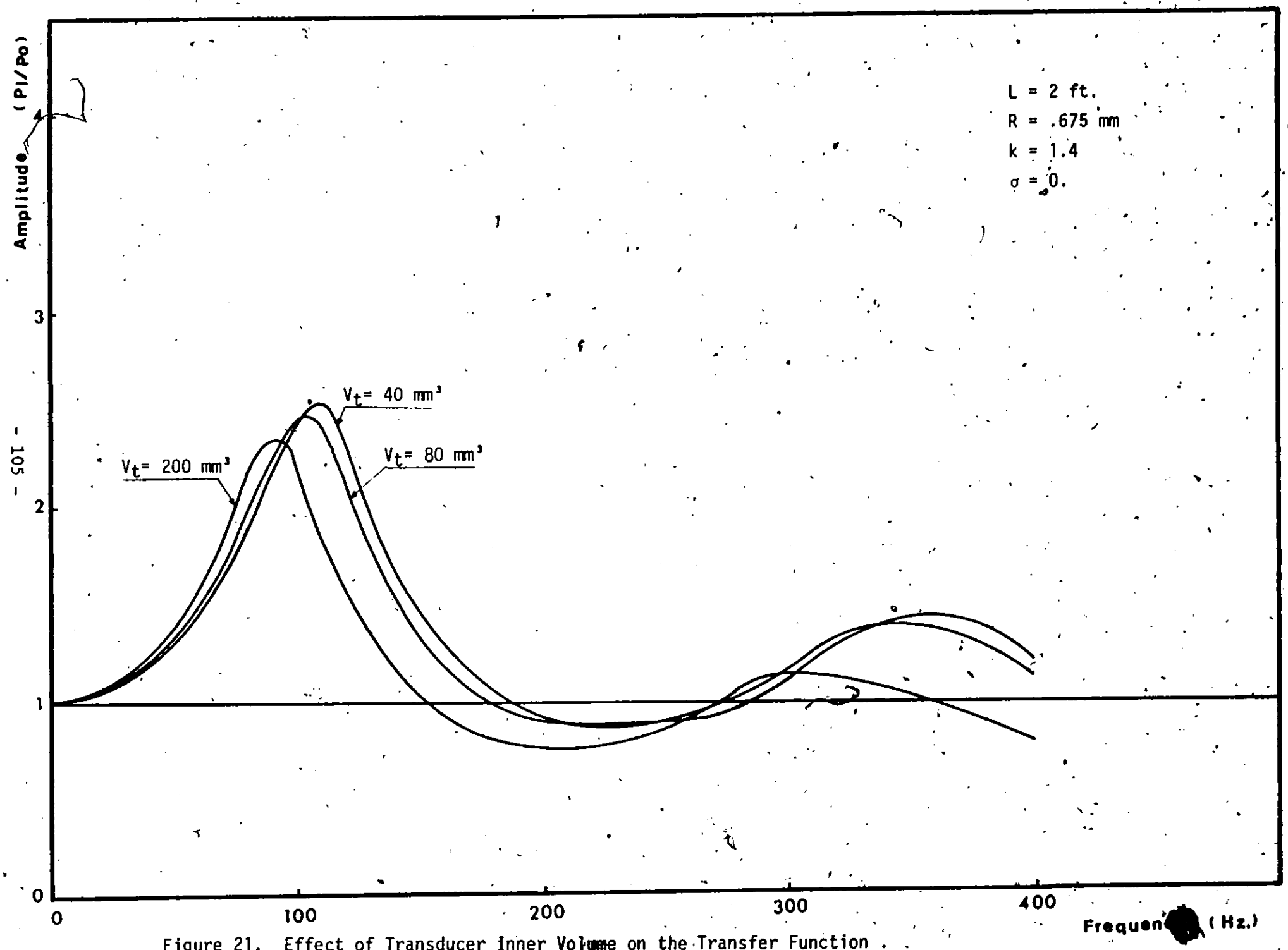

Figure 21. Effect of Transducer Inner Volume on the Transfer Function .

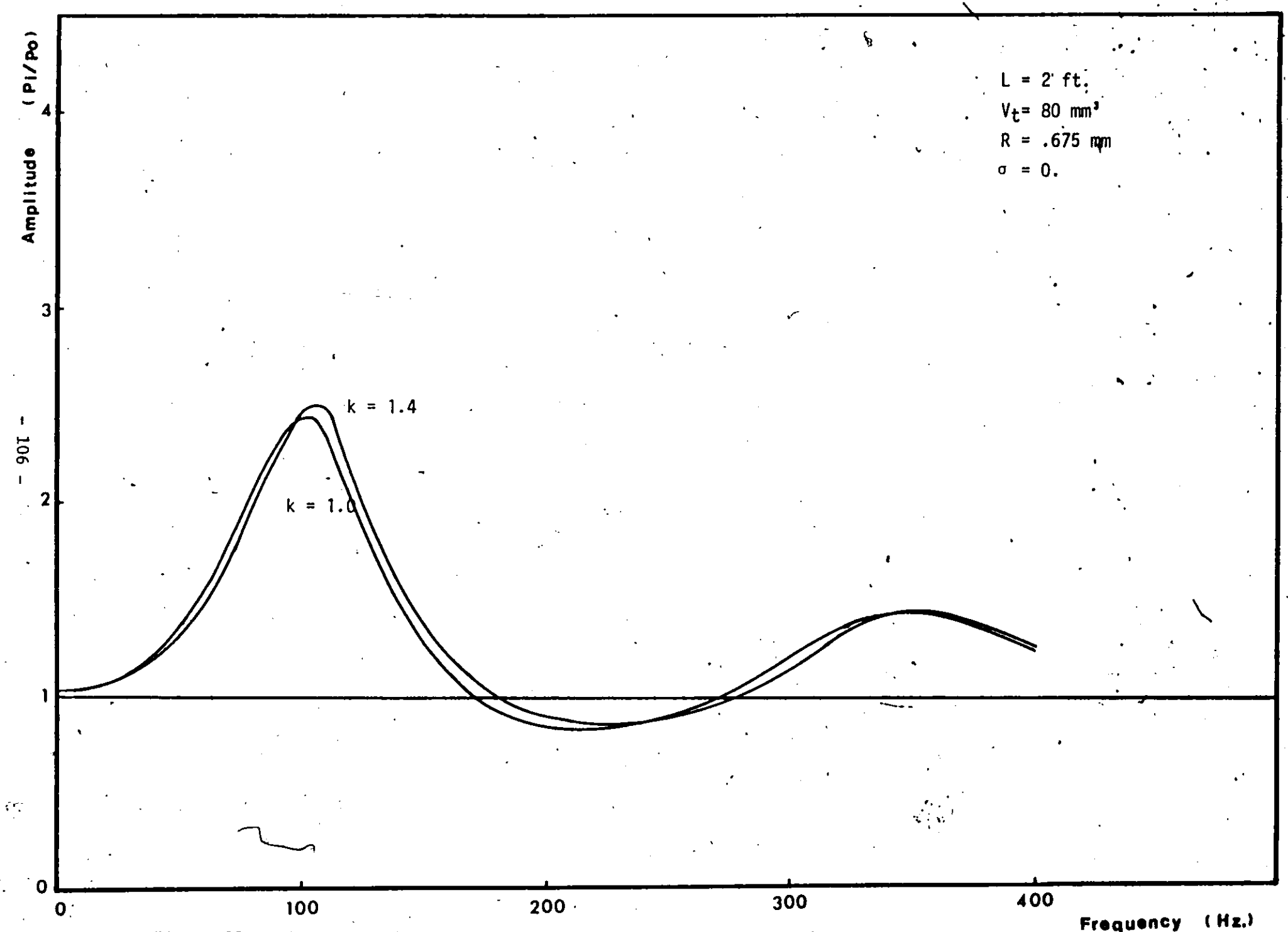

Figure 22. Effect of Polytropic Constant k on the Transfer Function.

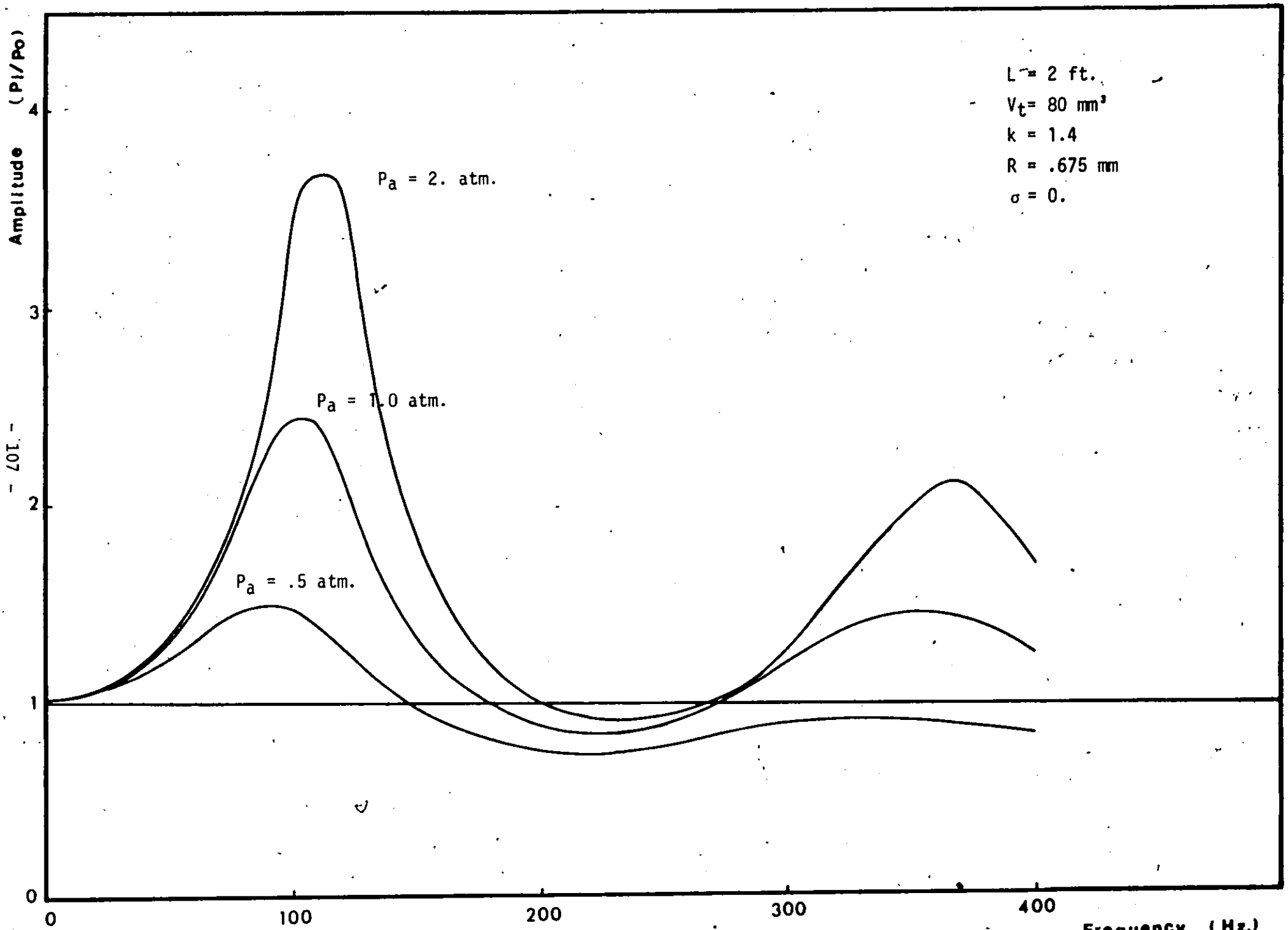

Figure 23. Effect of Mean Static Pressure on the Transfer Function.

Appendix C

FIGURES FOR PART II

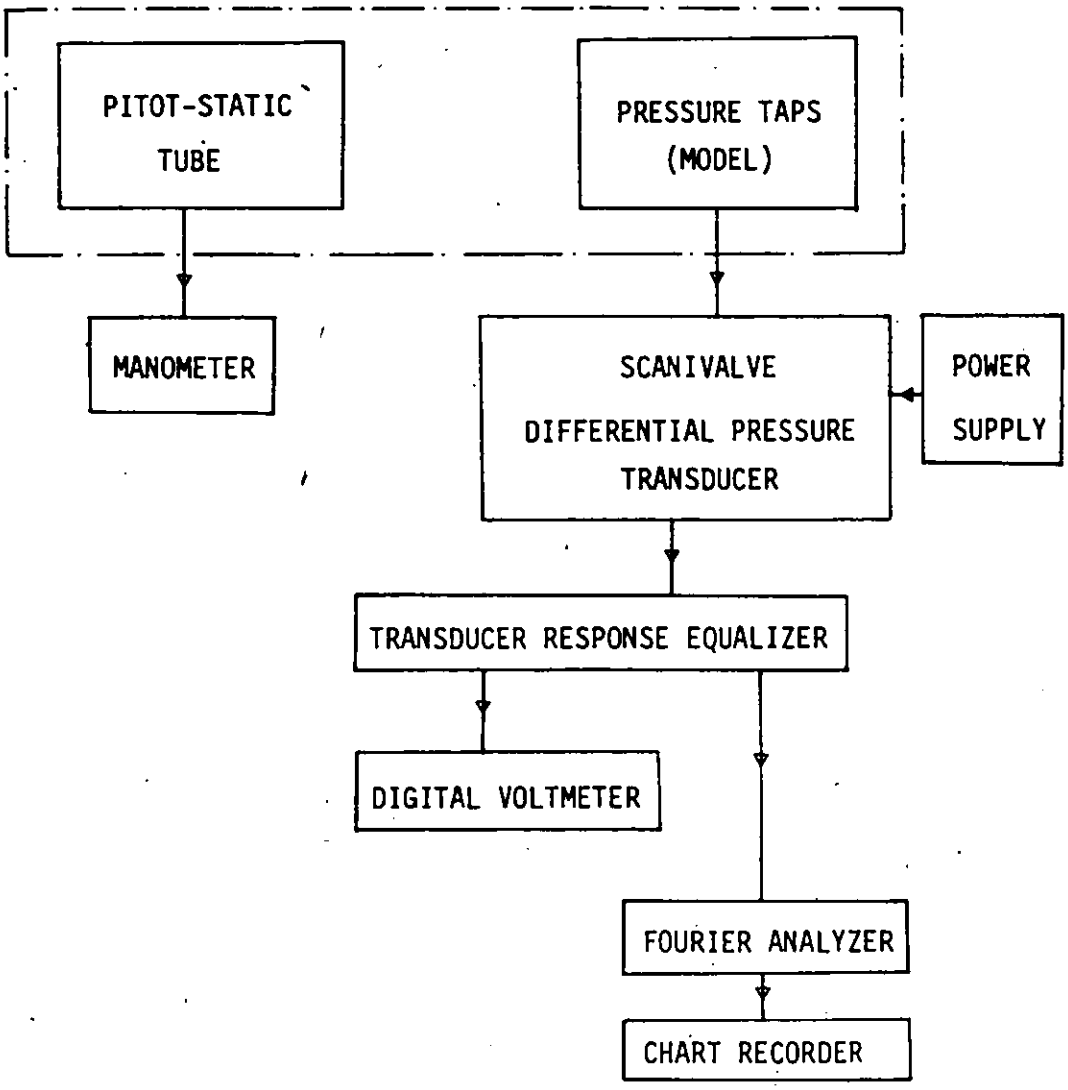

Figure 30. Block Diagram of Instruments Arrangement.

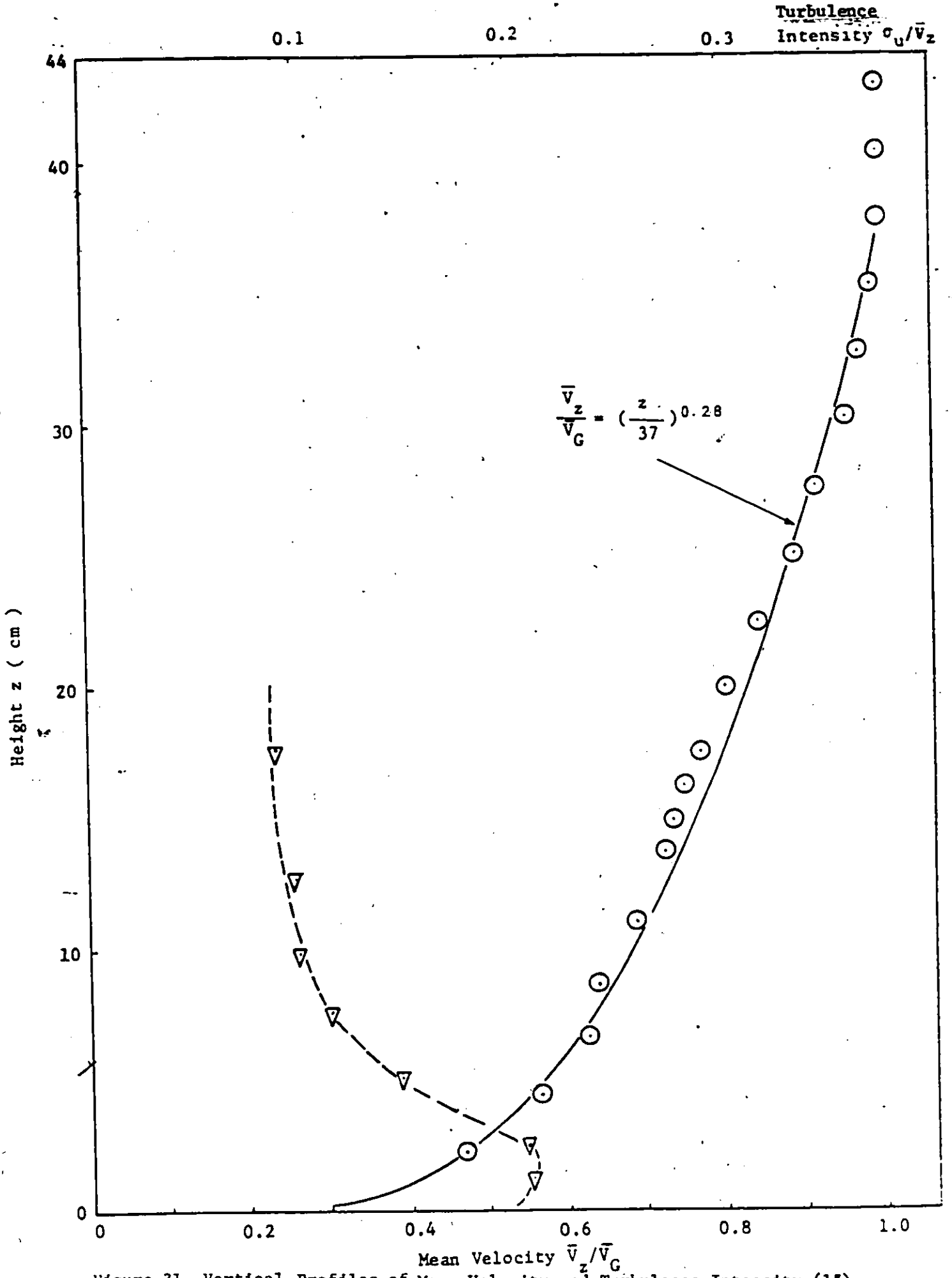

Figure 31. Vertical Profiles of Mean Velocity and Turbulence Intensity (15).

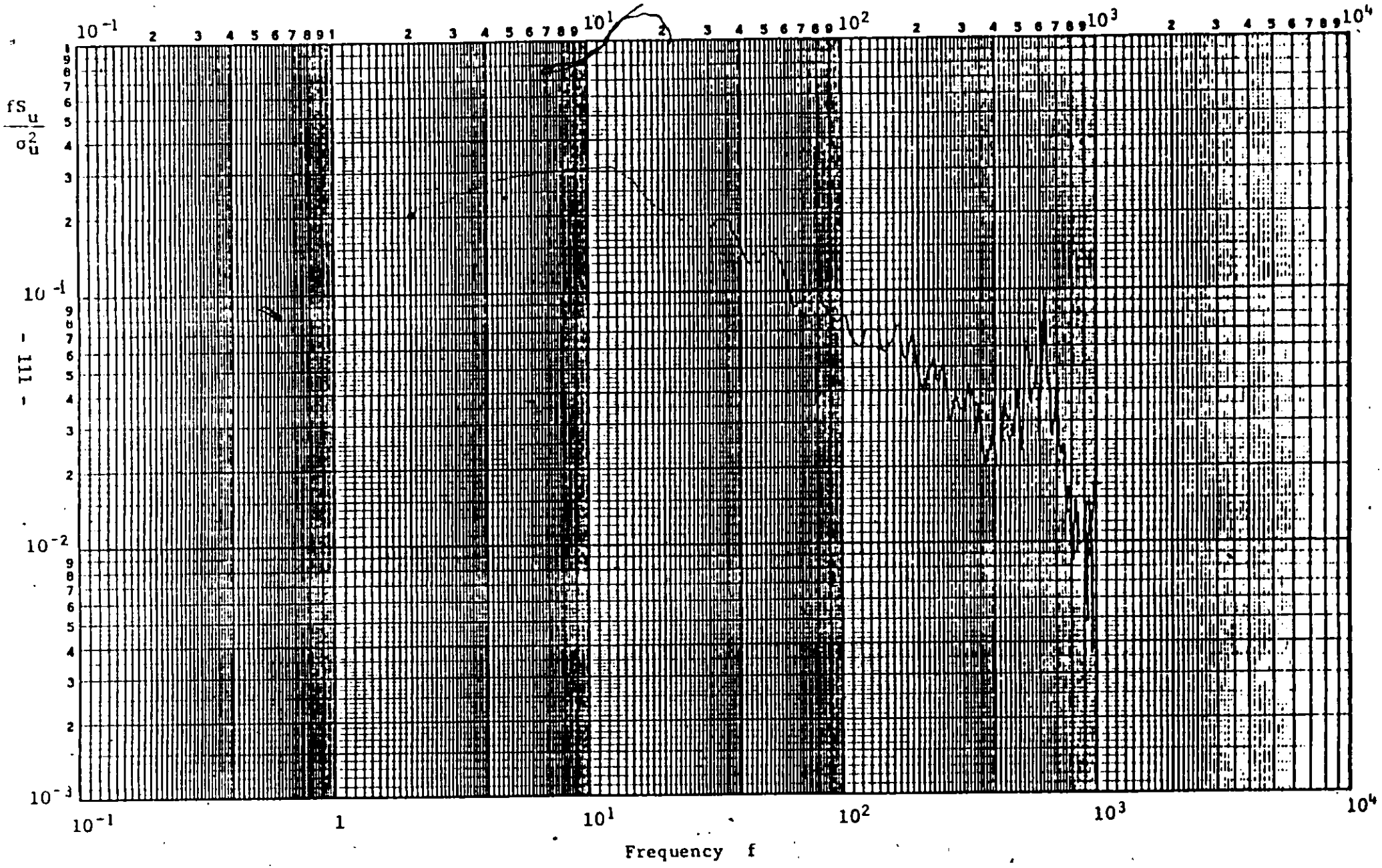

Figure 32. Measured Longitudinal Velocity Spectrum at the Top of the Model Building, (15).

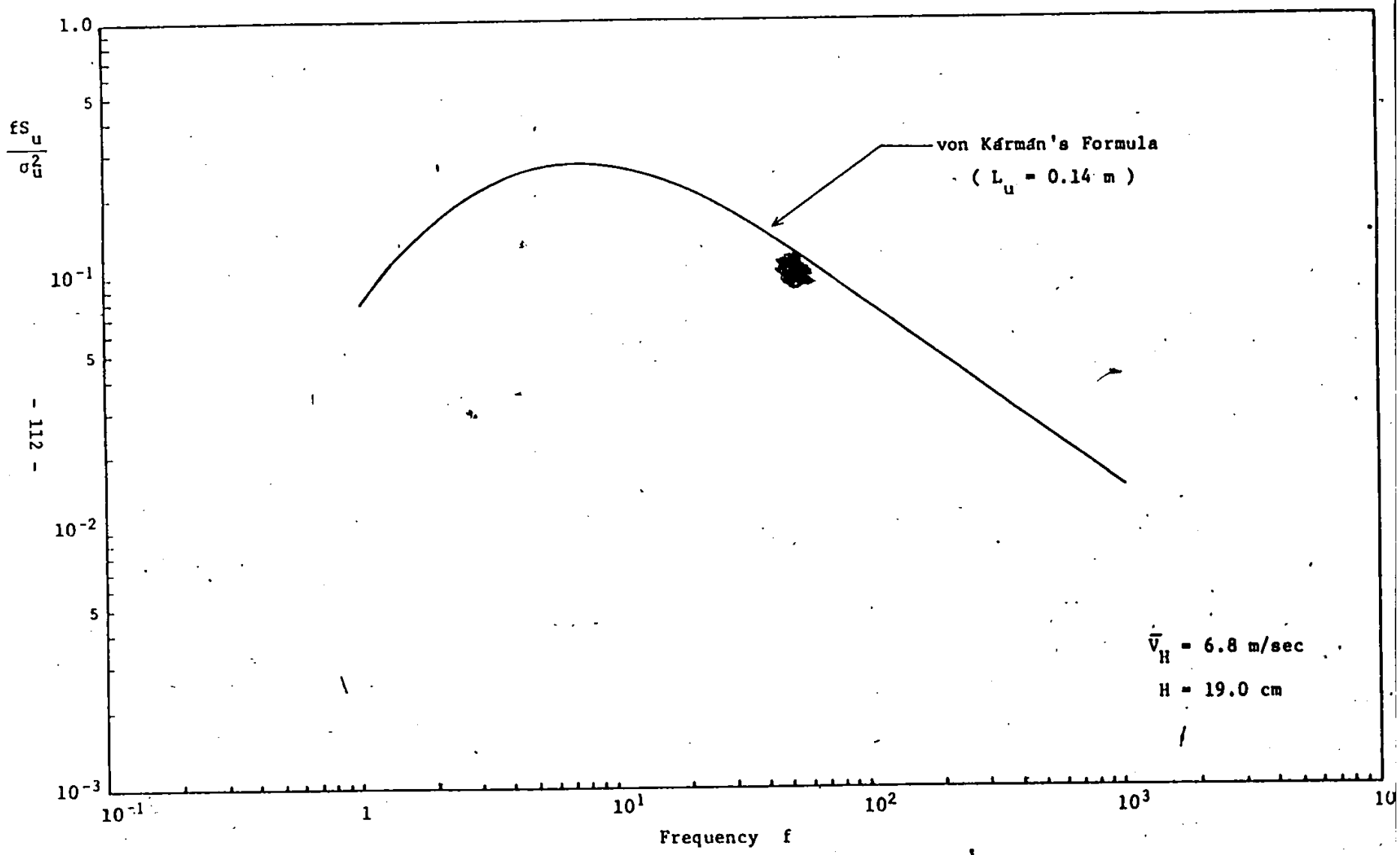

Figure 39. Von Karman's Equation for Velocity Spectrum Based on the Wind Tunnel Measurement, (15).

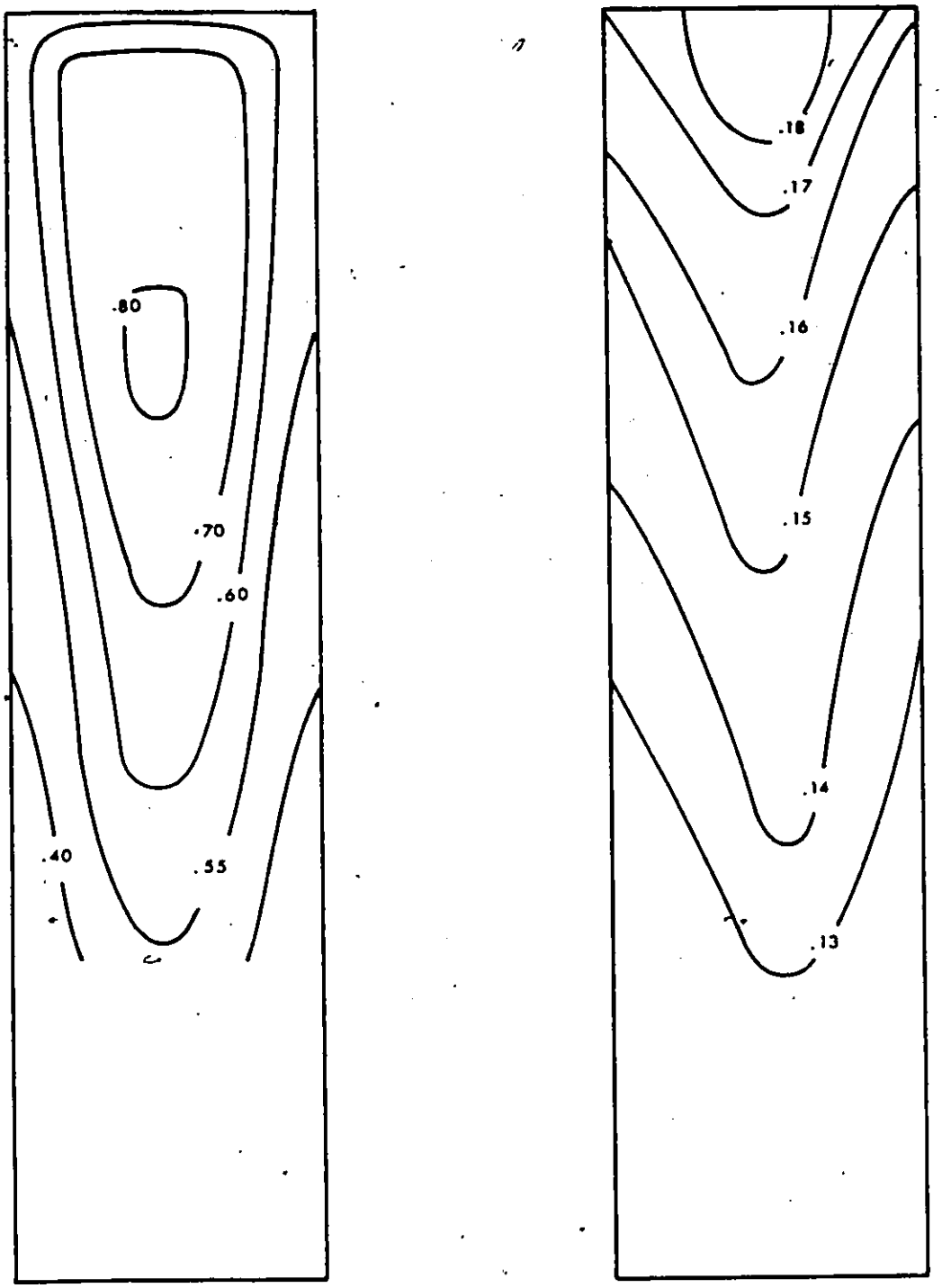

Figure 34. Pressure Distribution on Face 1, $\beta = 0^{\circ}$.

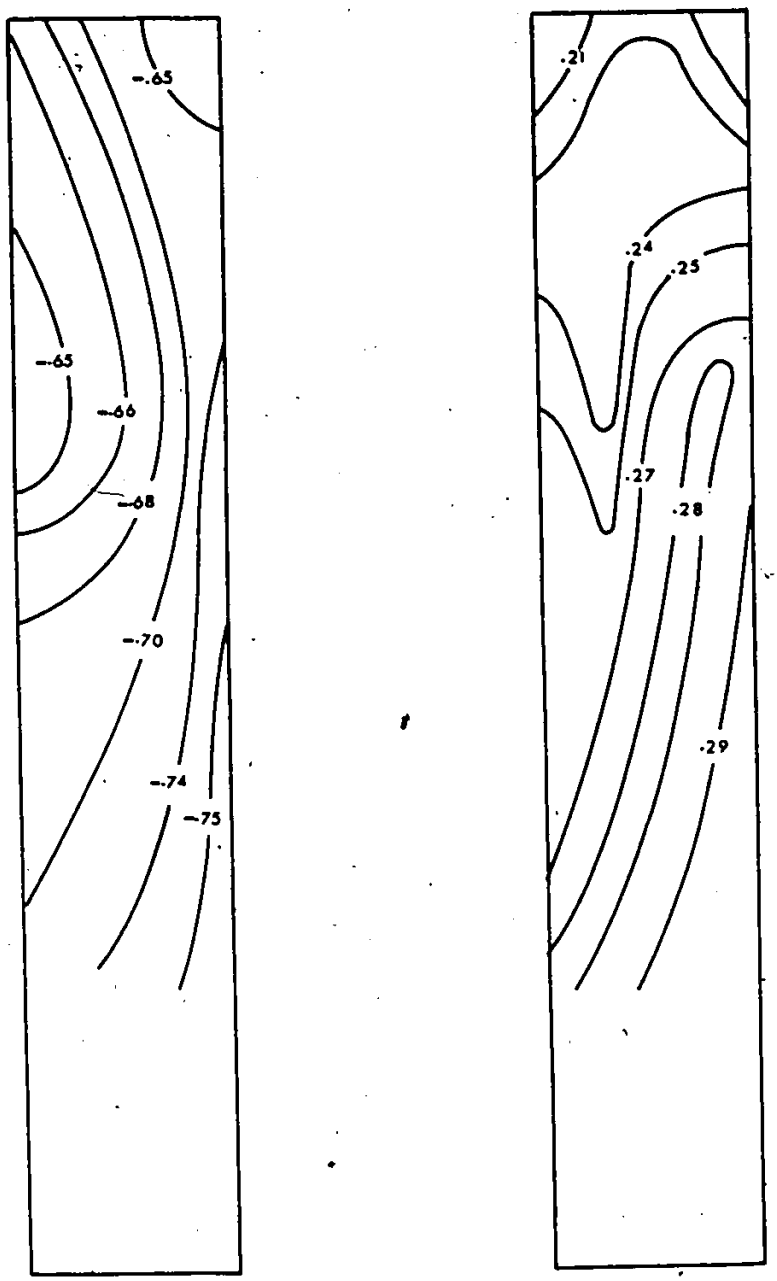

Figure 35. Pressure Distribution on Face 2, $\beta = 0^{\circ}$.

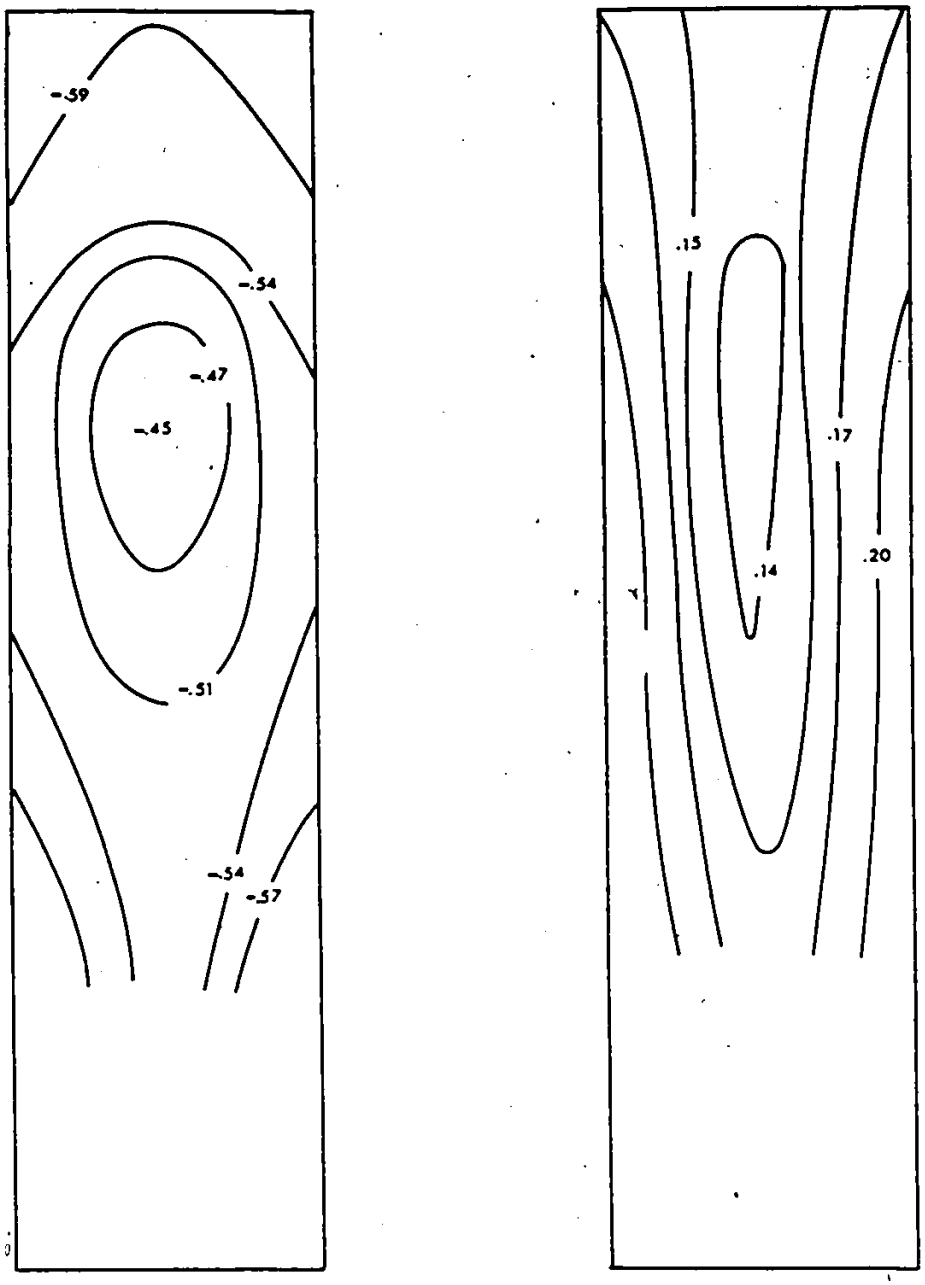

Figure 36. Pressure Distribution on Face 3, $\beta = 0^{\circ}$.

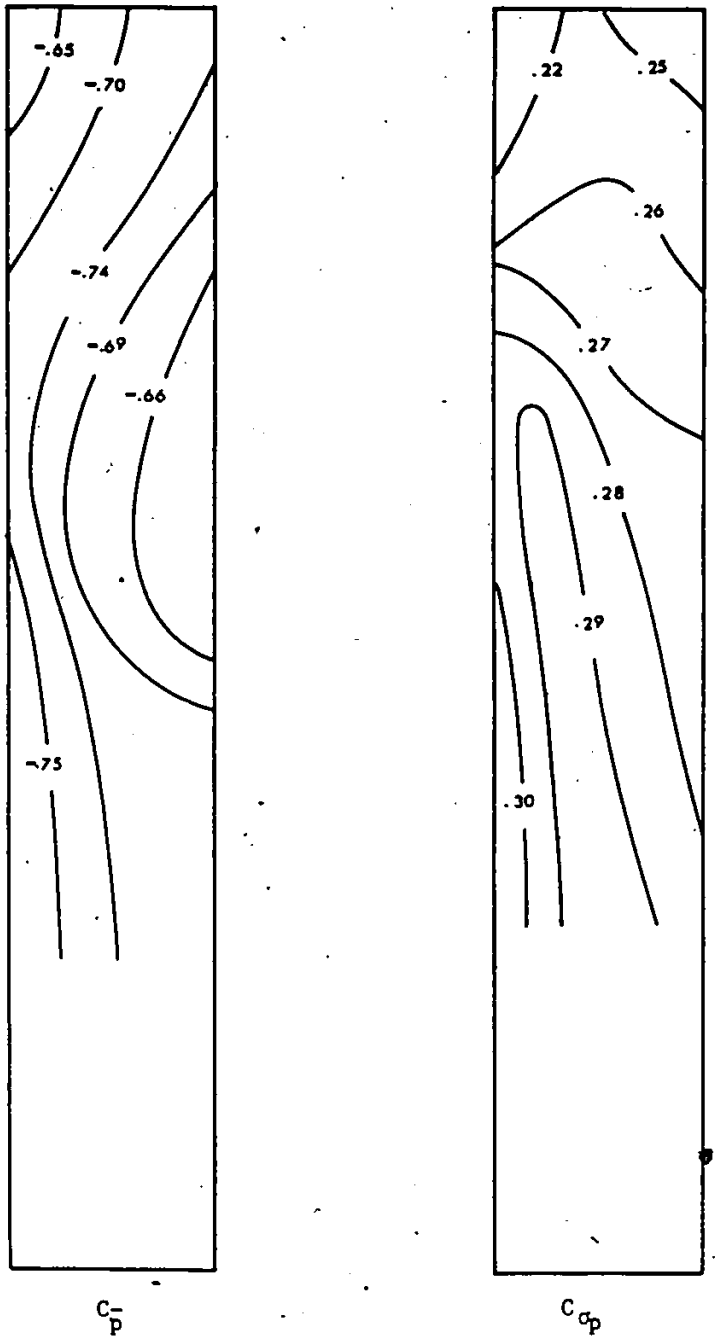

Figure 37. Pressure Distribution on Face 4, $\beta = 0^{\circ}$.

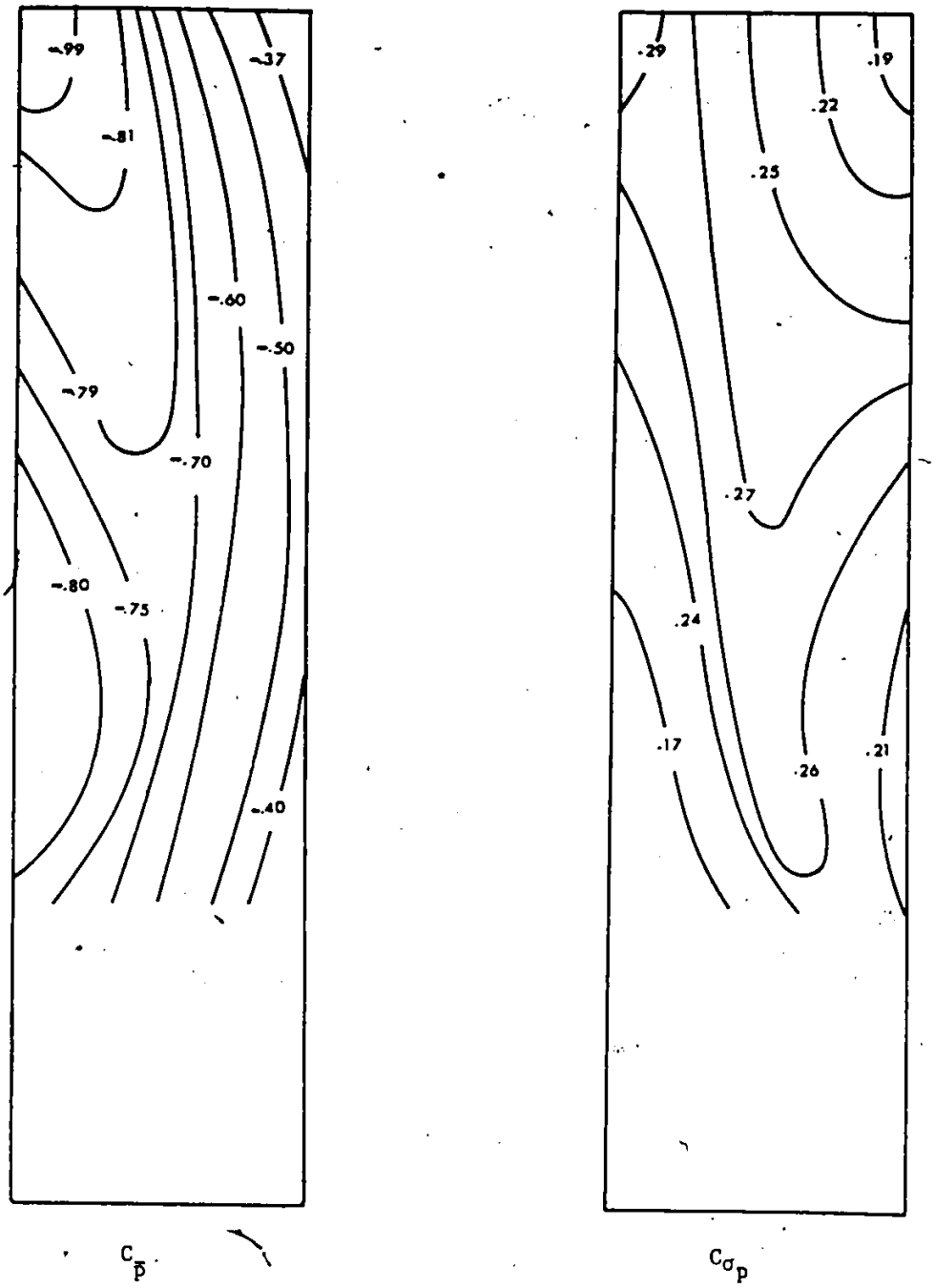

Figure 38. Pressure Distribution on Face 1, $\beta = 90^{\circ}$.

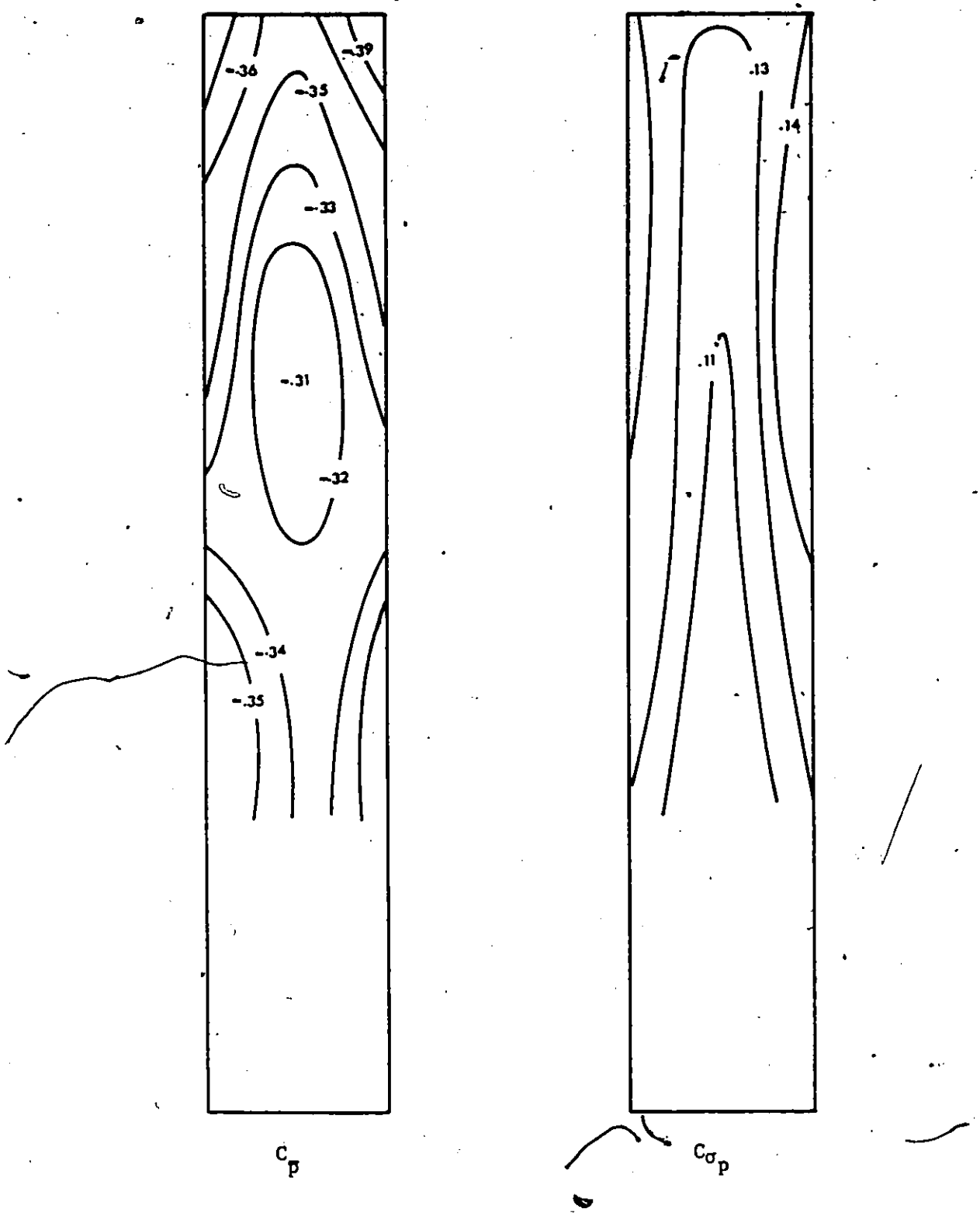

Figure 39. Pressure Distribution on Face 2, $\beta = 90^\circ$.

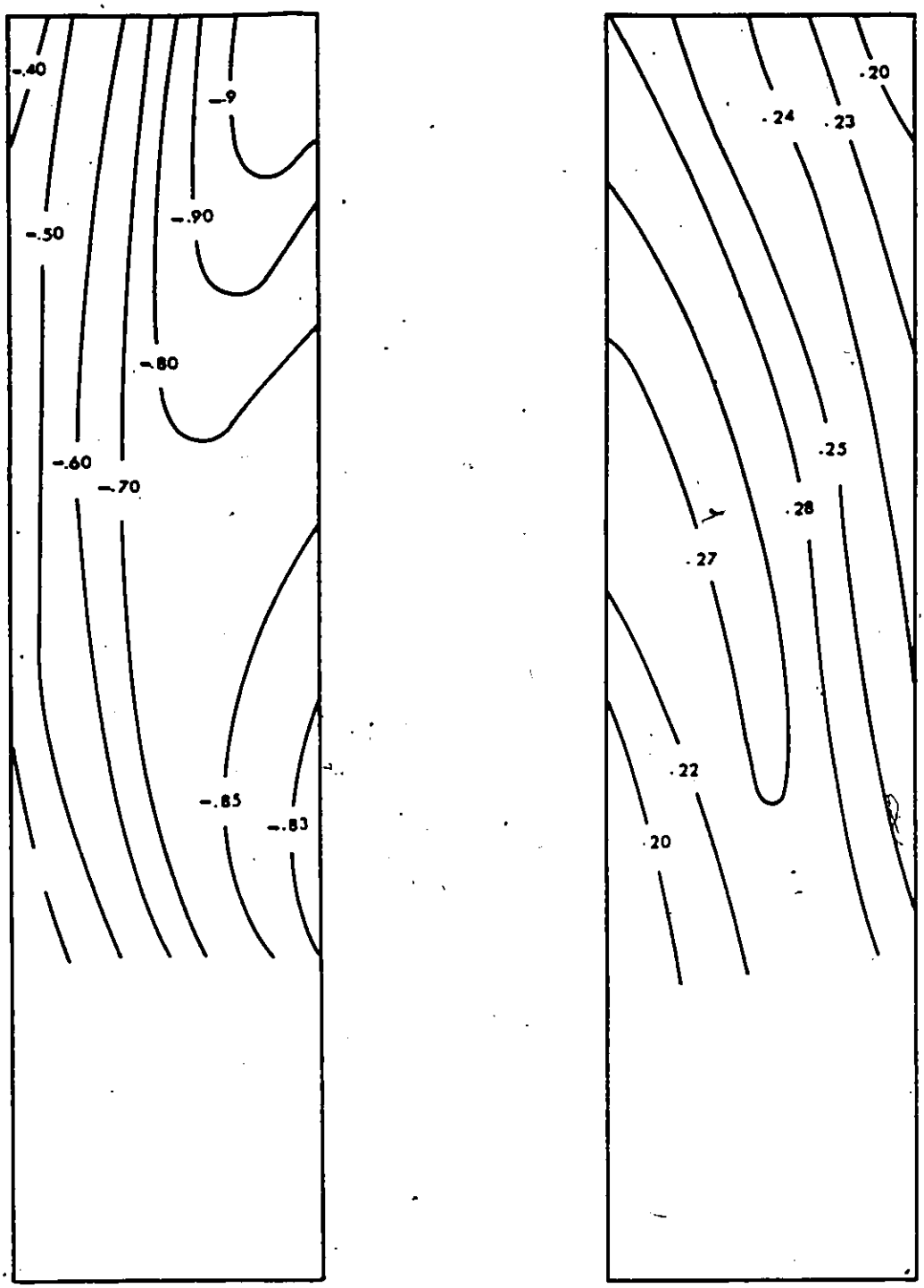

Figure 40. Pressure Distribution on Face 3, $\beta = 90^{\circ}$.

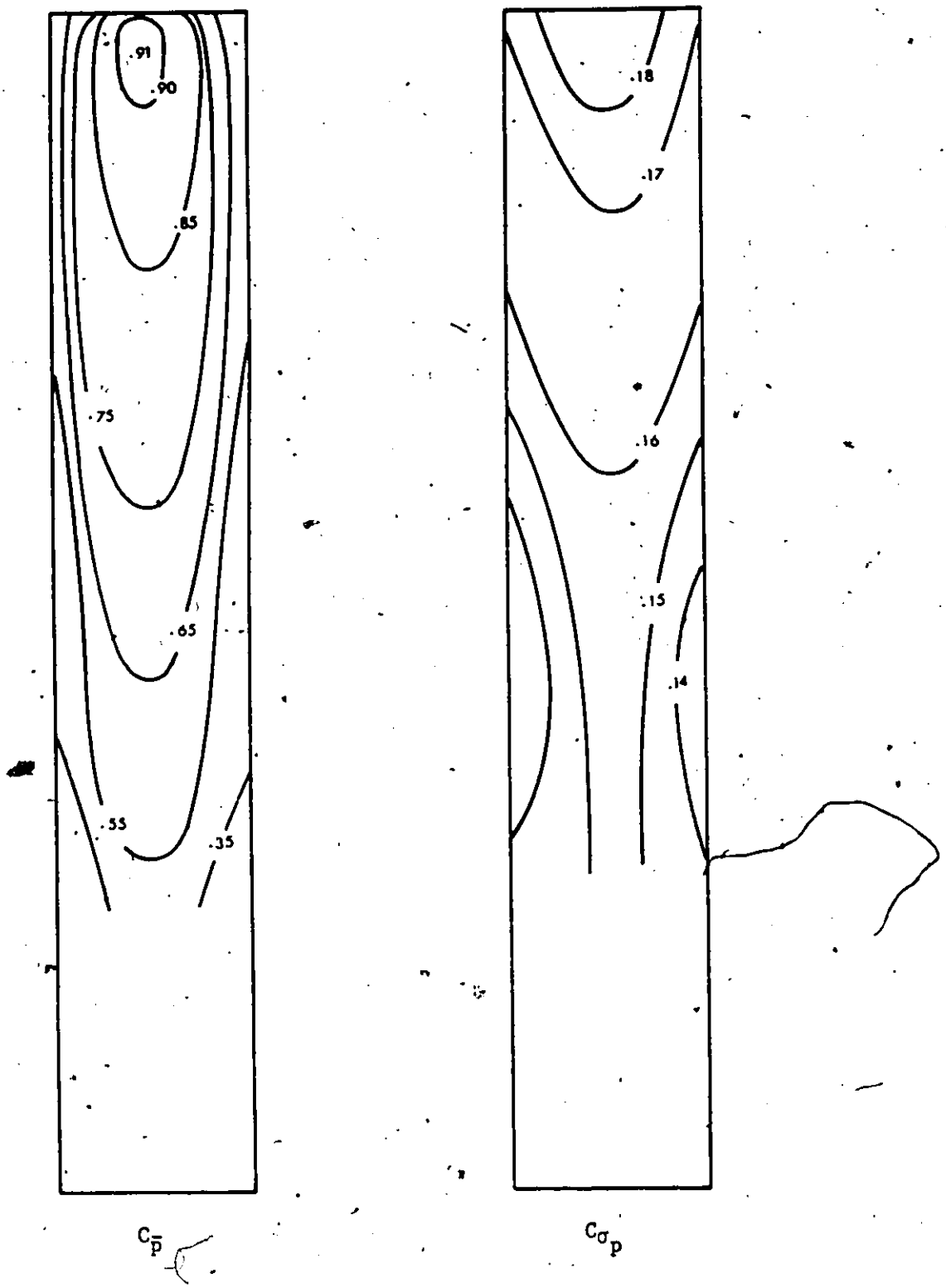

Figure 41. Pressure Distribution on Face 4, $\beta = 90^{\circ}$.

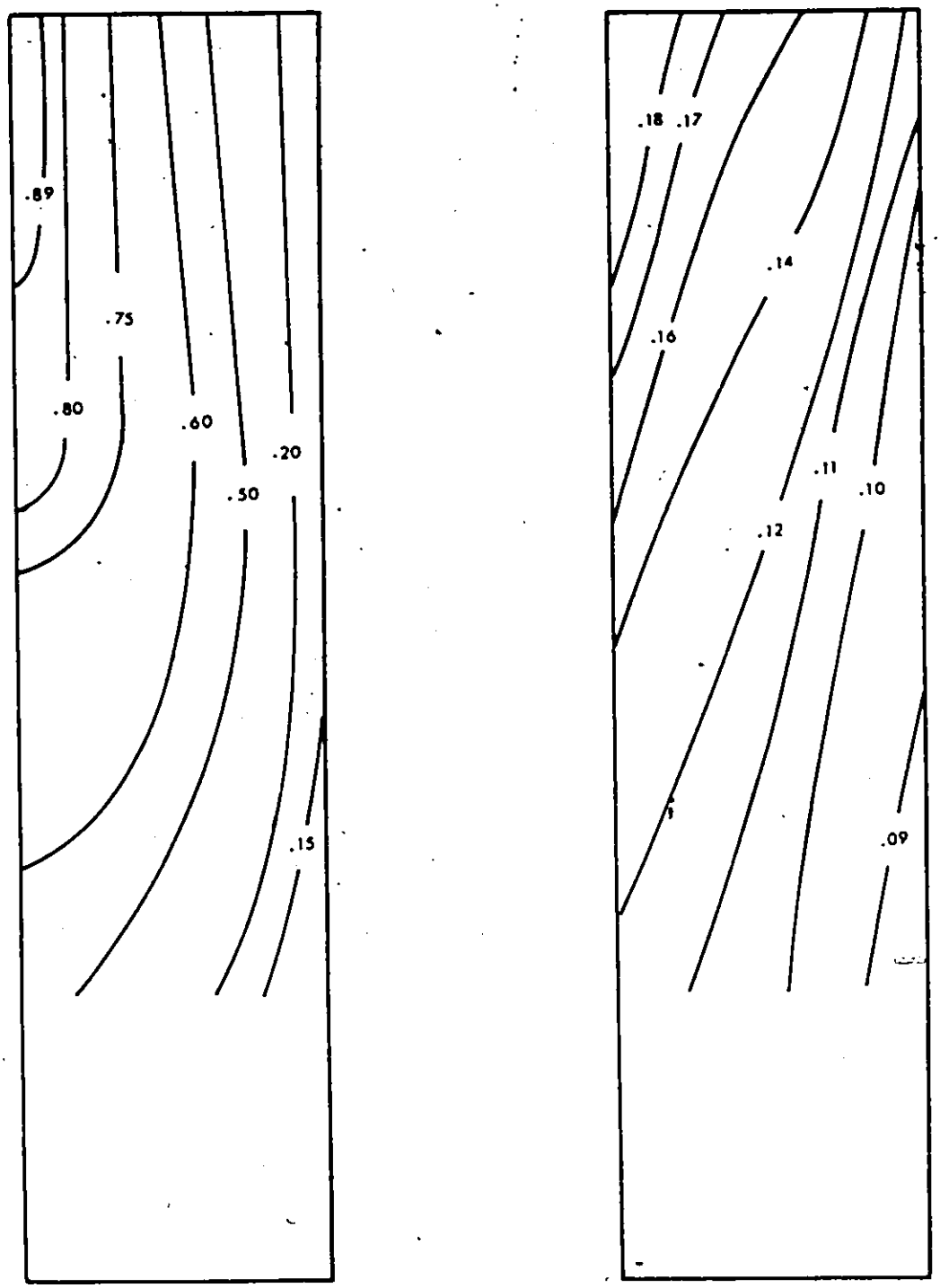

Figure 42. Pressure Distribution on Face 1, $\beta=30^{\circ}$.

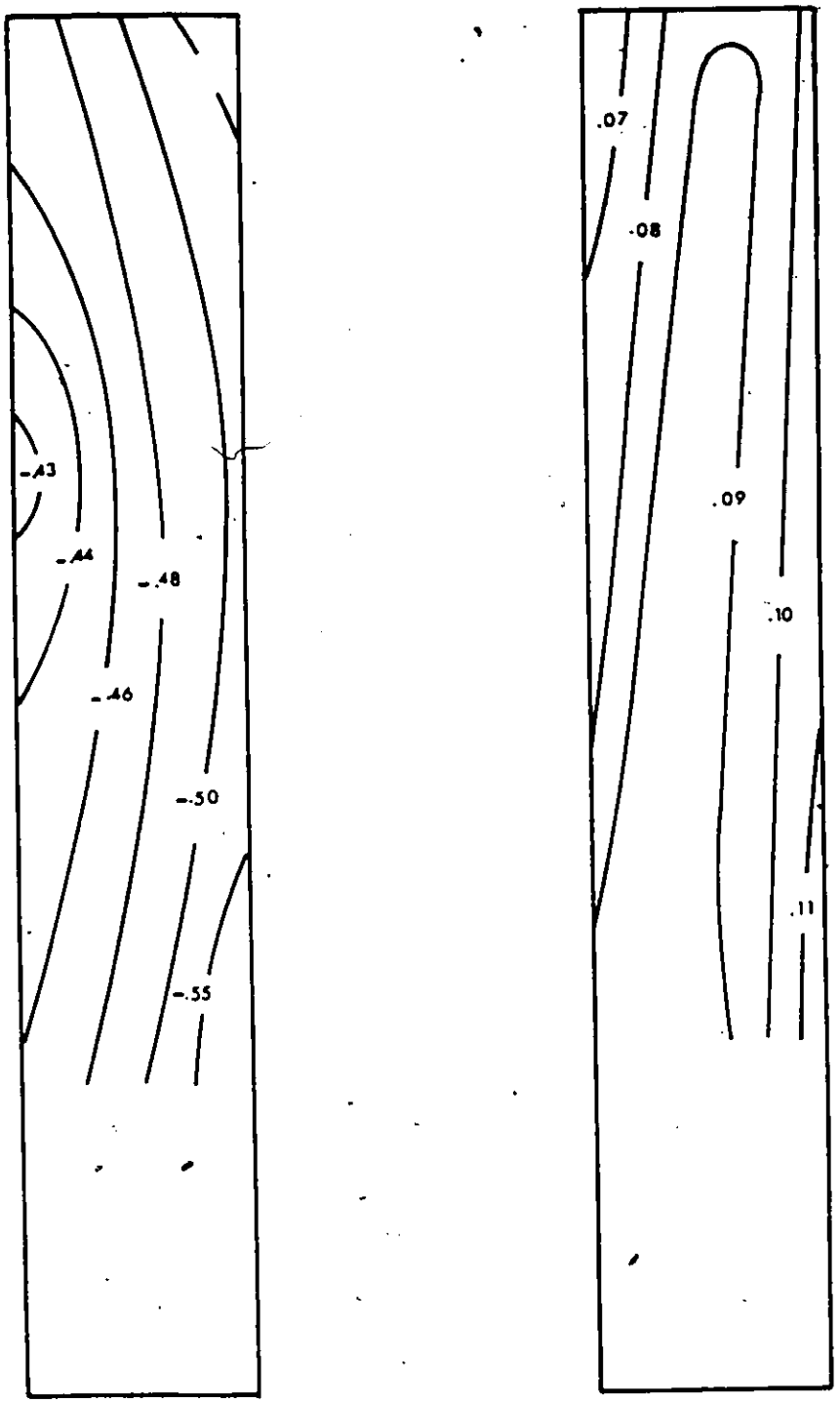

Figure 43. Pressure Distribution on Face 2, $\beta = 30^{\circ}$.

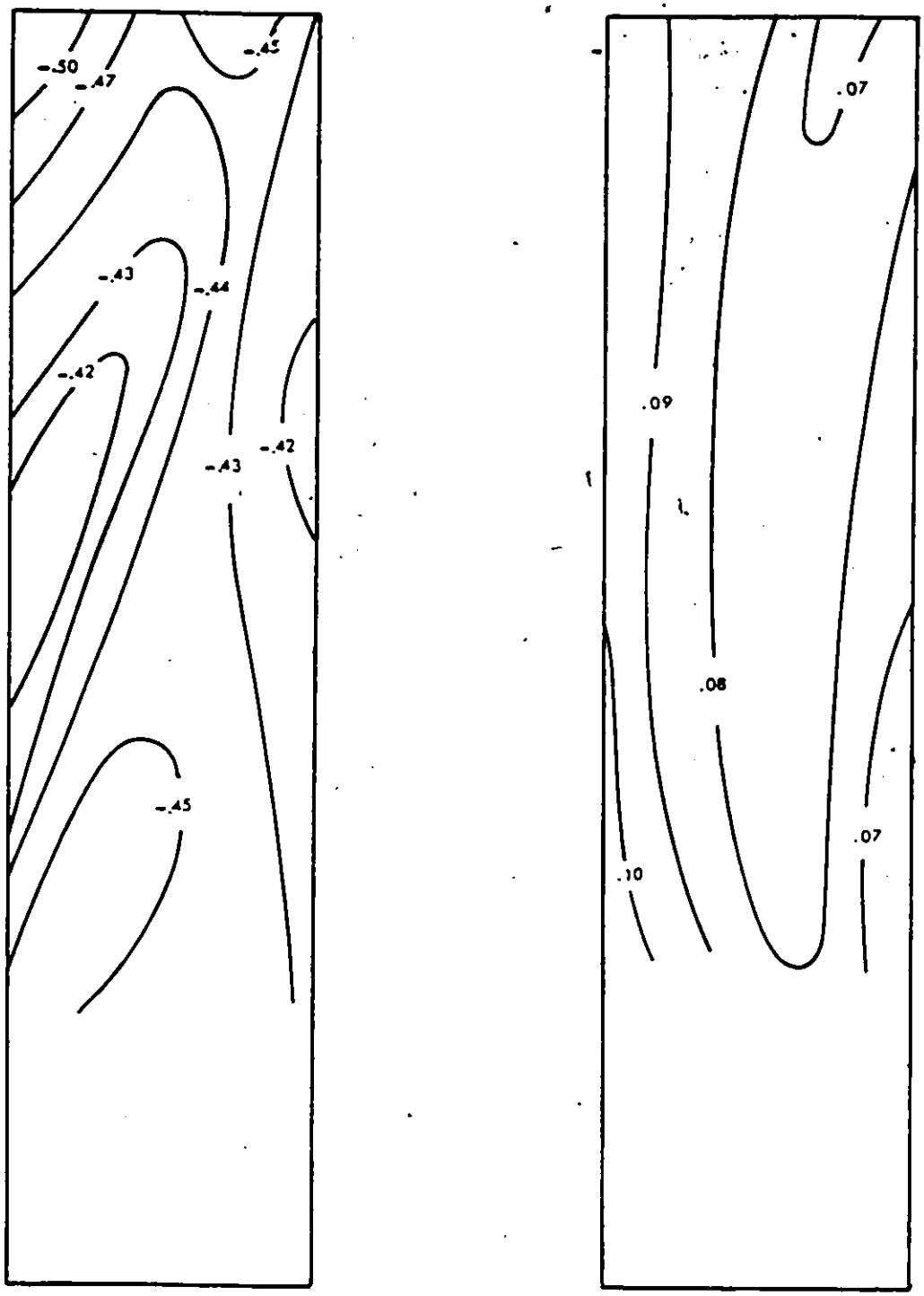

Figure 44. Pressure Distribution on Face 3, $\beta = 30^{\circ}$.

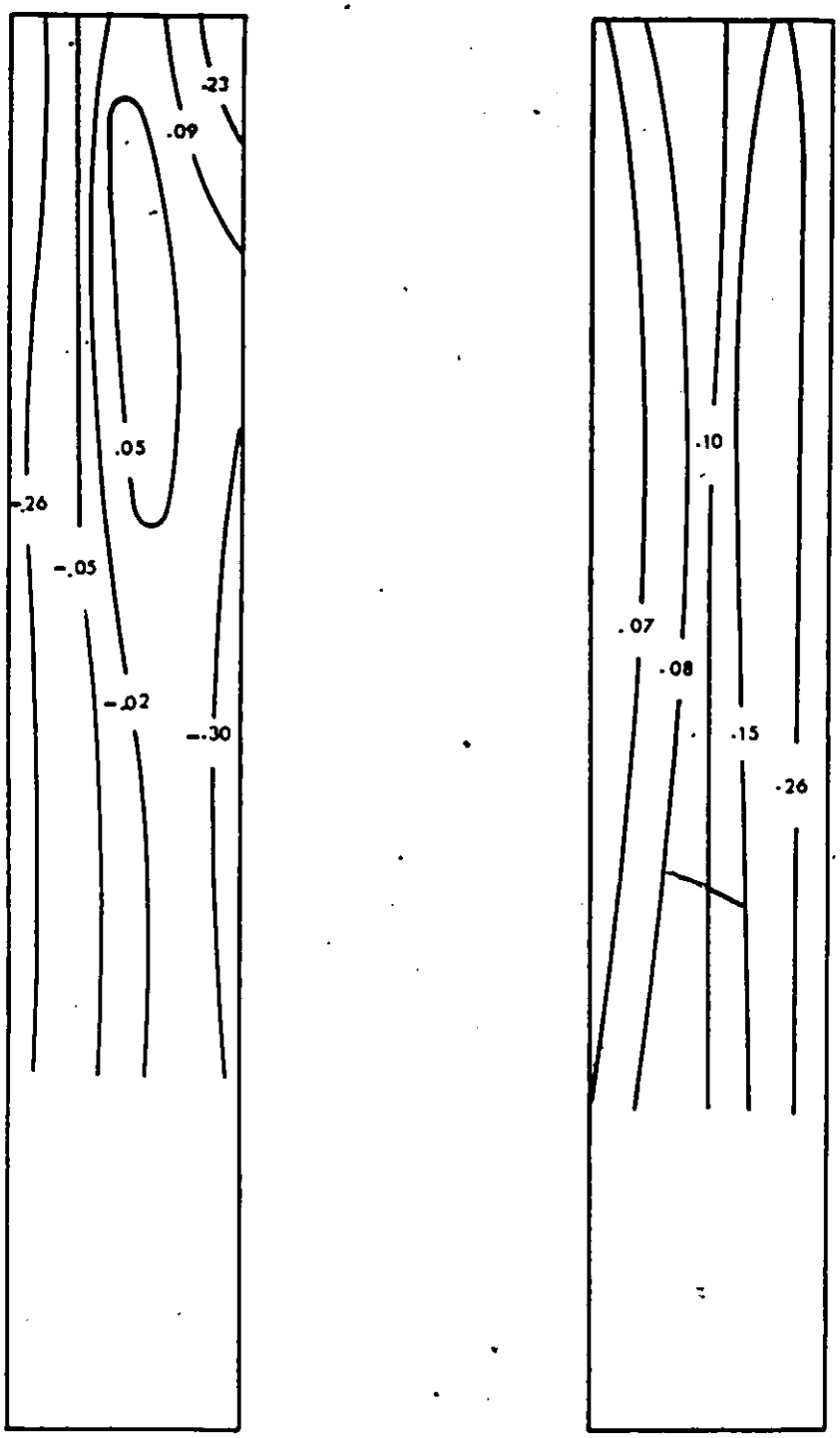

Figure 45. Pressure Distribution on Face 4, $\beta = 30^{\circ}$.

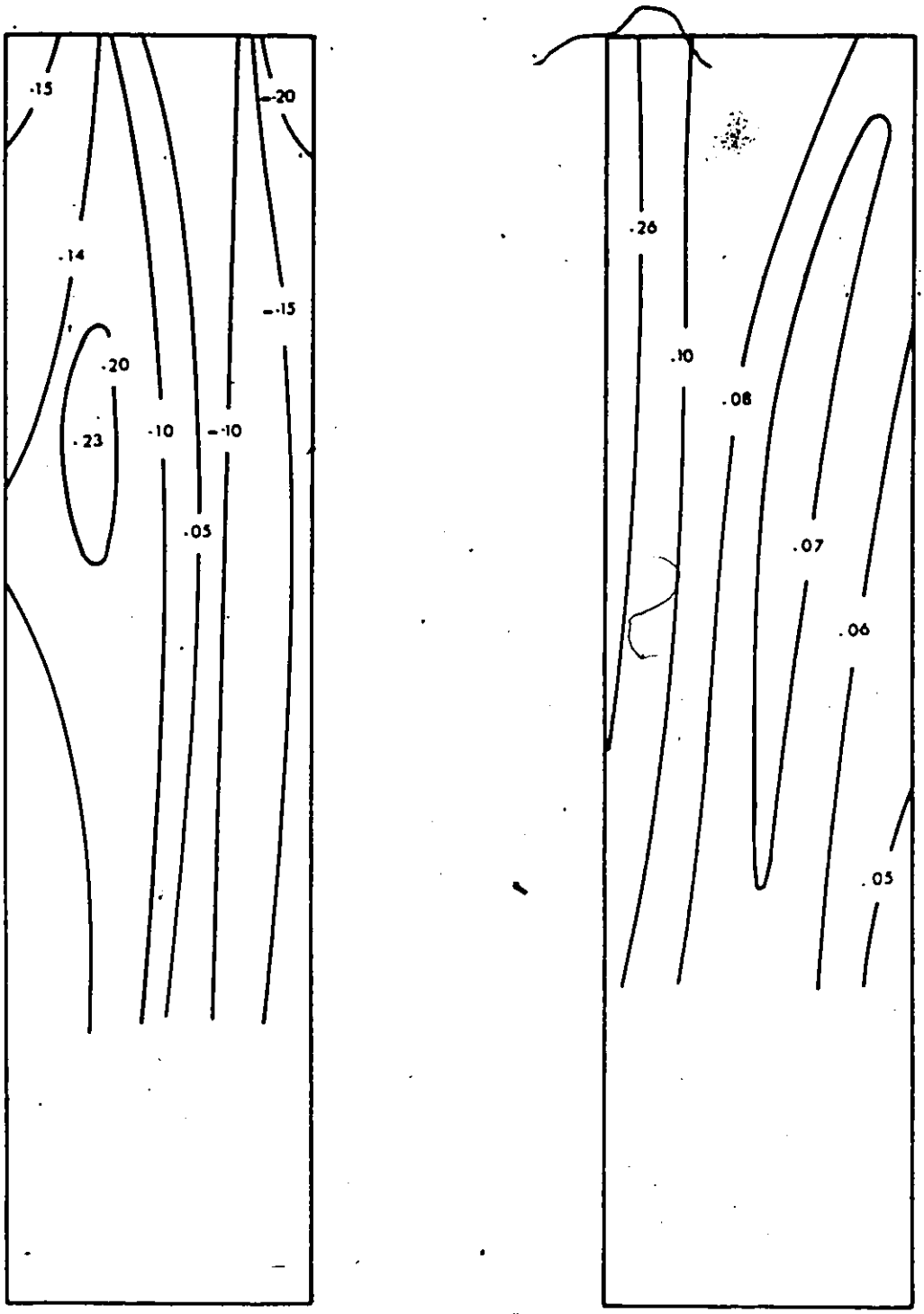

Figure 46. Pressure Distribution on Face 1, $\beta = 60^{\circ}$.

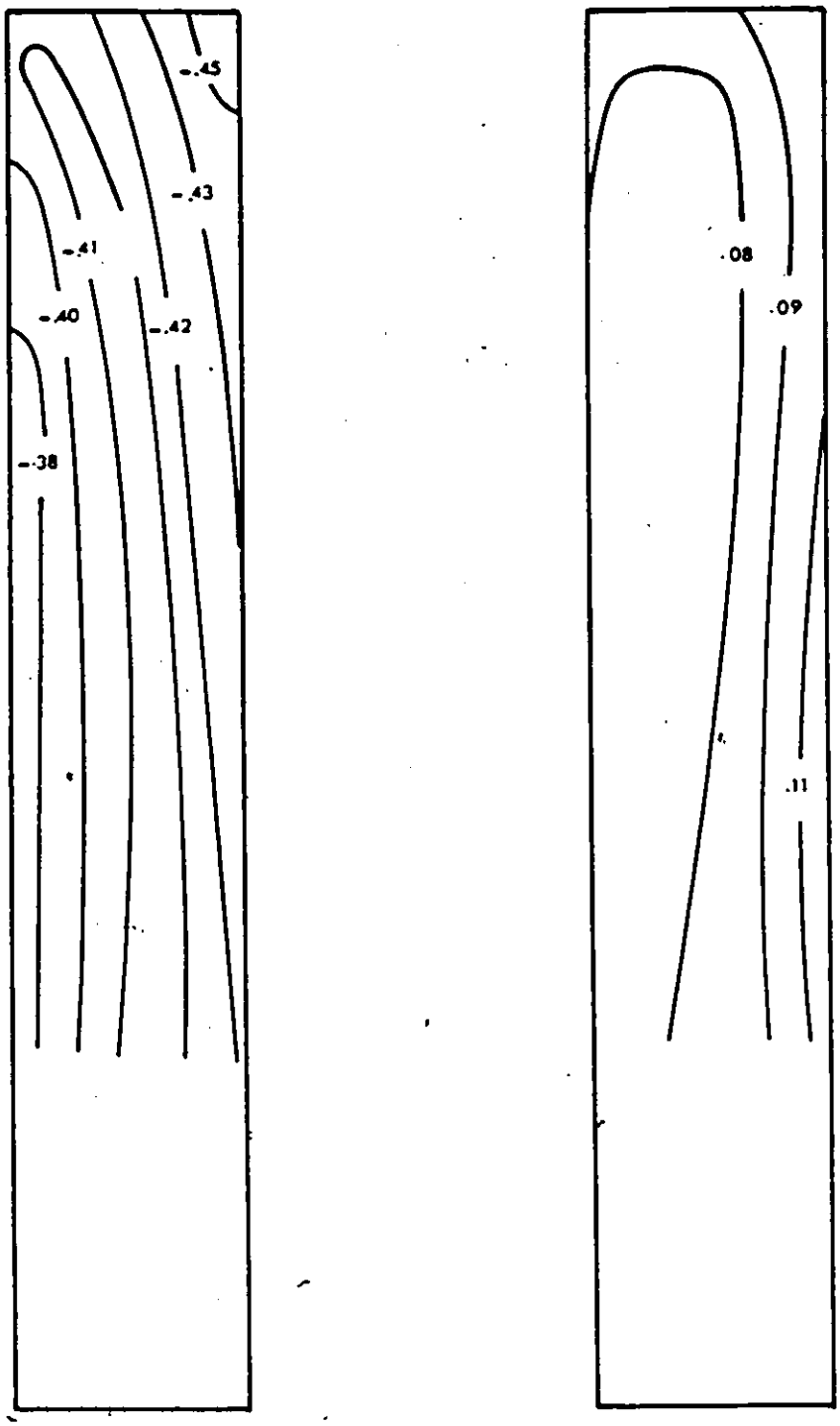

Figure 47. Pressure Distribution on Face 2, $\beta = 60^{\circ}$.

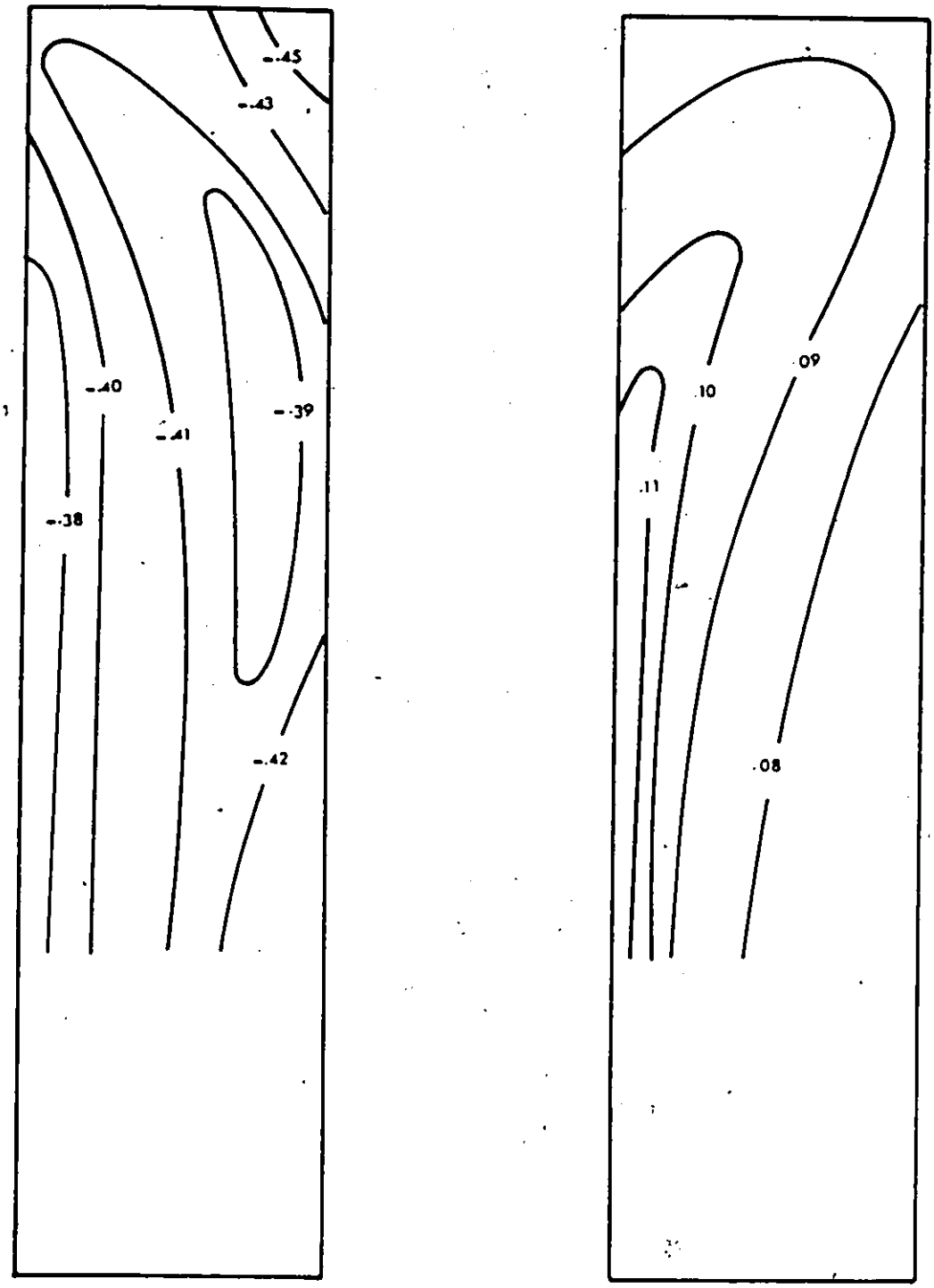

Figure 48. Pressure Distribution on Face 3, $\beta = 60^{\circ}$.

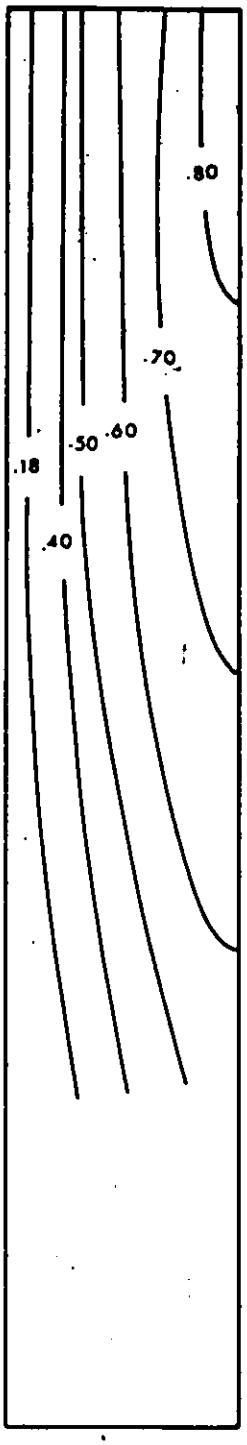

$C_{\bar{p}}$

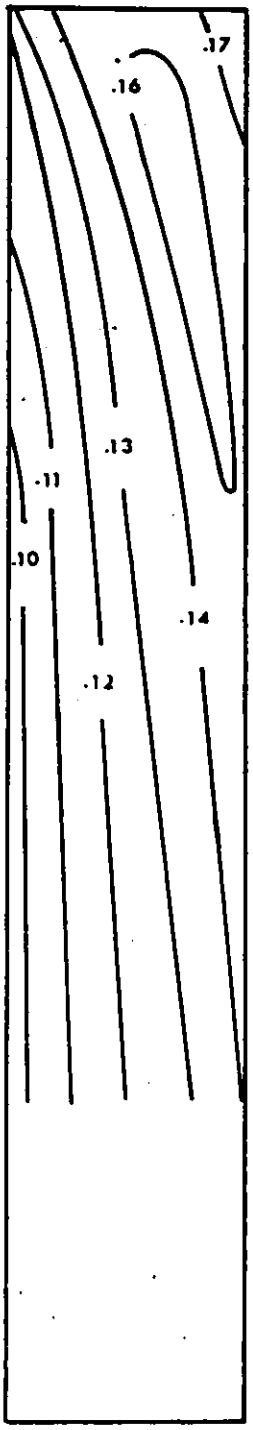

C_{σ_p}

Figure 49. Pressure Distribution on Face 4, $\beta = 60^{\circ}$.

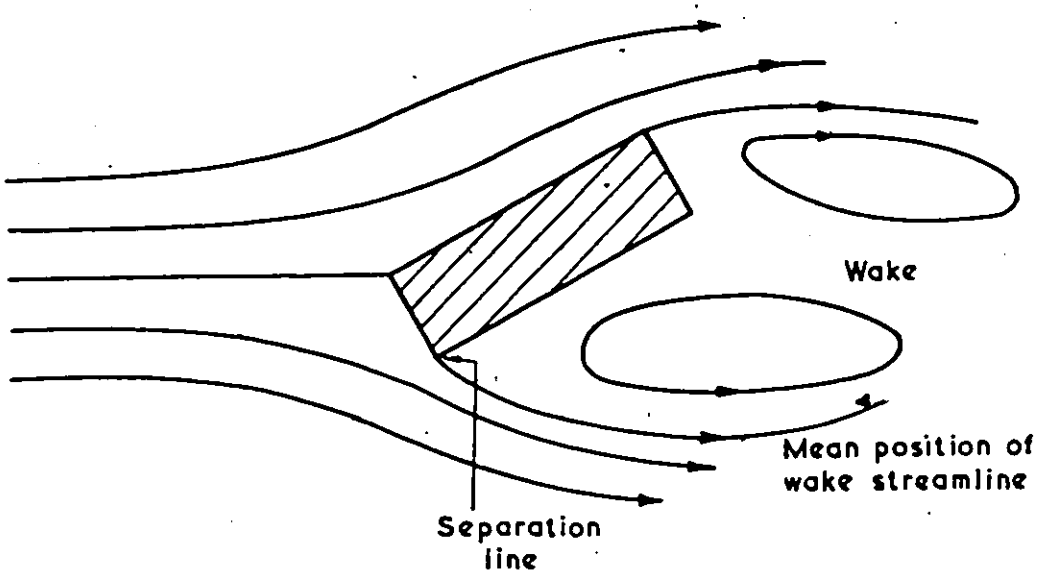

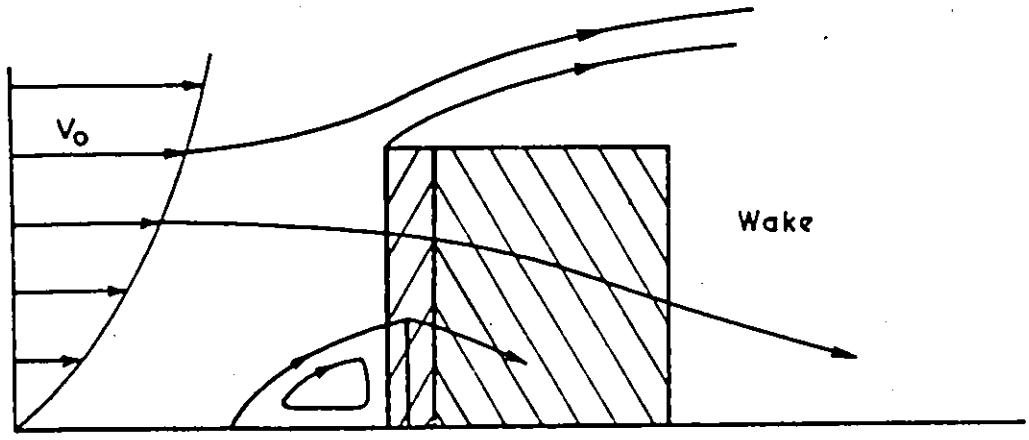

Figure 50. Definition Sketch of Flow over a Building, (Ref. 17).

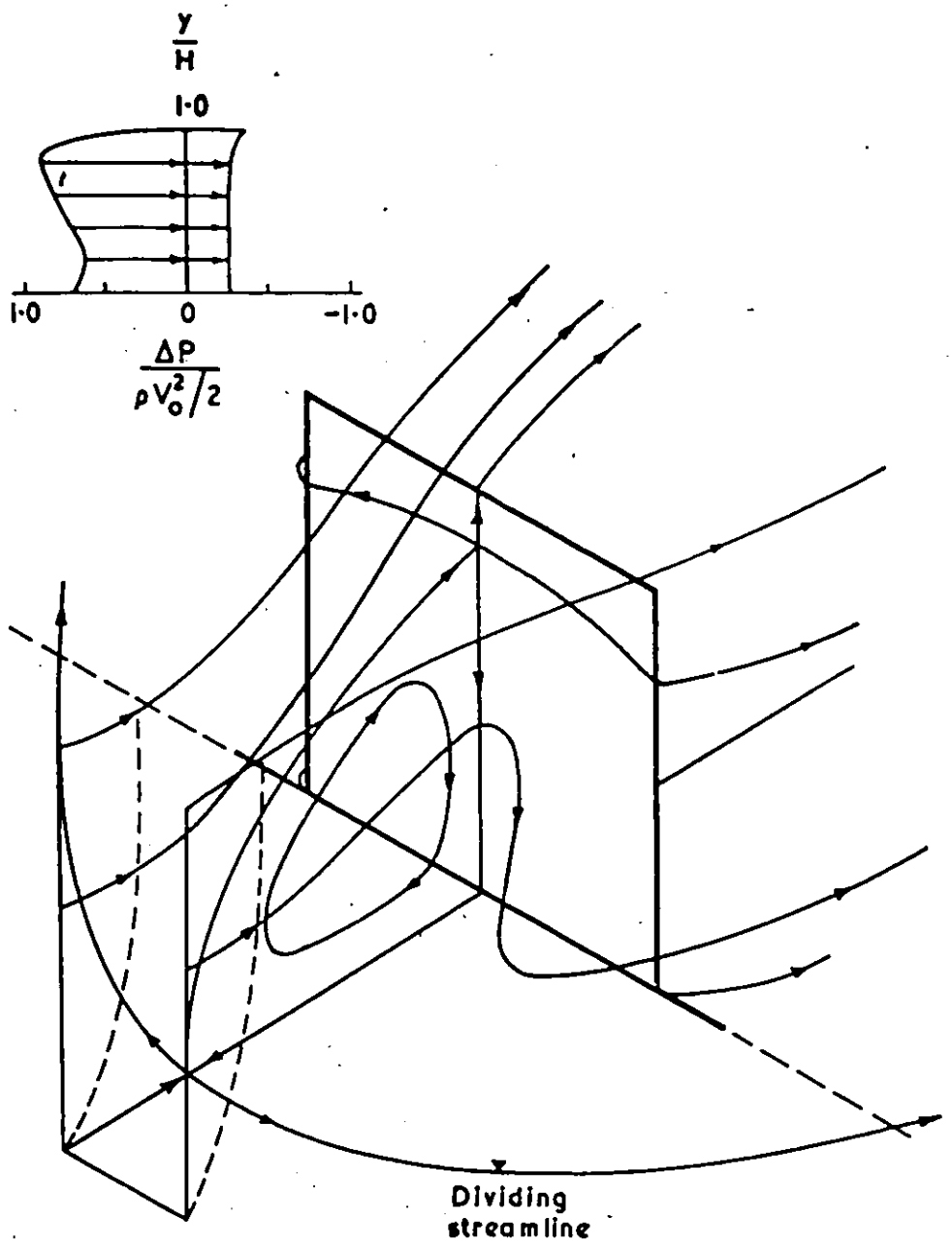

Figure 51. Flow Pattern and Centre Line Pressure Distribution on a Square Wall, (Ref. 17).

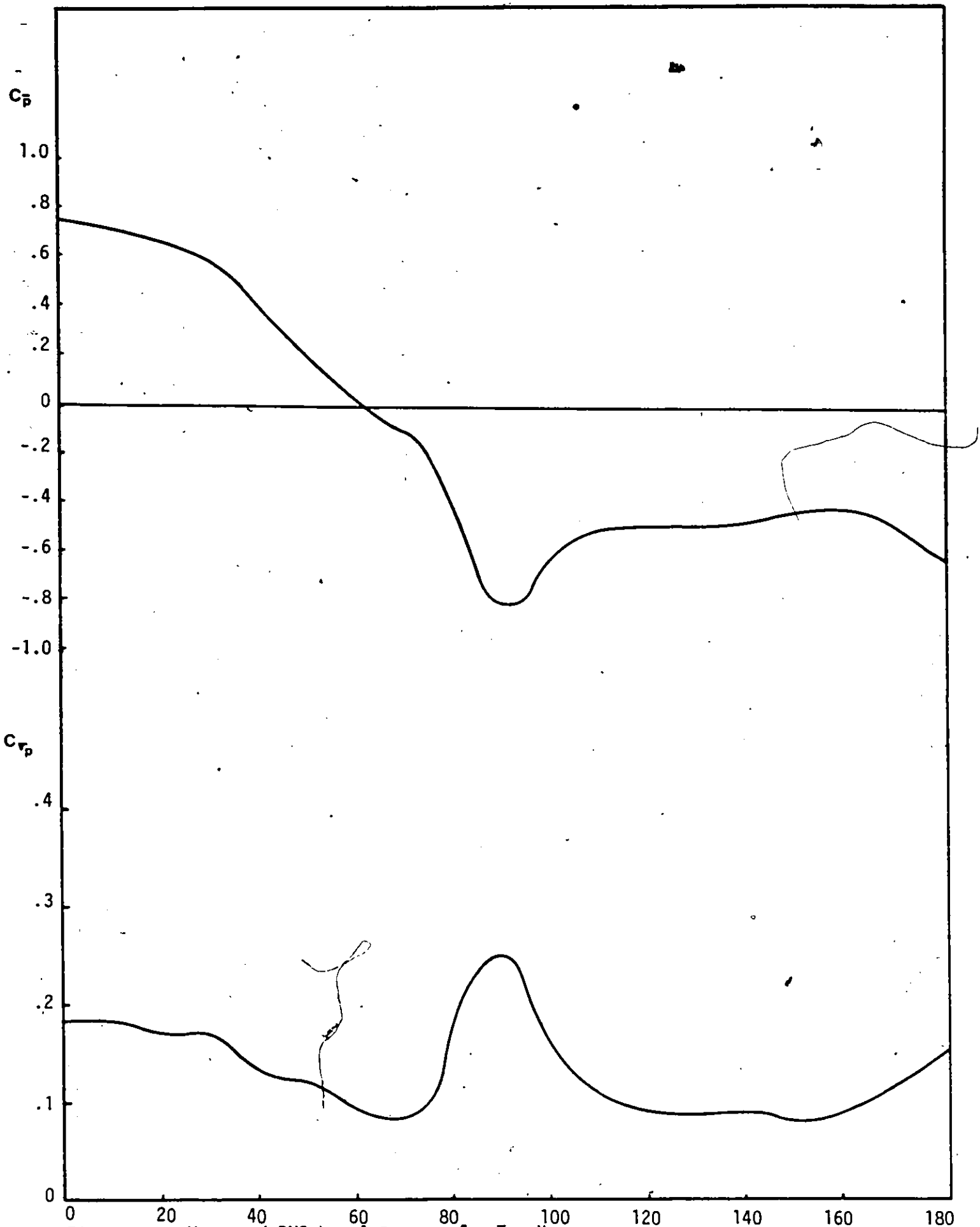

Figure 52. Mean and RMS Local Pressre for Tap No. 3 as a Function of β .

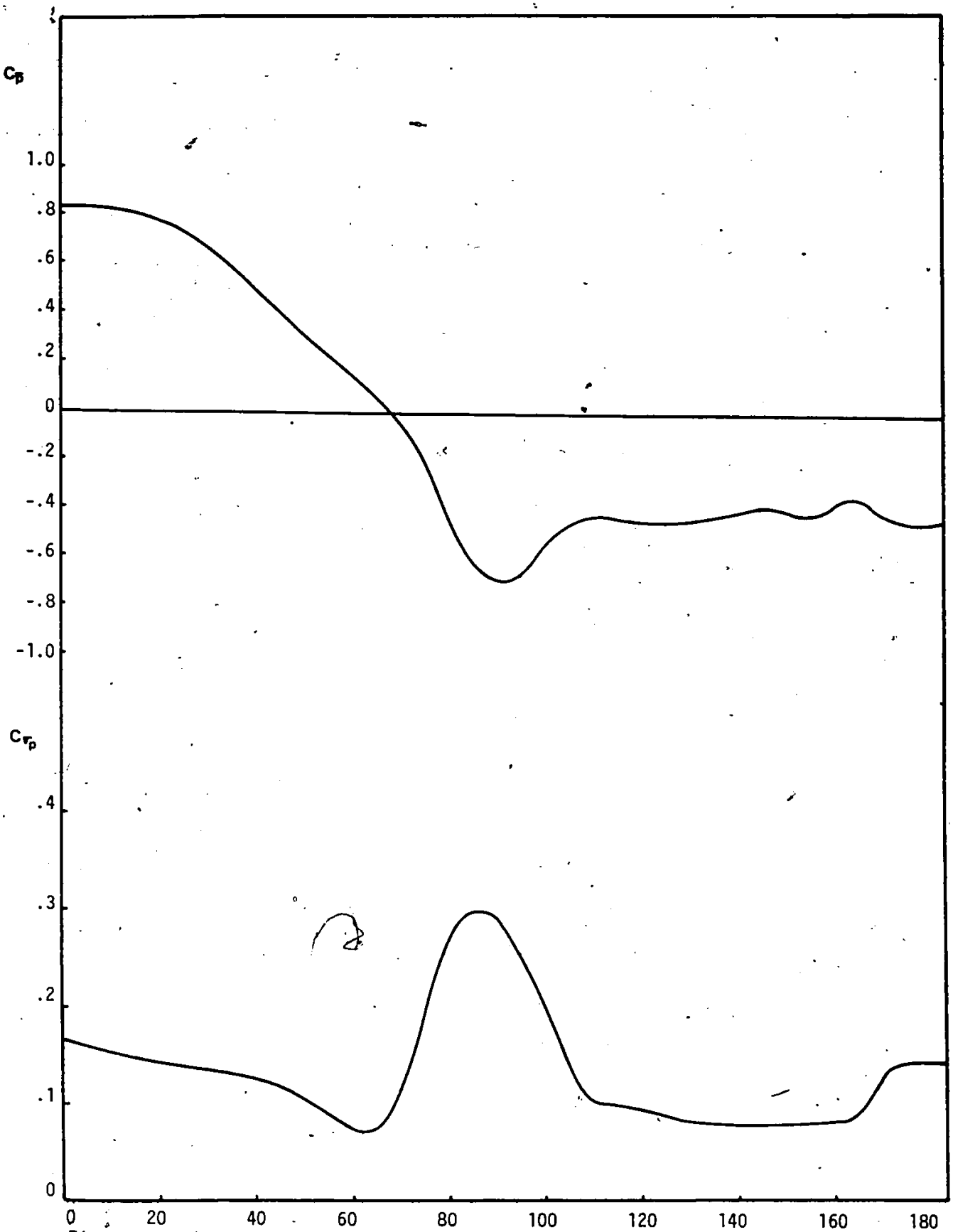

Figure 53. Mean and RMS Local Pressure for Tap No. 23 as a Function of β .

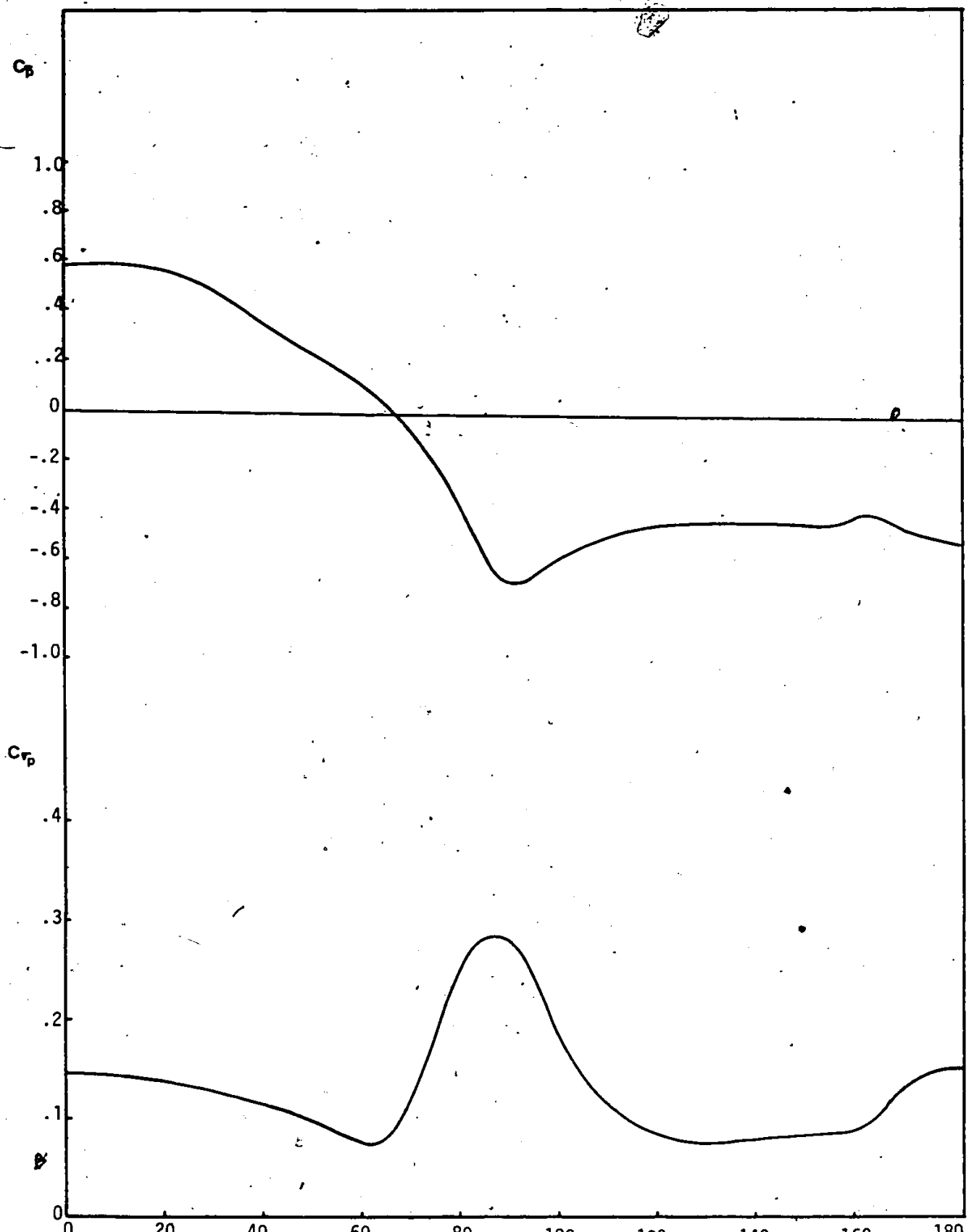

Figure 54. Mean and RMS Local Pressure for Tap No. 43 as a Function of β .

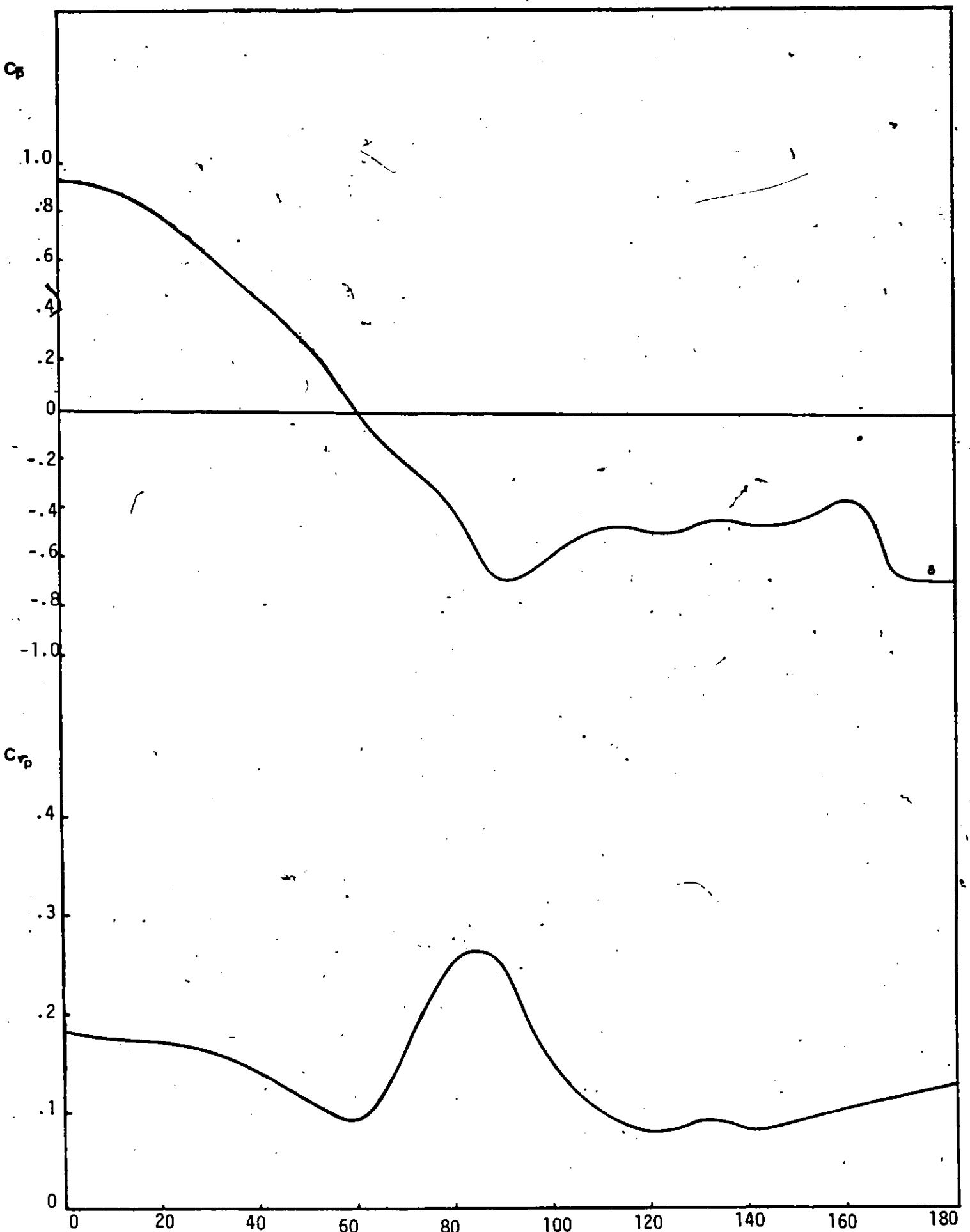

Figure 55. Mean and RMS Local Pressure for Tap No. 8 as a Function of β.

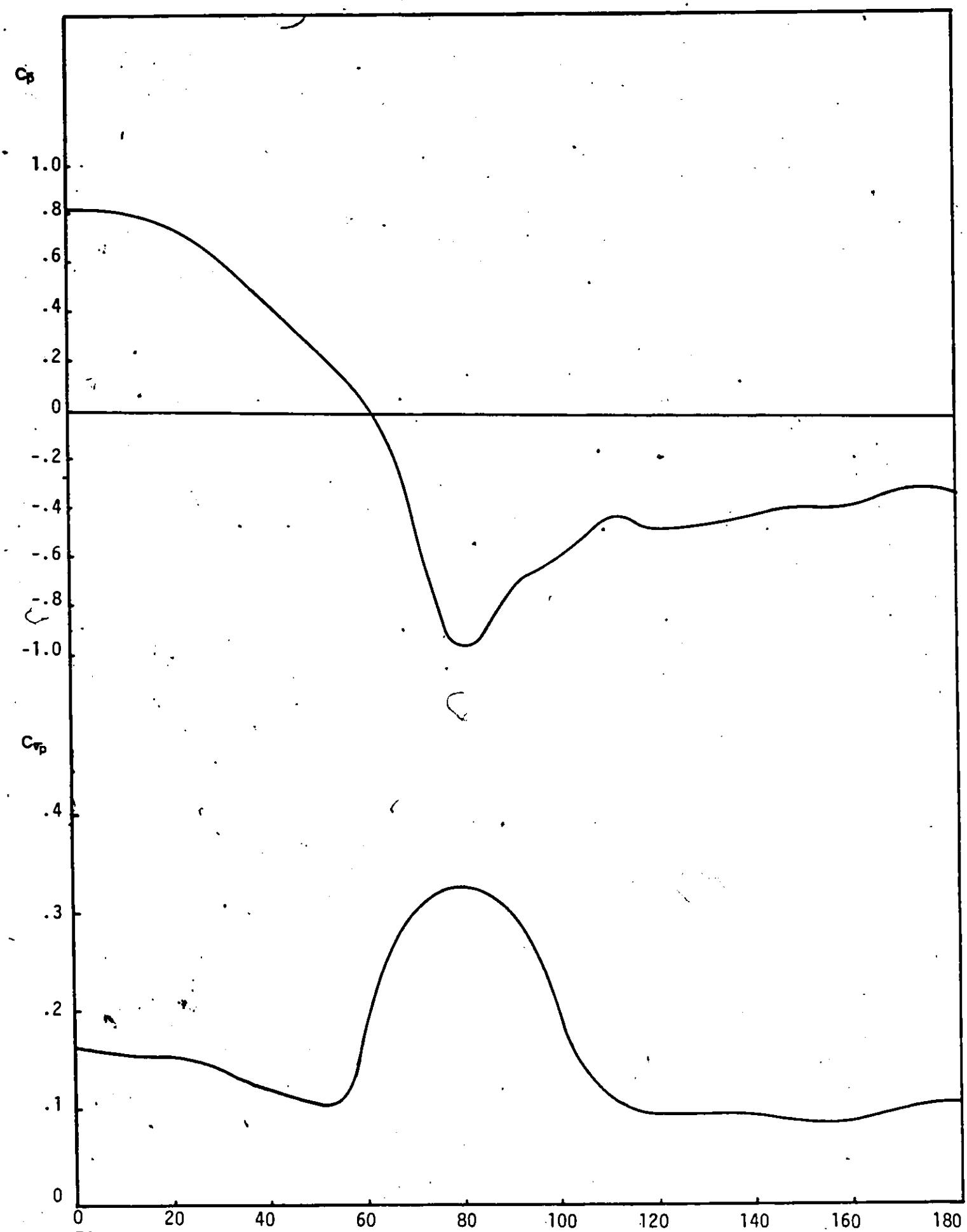

Figure 56. Mean and RMS Local Pressure for Tap No. 28 as a Function of β .

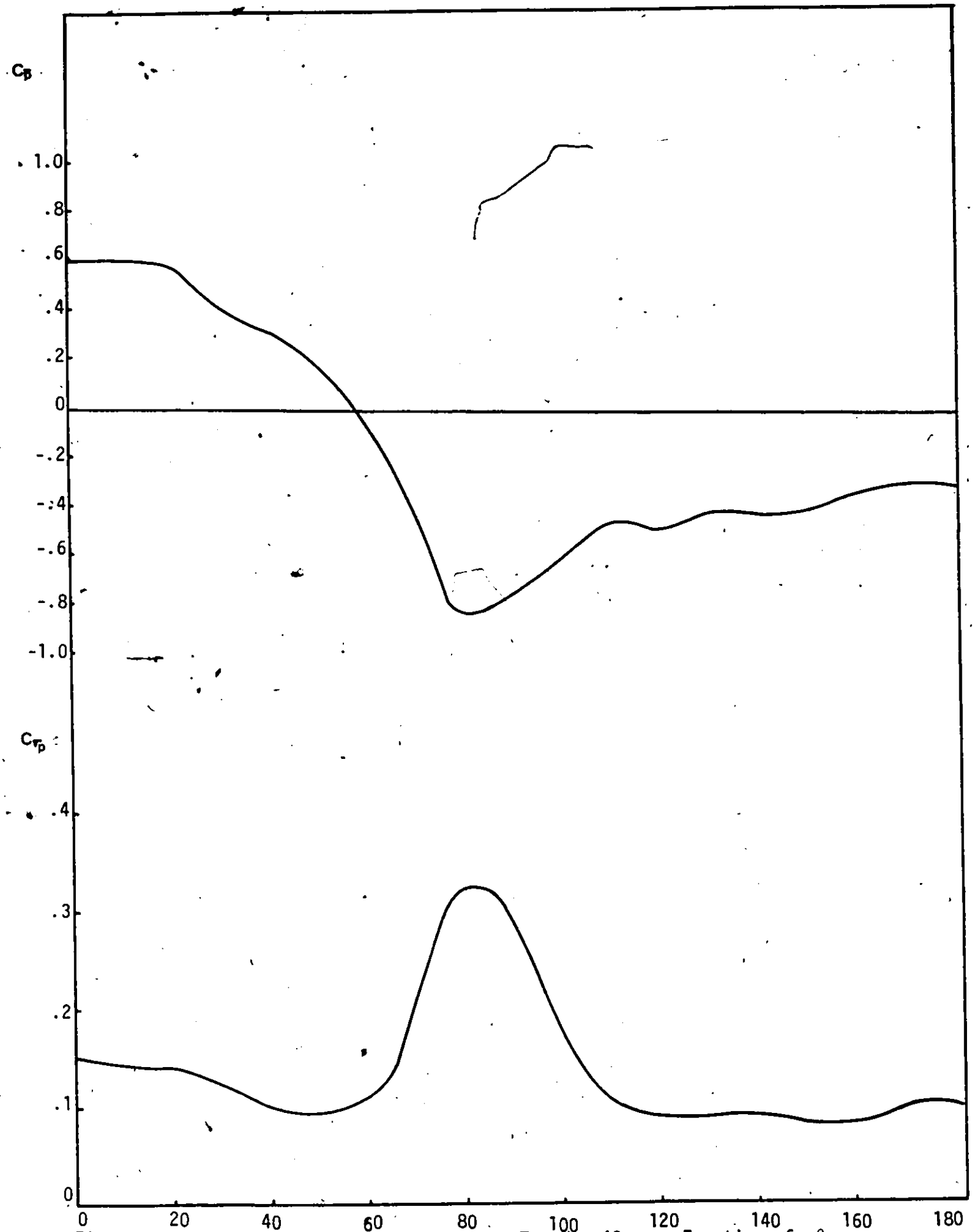

Figure 57. Mean and RMS Local Pressure for Tap No. 48 as a Function of β.

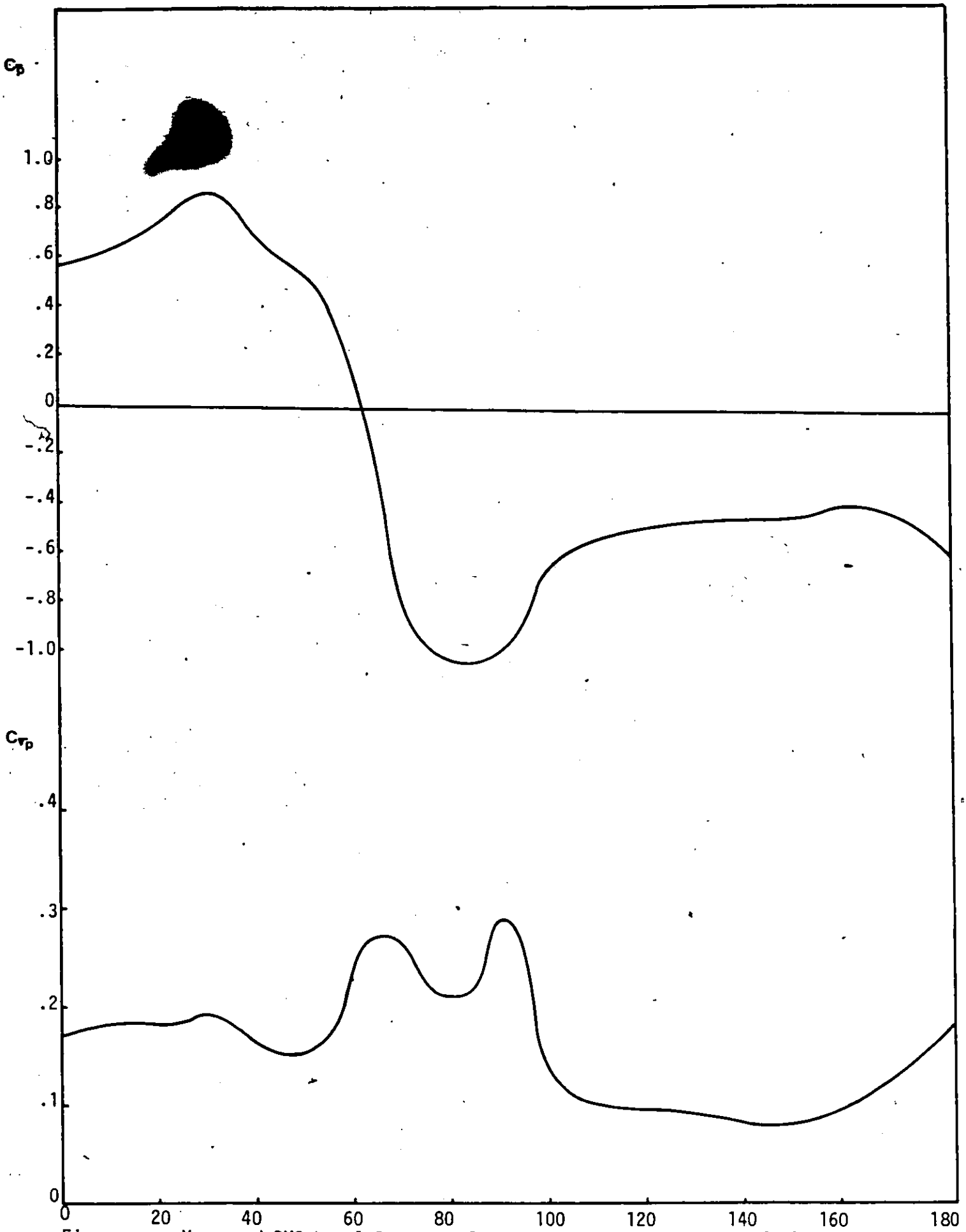

Figure 58. Mean and RMS Local Pressure for Tap No. 1 as a Function of β.

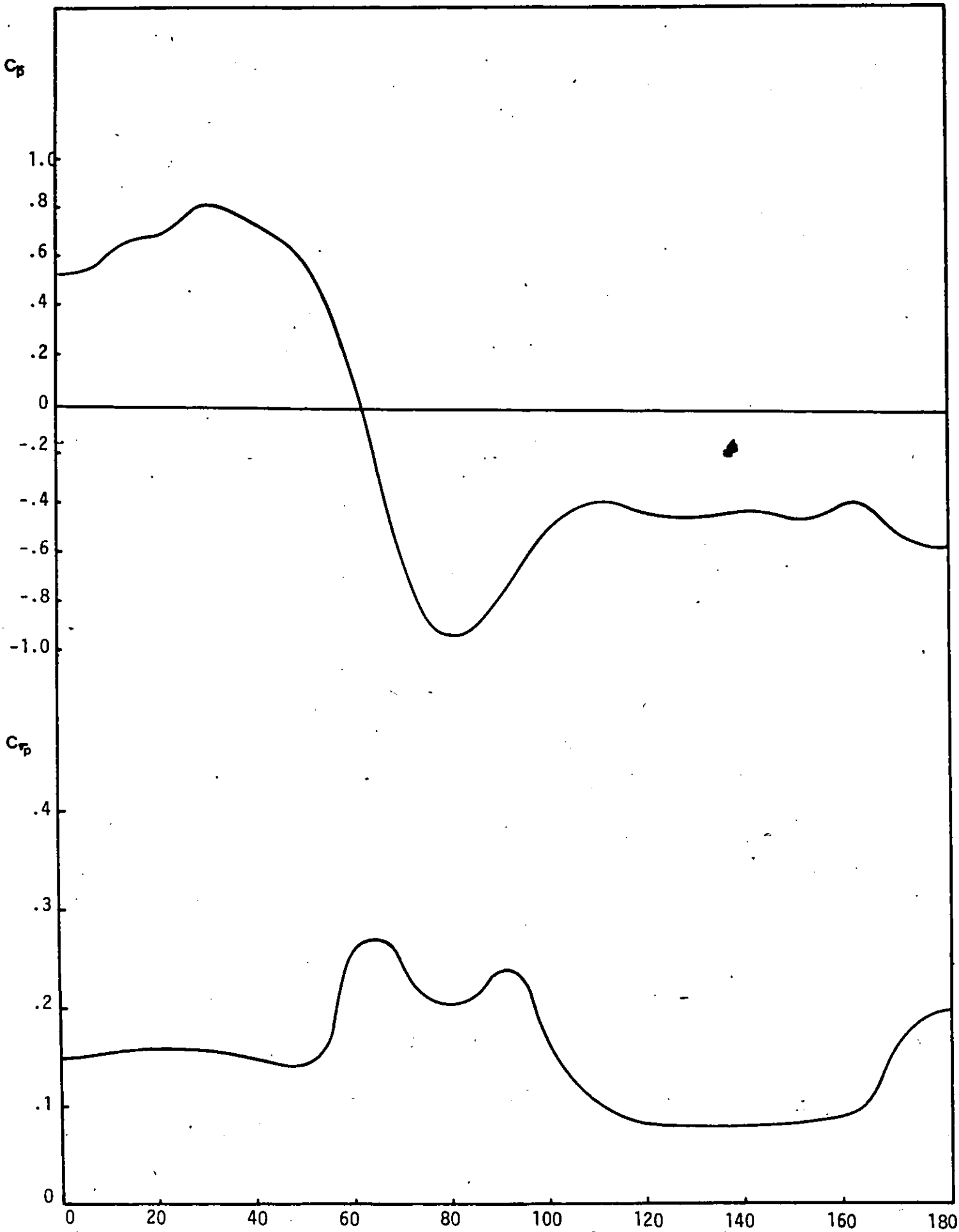

Figure 59. Mean and RMS Local Pressure for Tap No. 21 as a Function of β.

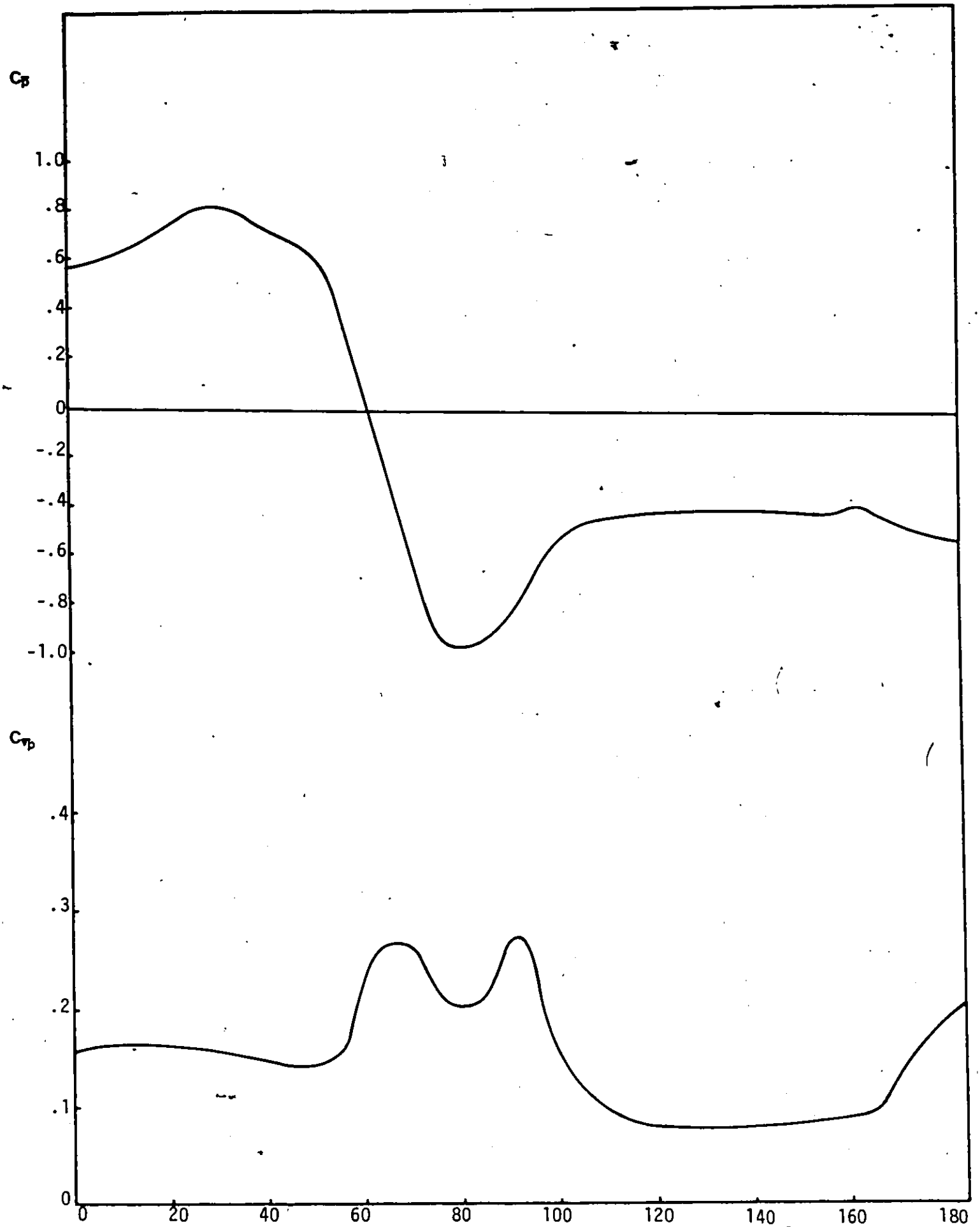

Figure 60. Mean and RMS Local Pressure for Tap No. 41 as a Function of β.

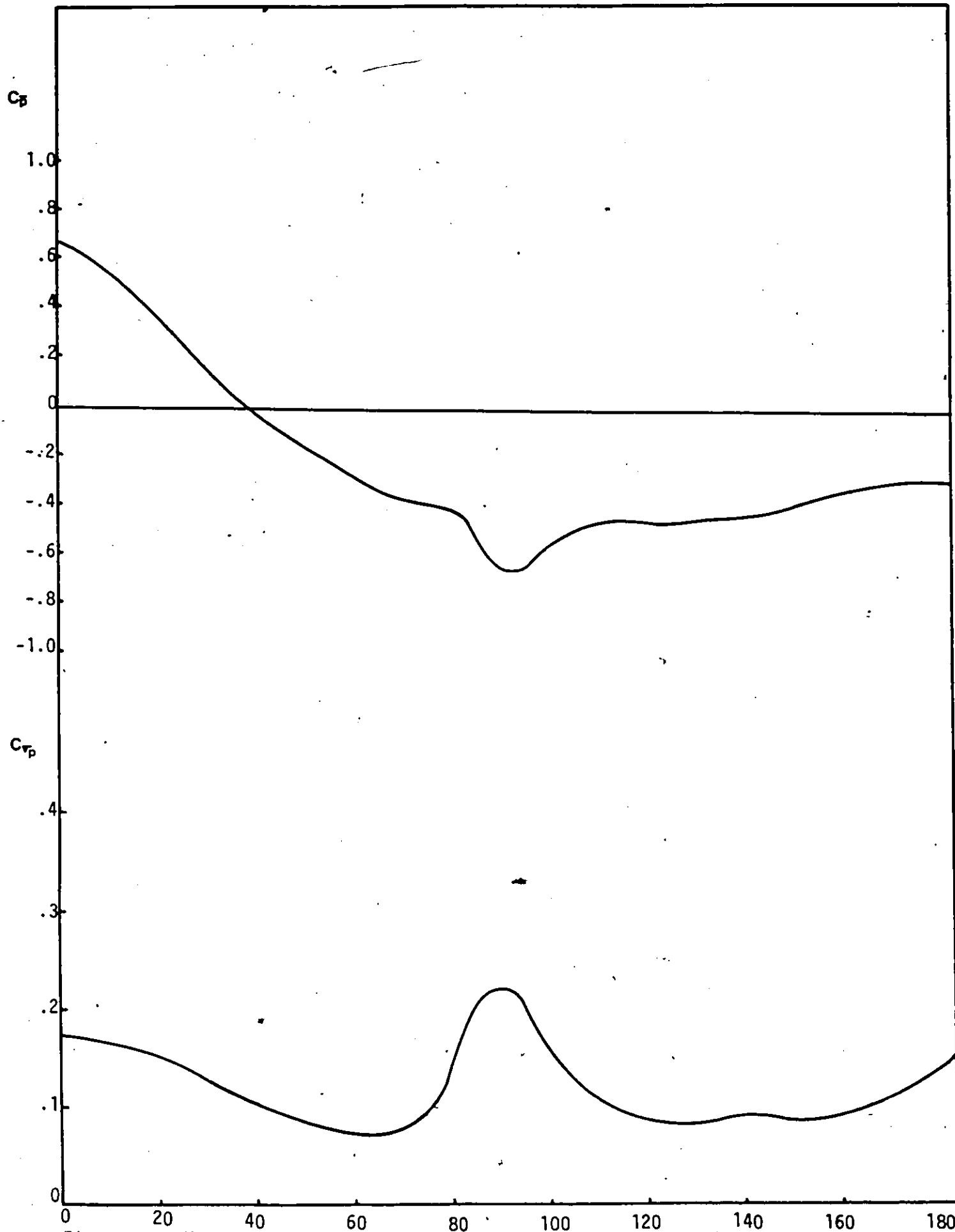

Figure 61. Mean and RMS Local Pressure for Tap No. 6 as a Function of β.

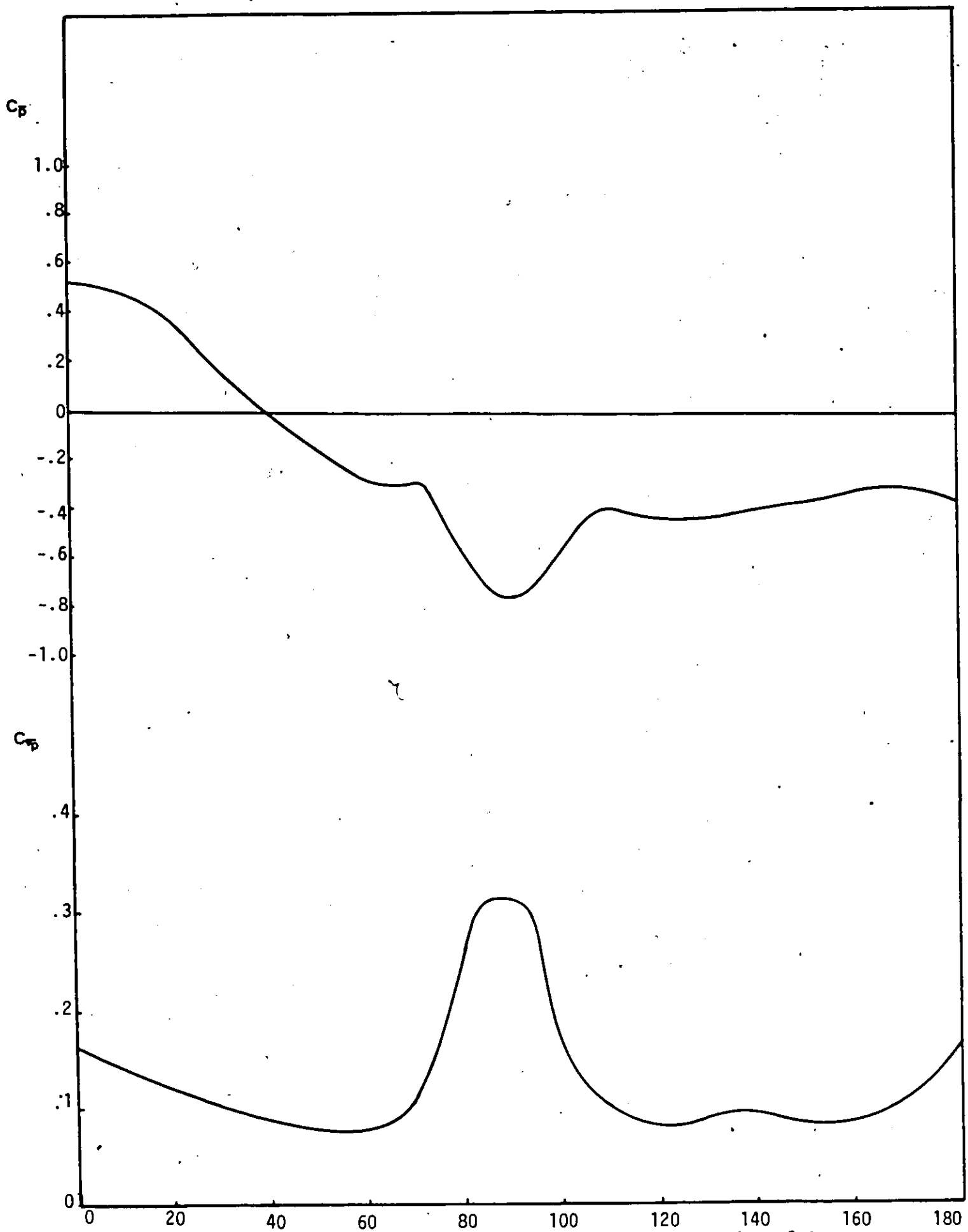

Figure 62. Mean and RMS Local Pressure for Tap No. 26 as a Function of β.

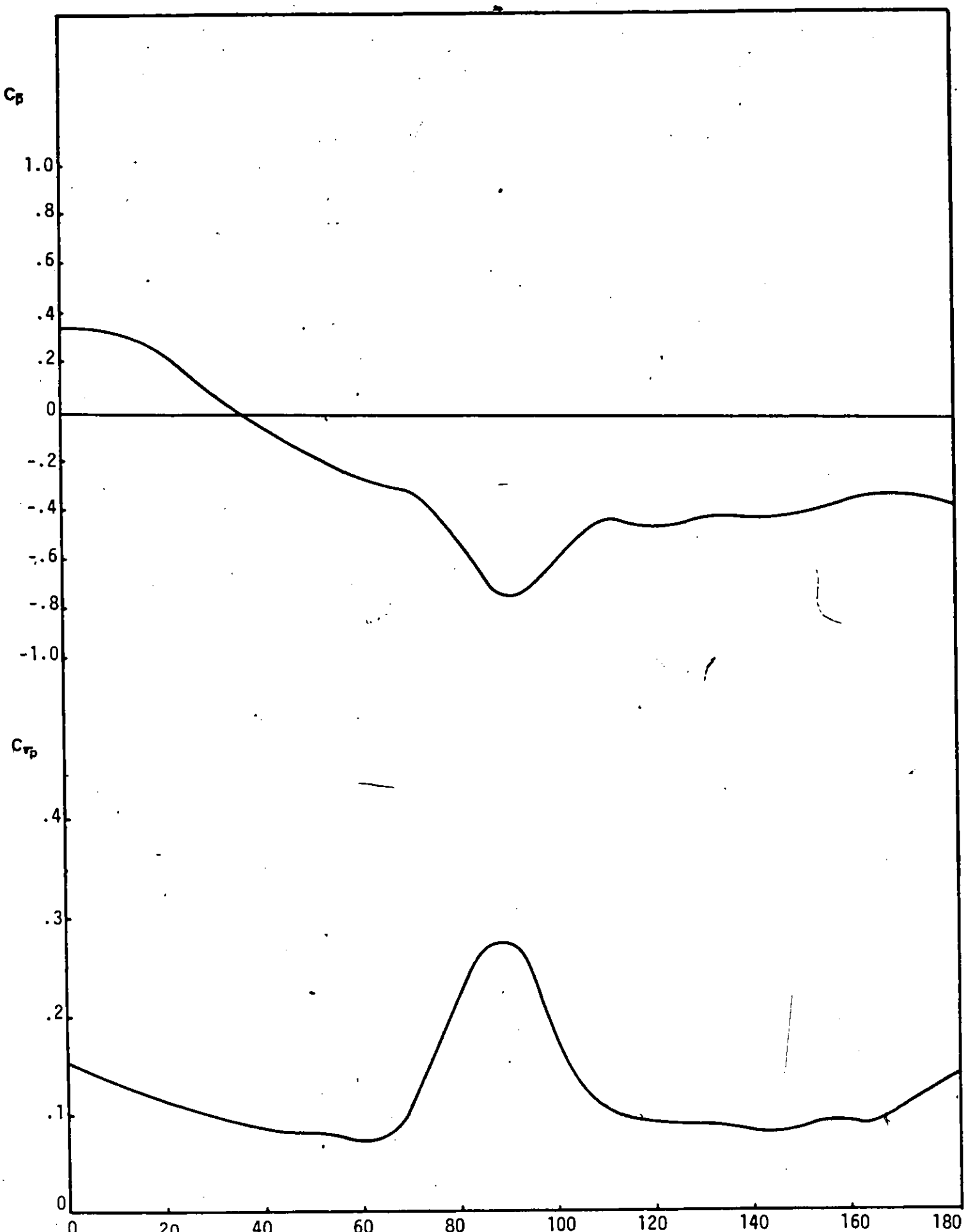

Figure 63. Mean and RMS Local Pressure for Tap No. 46 as a Function of β .

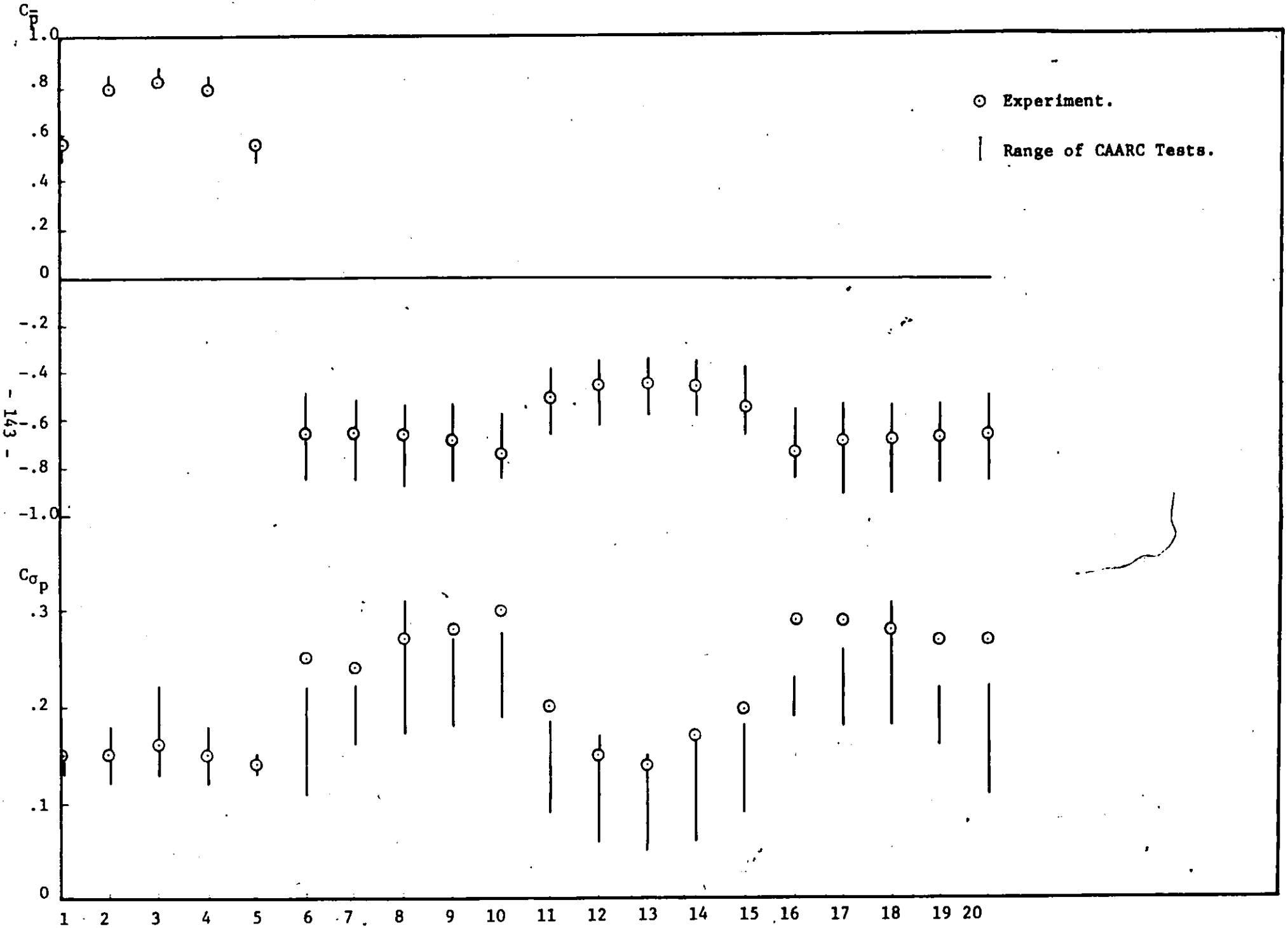

Figure 64 . Comparison of $C_{\bar{p}}$ aand C_{σ_p} with CAARC Results for $\beta = 0^{\circ}$ at Z = 2/3 H.

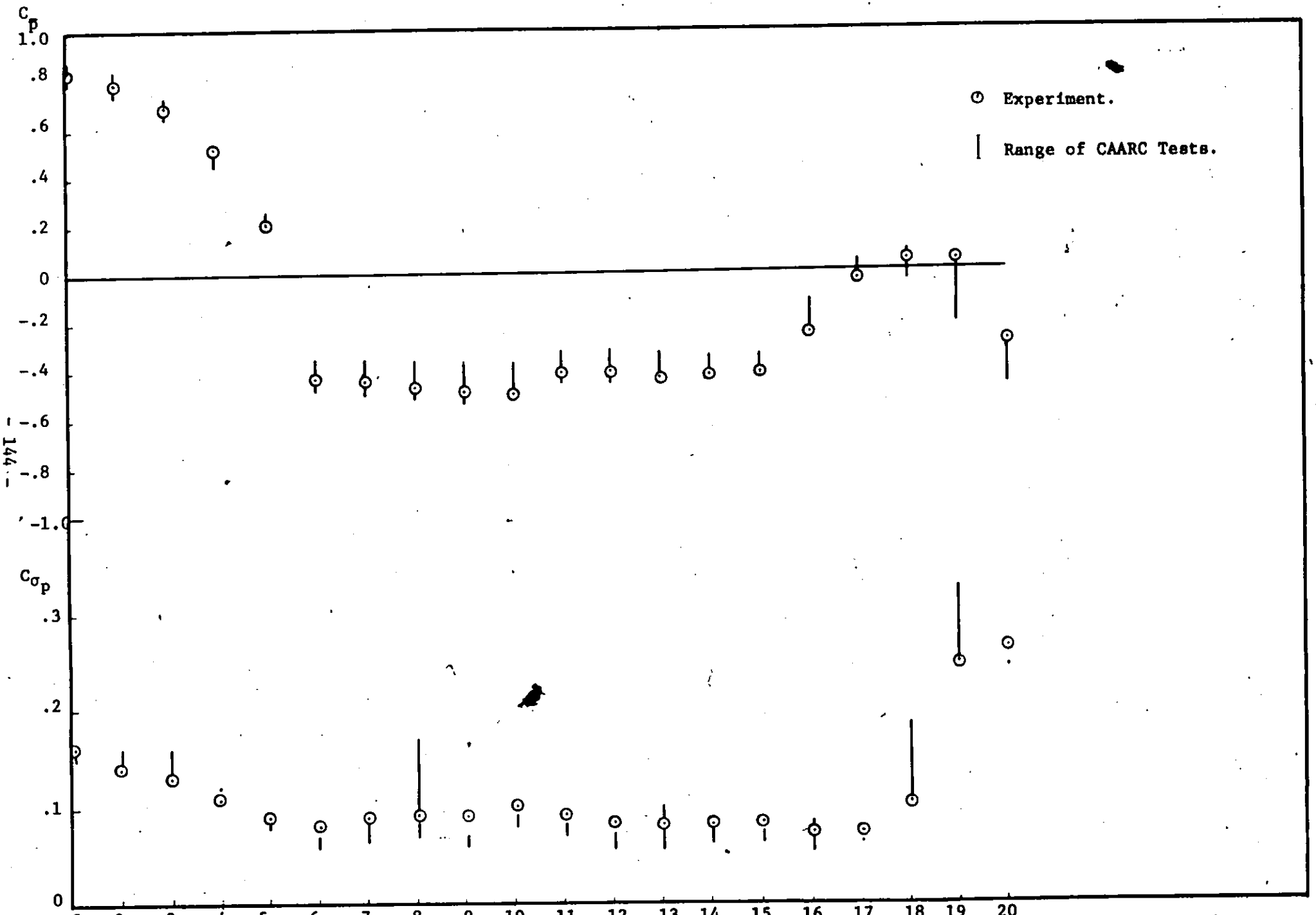

Figure 65. Comparison of C_p and $C\sigma_p$ with CAARC Results for $\beta = 30^0$ at Z = 2/3 H.

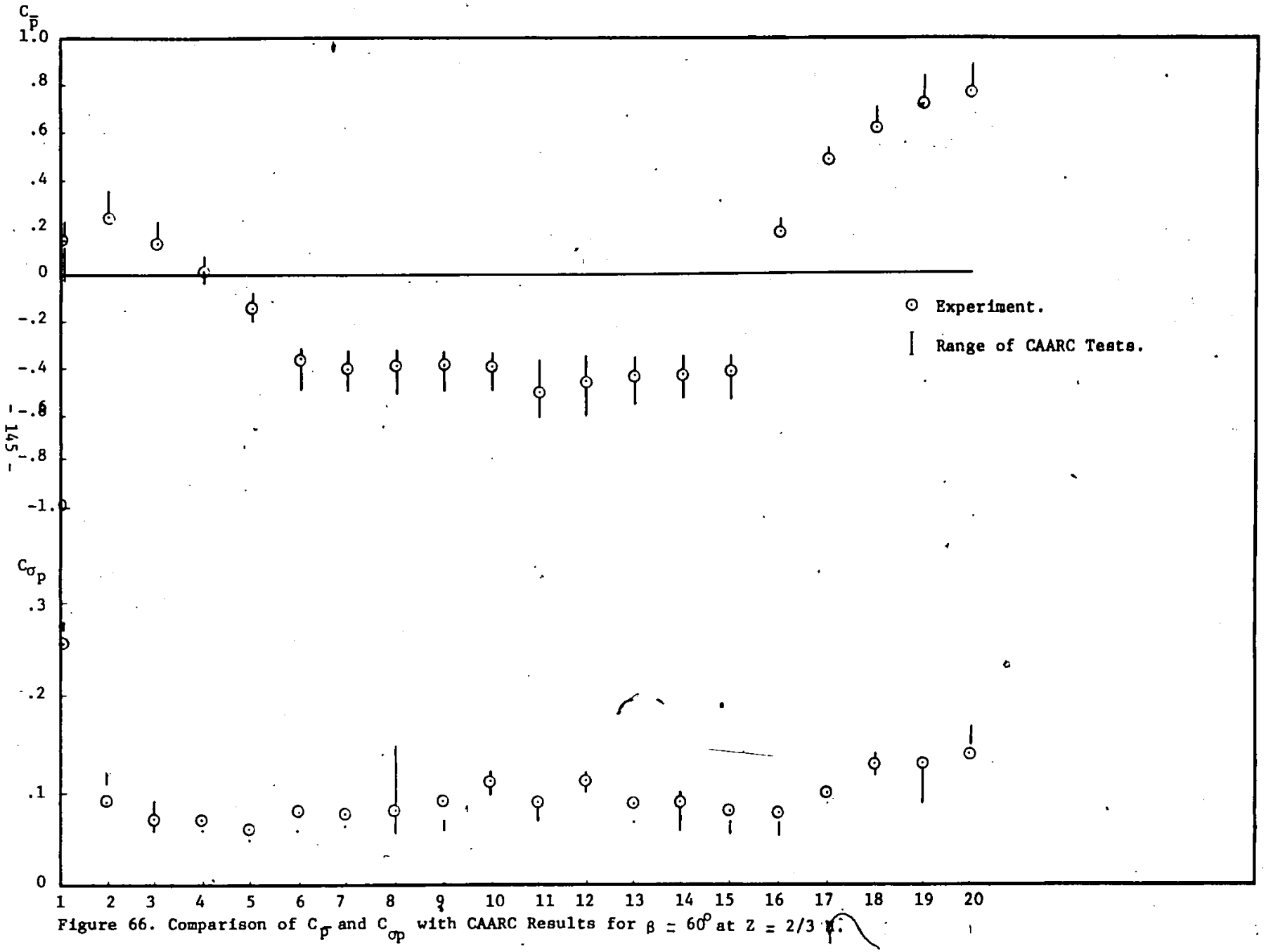

Figure 66. Comparison of $C_{\bar{p}}$ and $C_{\sigma p}$ with CAARC Results for $\beta = 60^{\circ}$ at Z = 2/3 H.

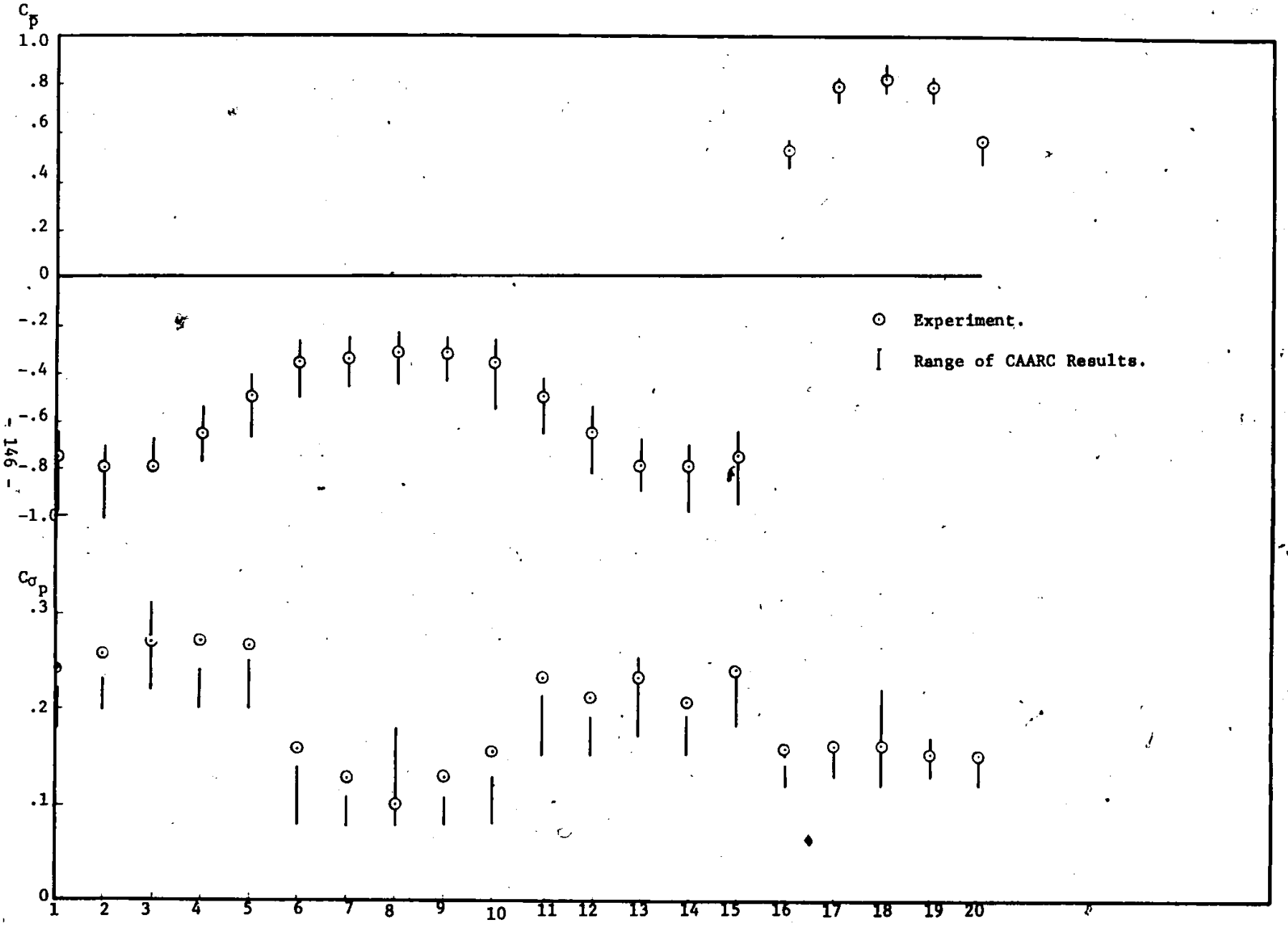

Figure 67. Comparison of $C_{\bar{p}}$ and C_{σ_p} with CAARC Results for $\beta = 90^o$ at Z = 2/3 H.

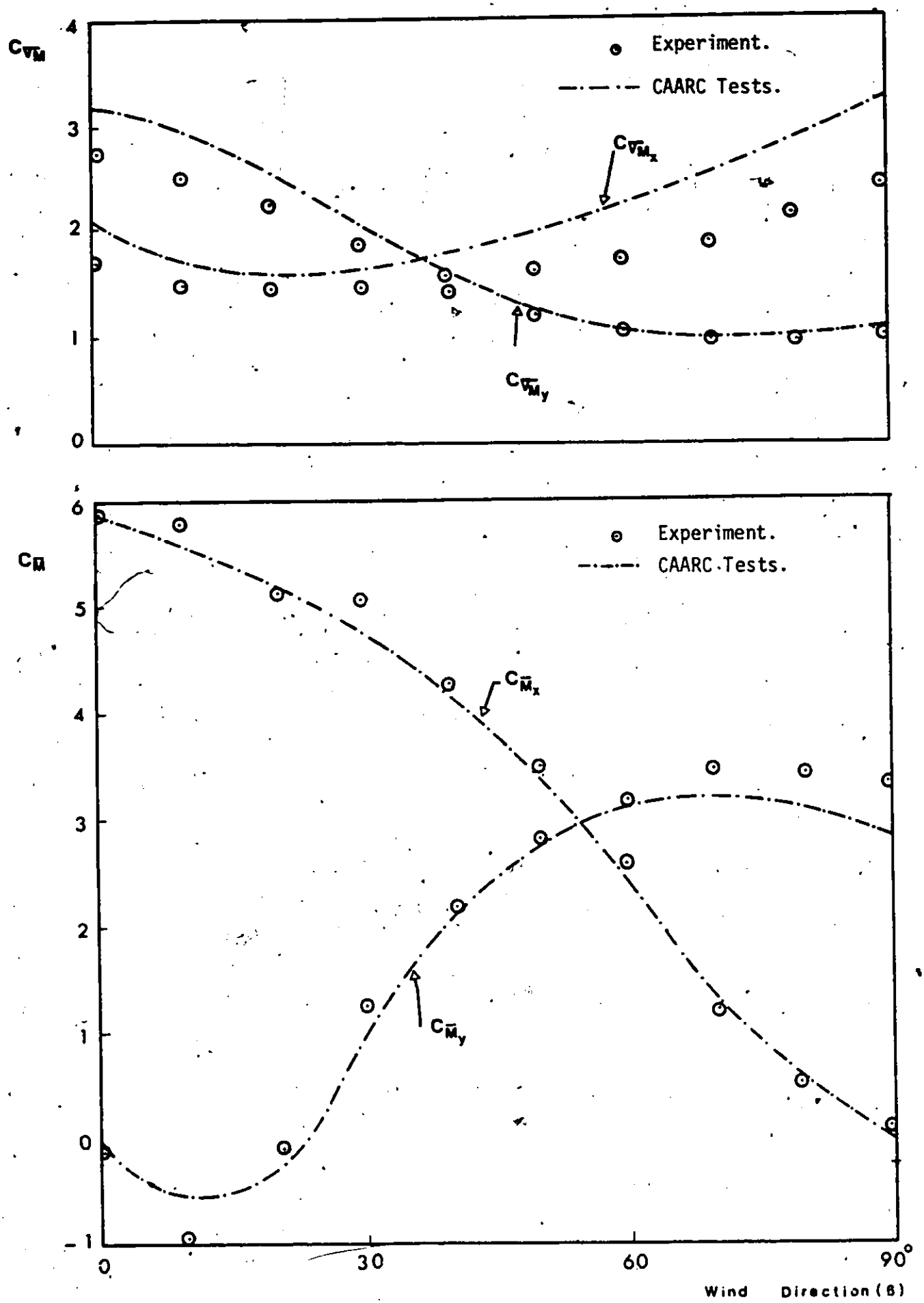

Figure 68. Base Overturning Moment as a Function of β for the CAARC Model.

Figure 69. NBC Pressure Coefficient for Tall Building, (Ref. 18).

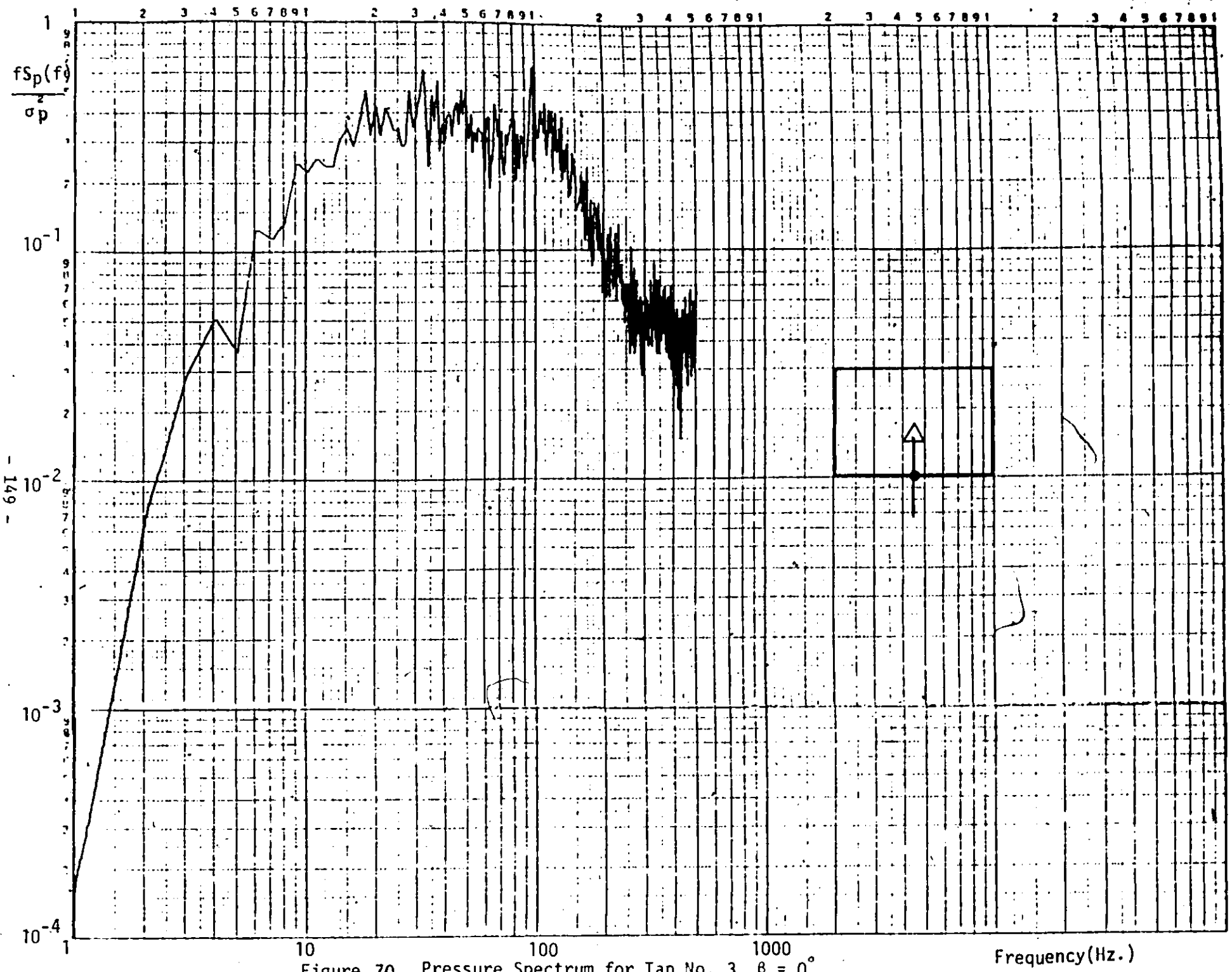

Figure 70. Pressure Spectrum for Tap No. 3, $\beta = 0^\circ$.

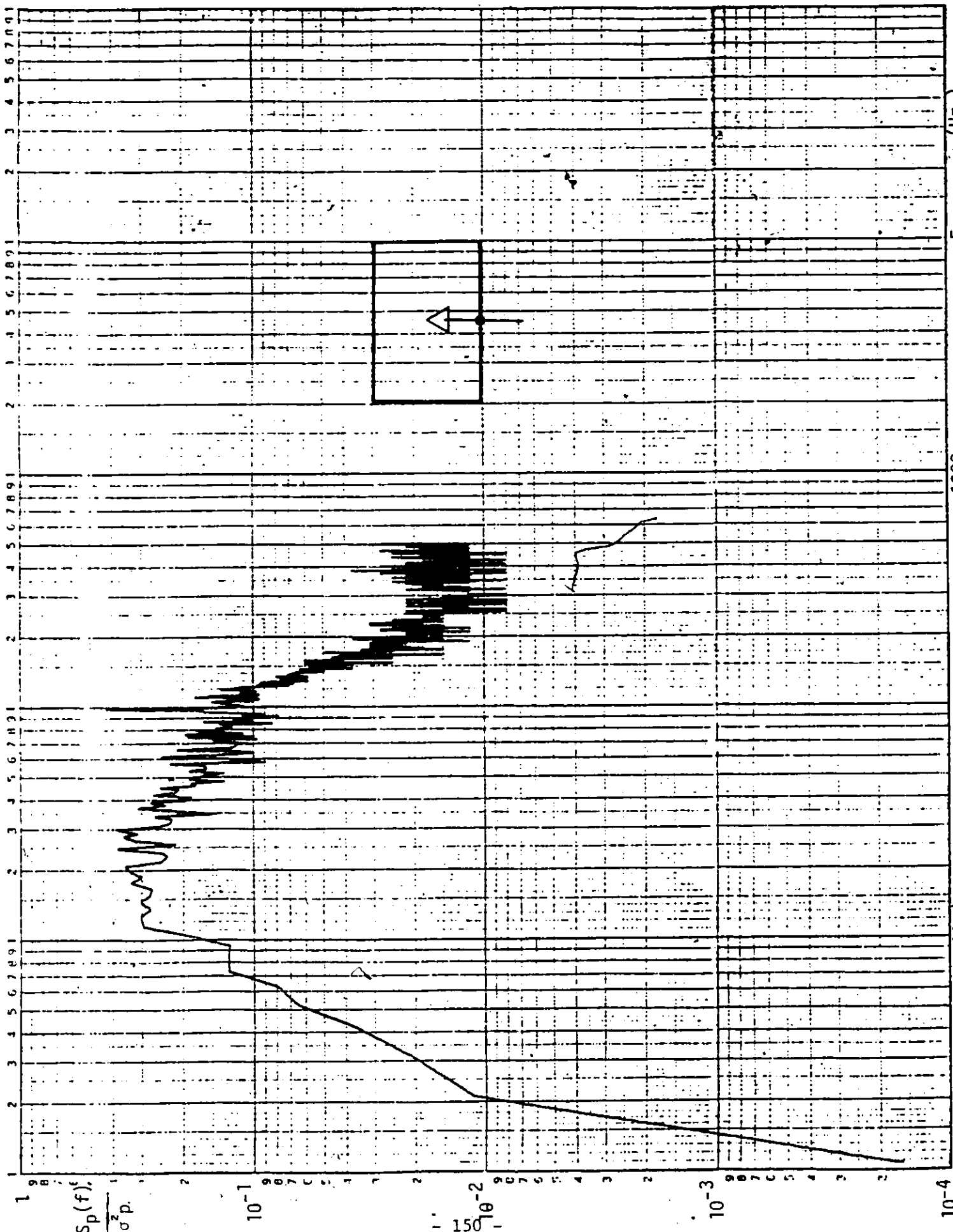

Figure 71. Pressure Spectrum for Tap No. 23, $\beta = 0$.

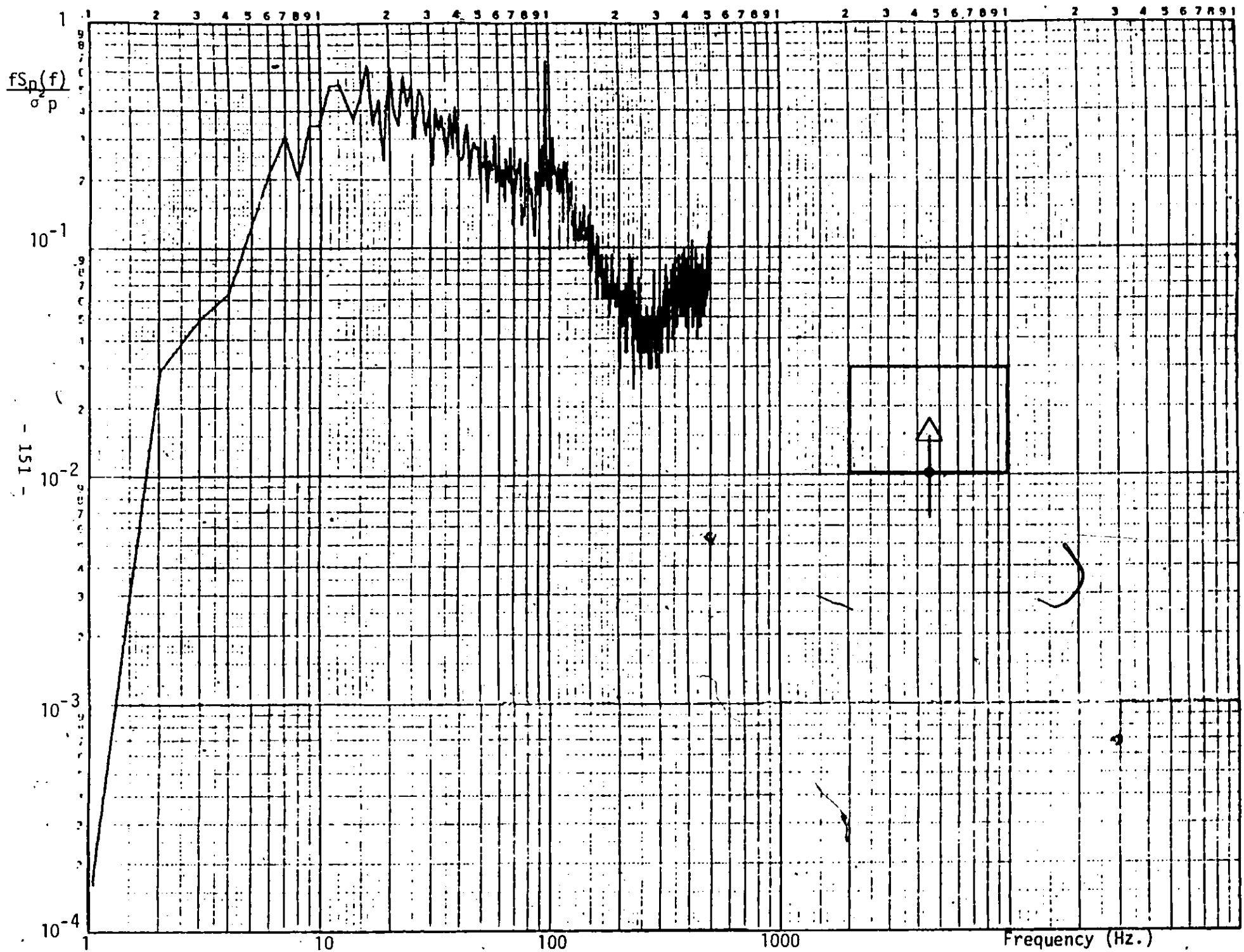

Figure 72. Pressure Spectrum for Tap No. 43, $\beta = 0$.

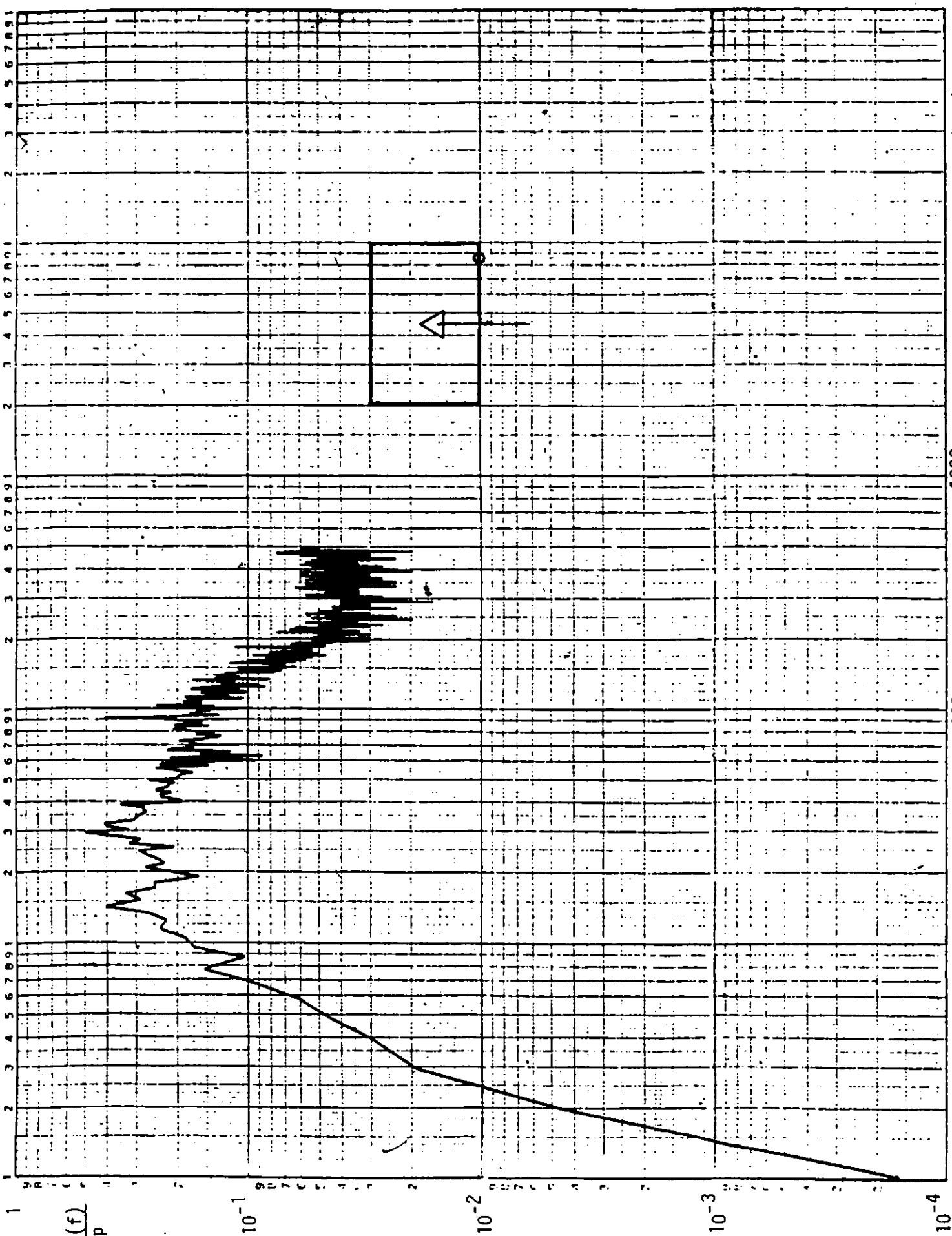

Figure 73, Pressure Spectrum for Tap No.25, $\beta = 0$.

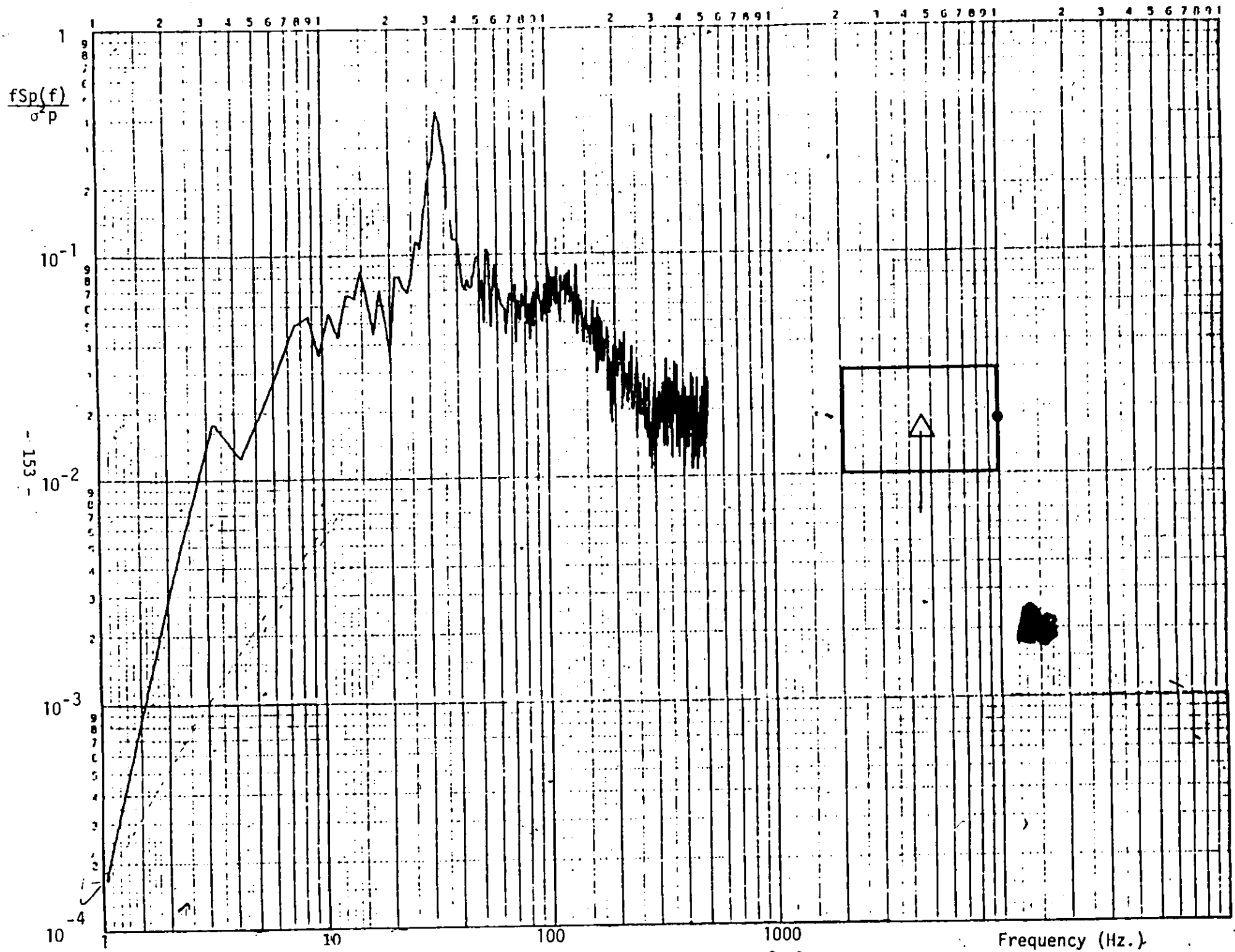

Figure 74. Pressure Spectrum for Tap No. 8, β =0.

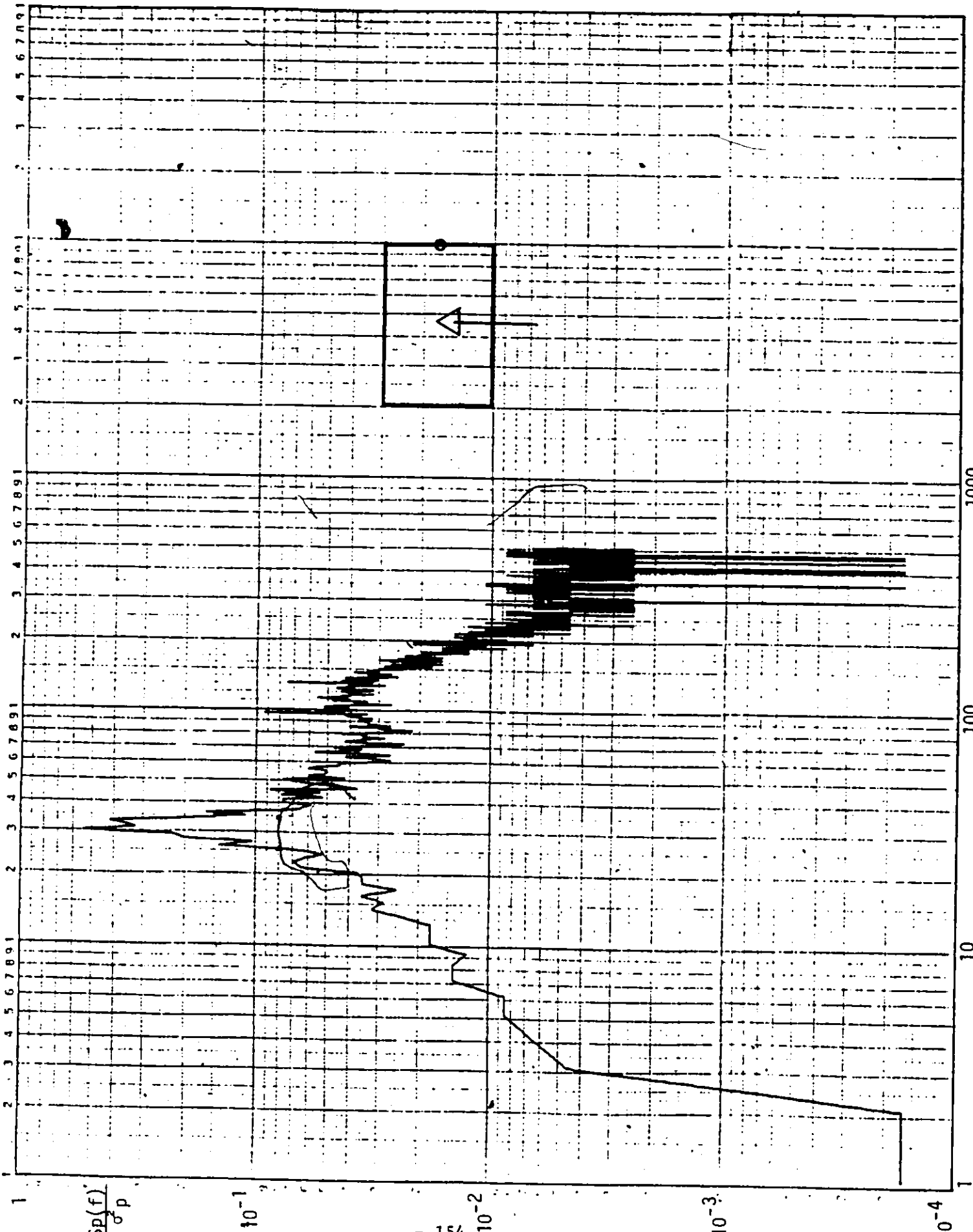

Figure 75. Pressure Spectrum for Tap No. 28, $\beta = 0$.

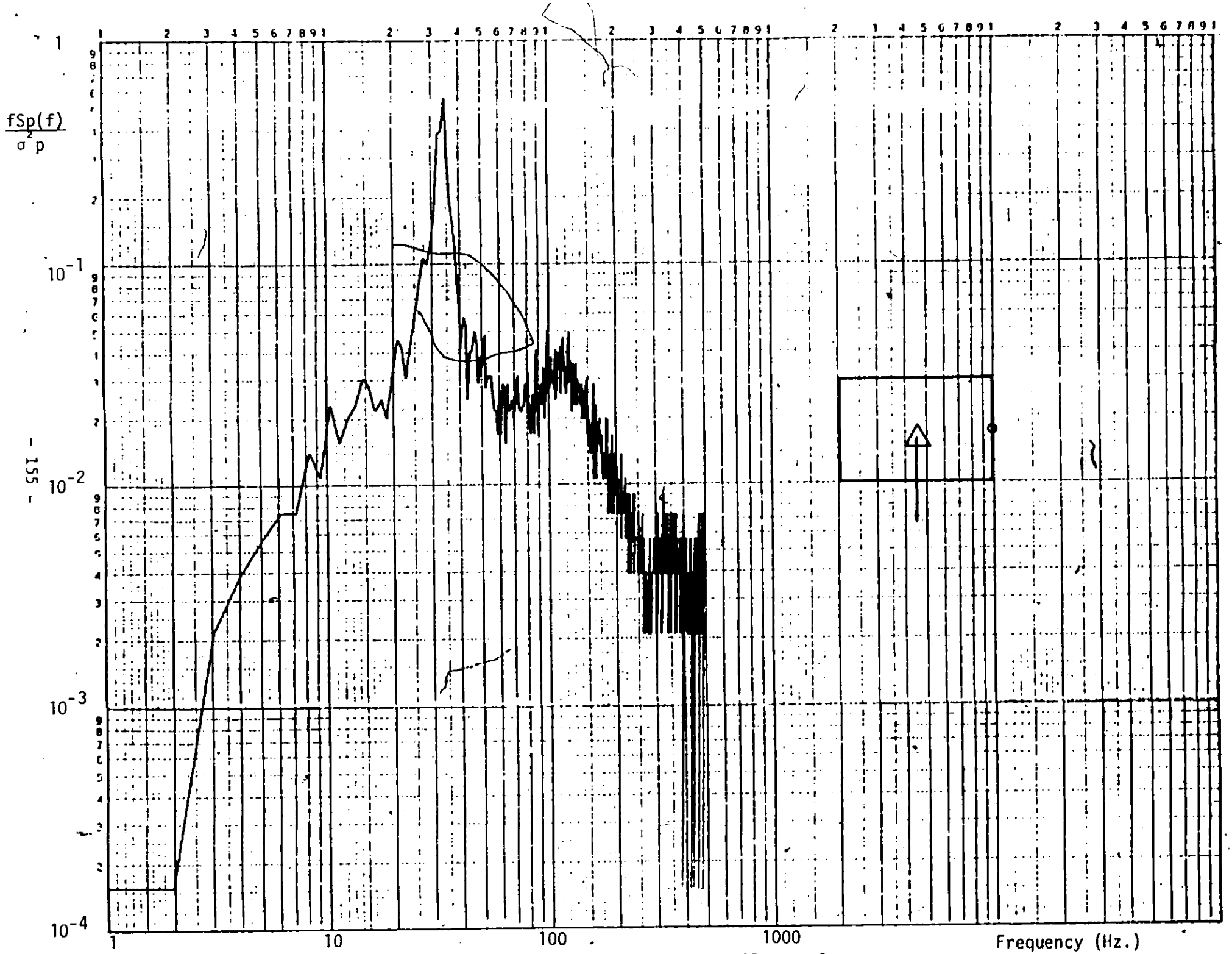

Figure 76. Pressure Spectrum for Tap No. 48, β = 0 .

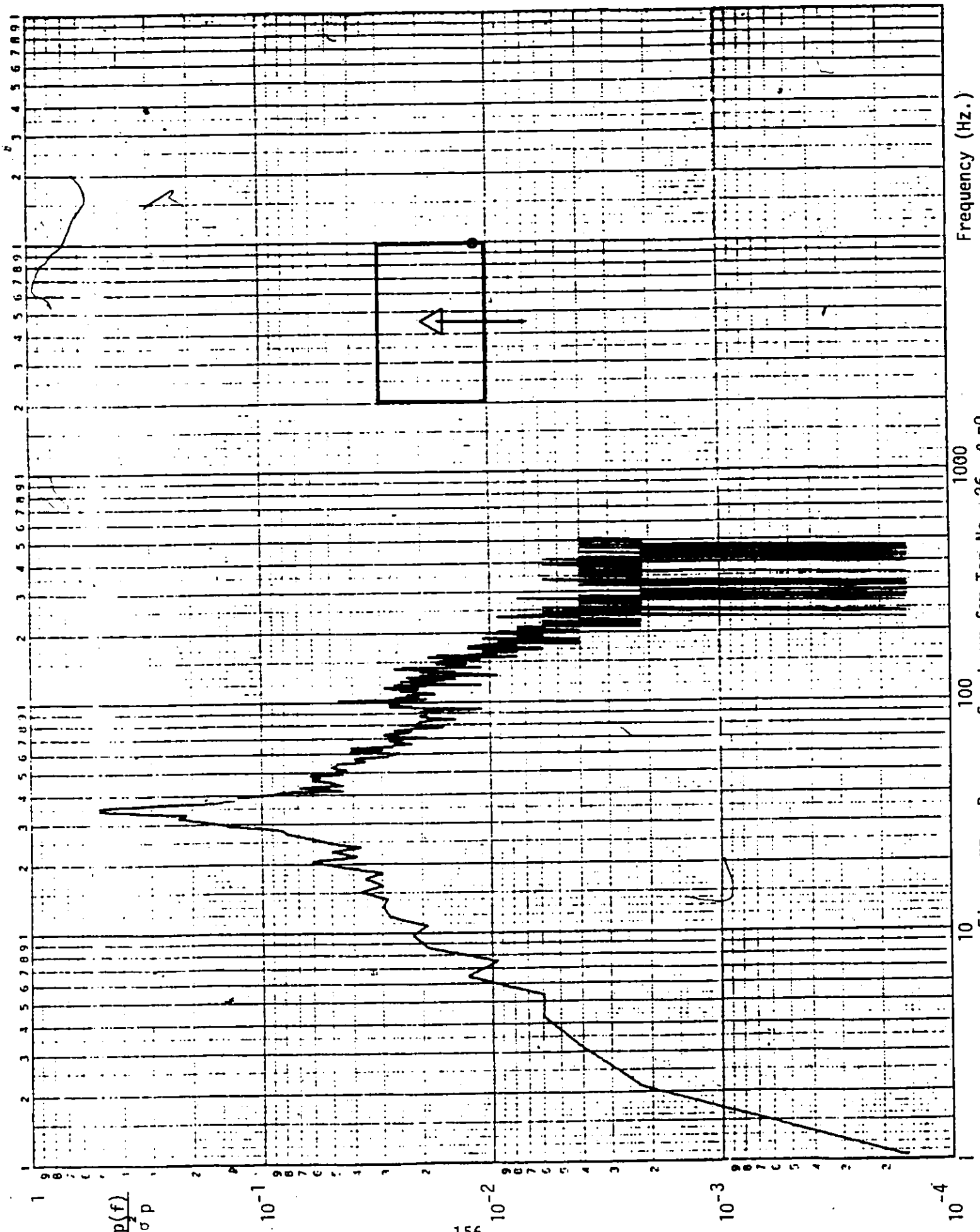

Figure 77. Pressure Spectrum for Tap No. 26, $\beta = 0$.

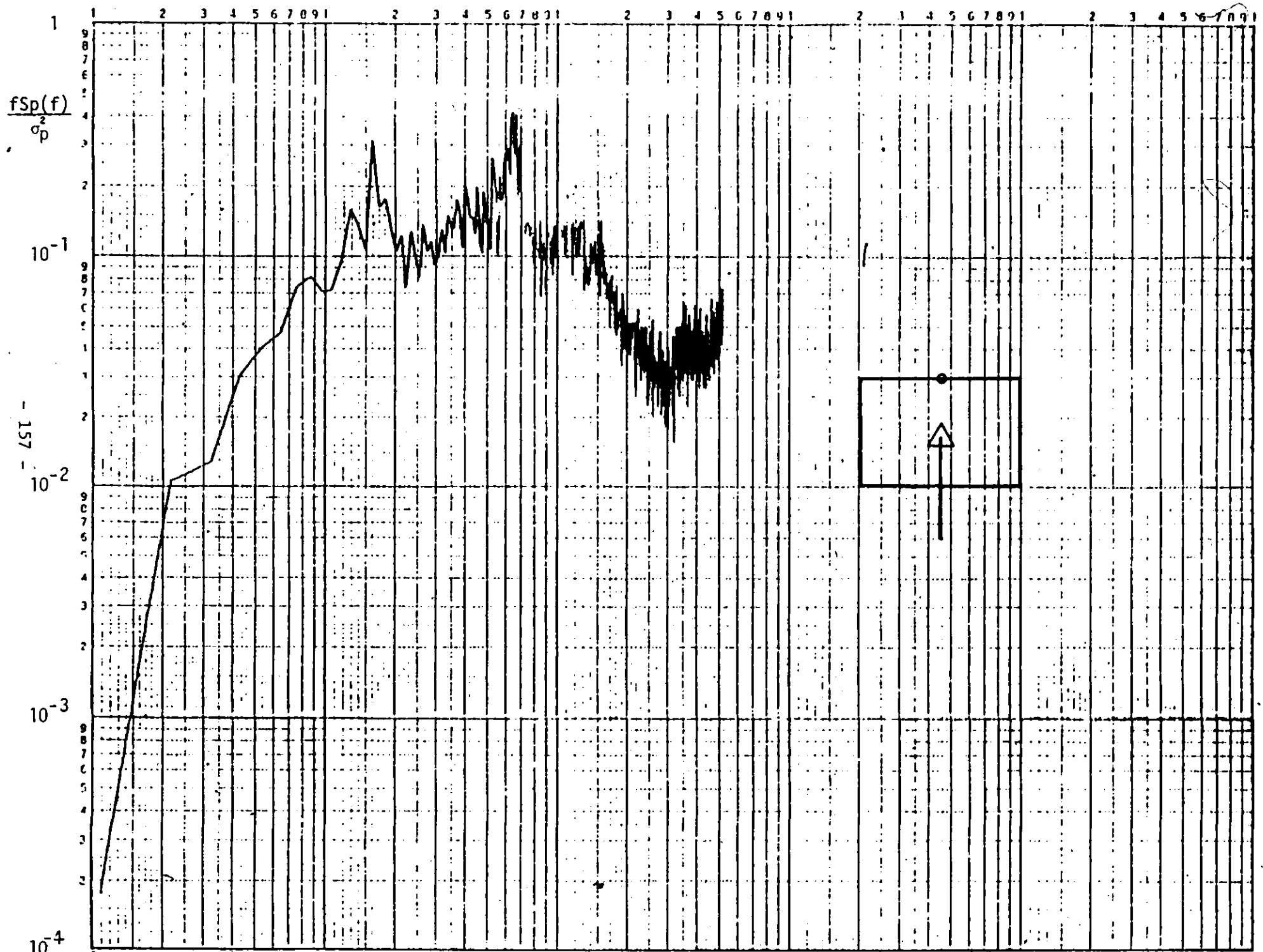

Figure 78. Pressure Spectrum for Tap No. 13, $\beta = 0$.

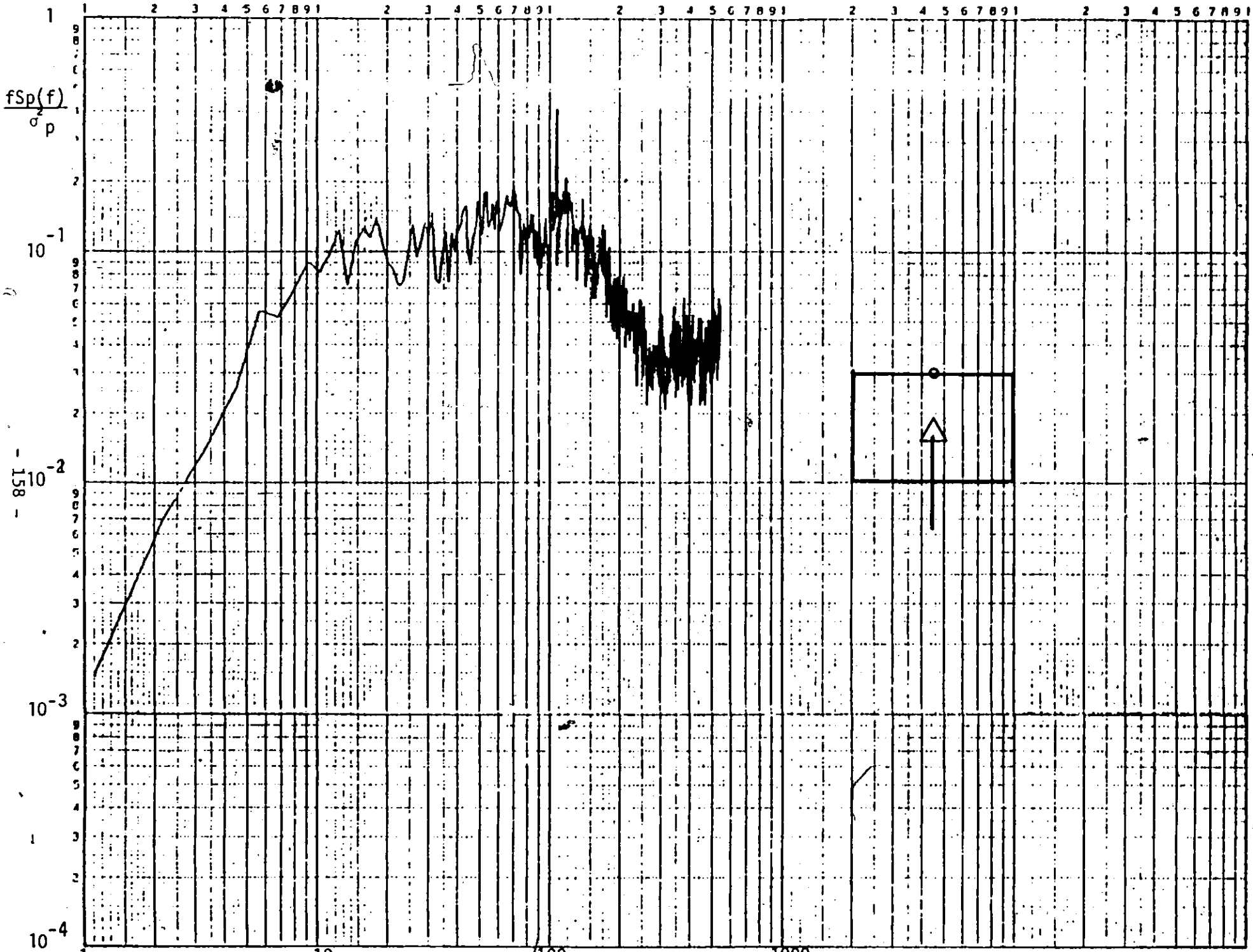

Figure 79. Pressure Spectrum for Tap No. 33, β = 0.

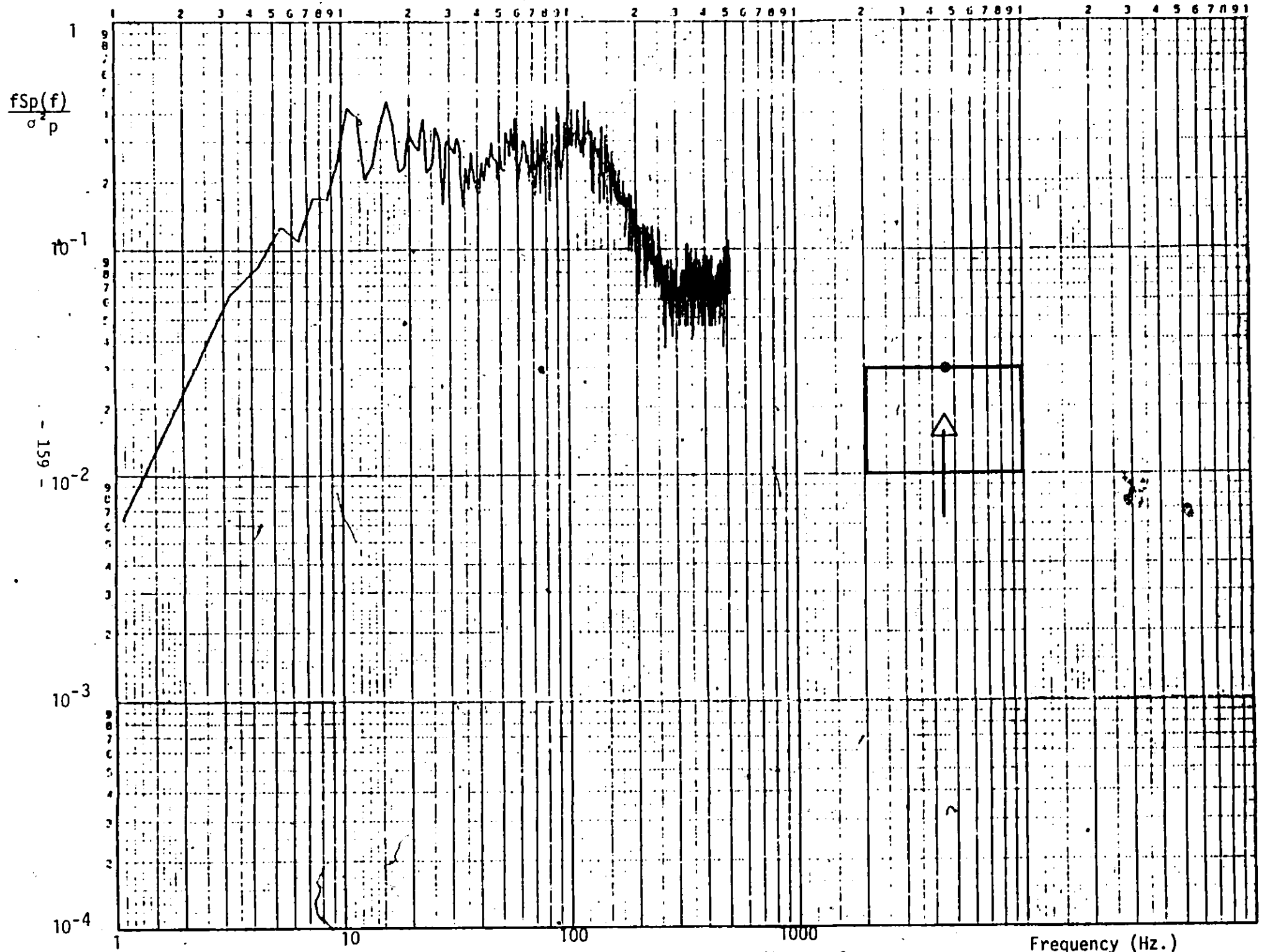

Figure 80. Pressure Spectrum for Tap No. 53, $\beta = 0$.

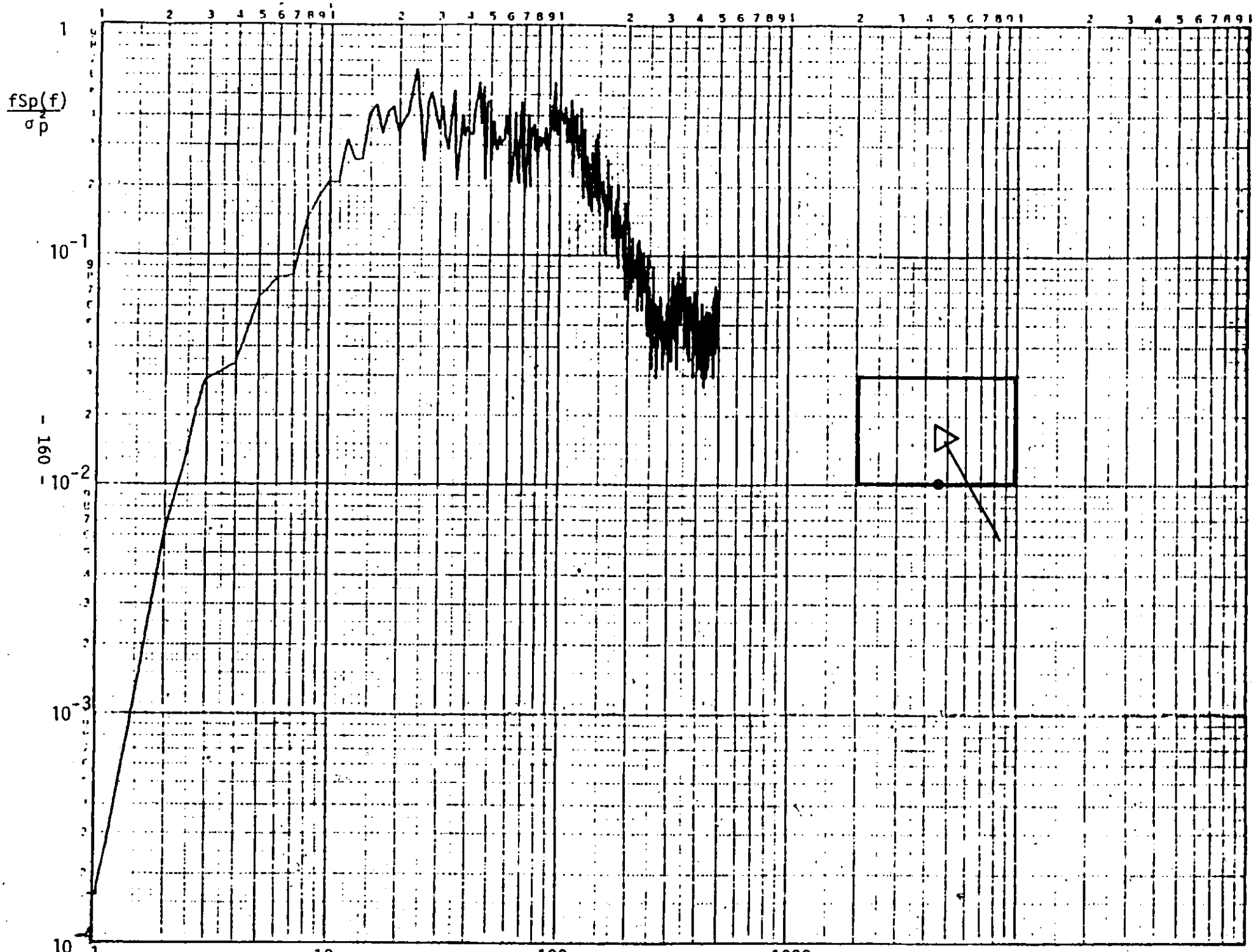

Figure 81. Pressure Spectrum for Tap No. 3, β = 30

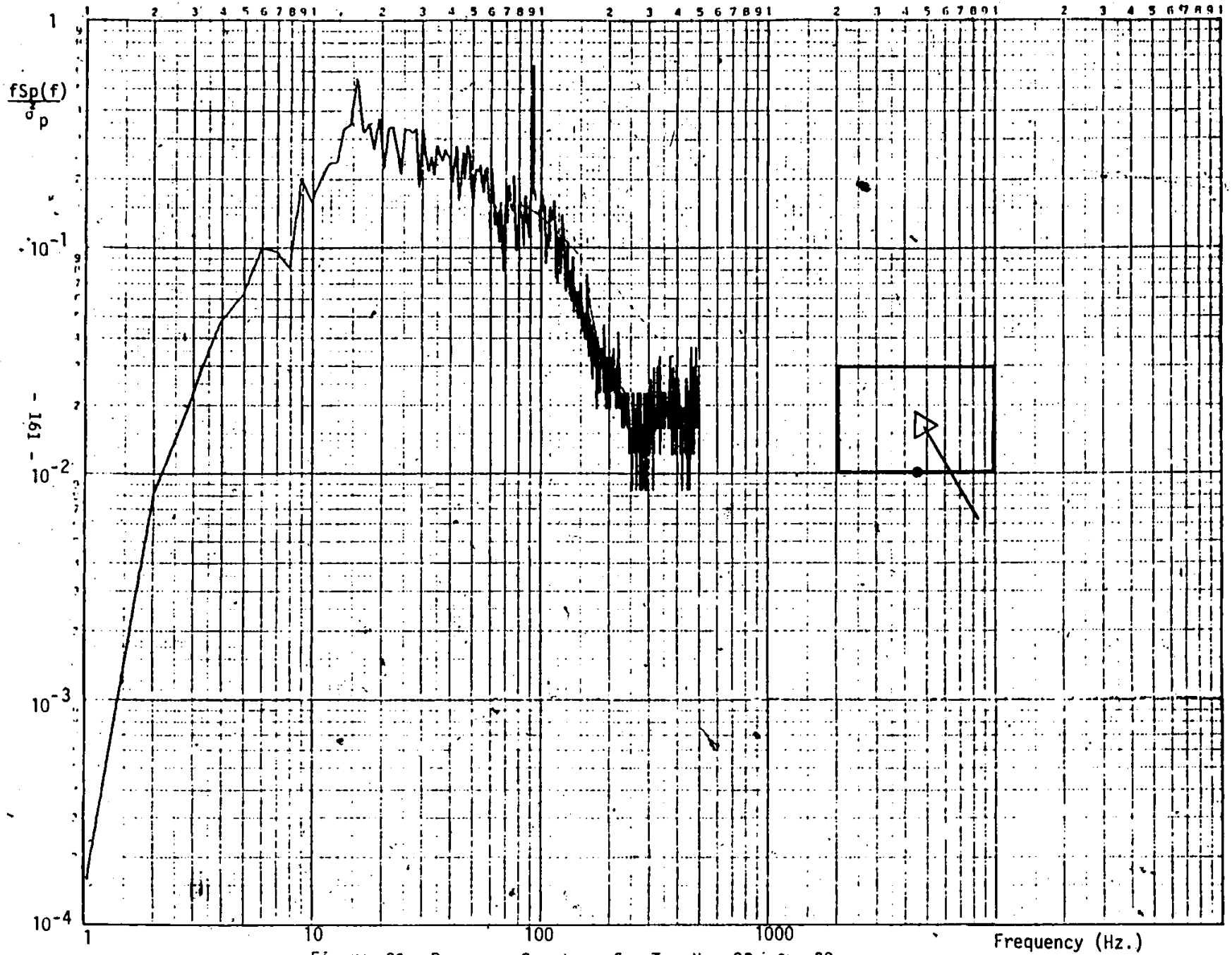

Figure 82. Pressure Spectrum for Tap No. 23, $\beta = 30$.

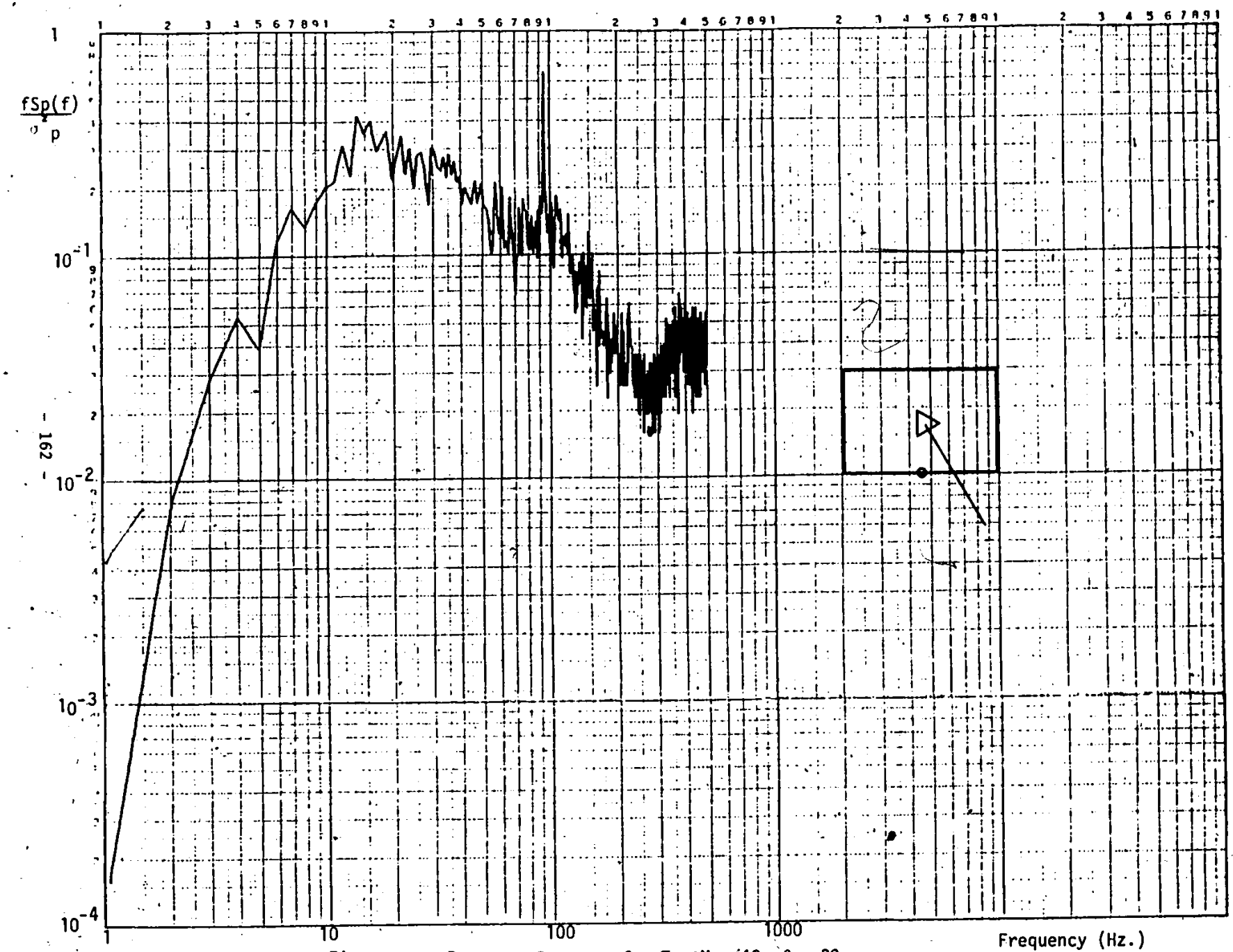

Figure 83. Pressure Spectrum for Tap No. 43, $\beta = 30$.

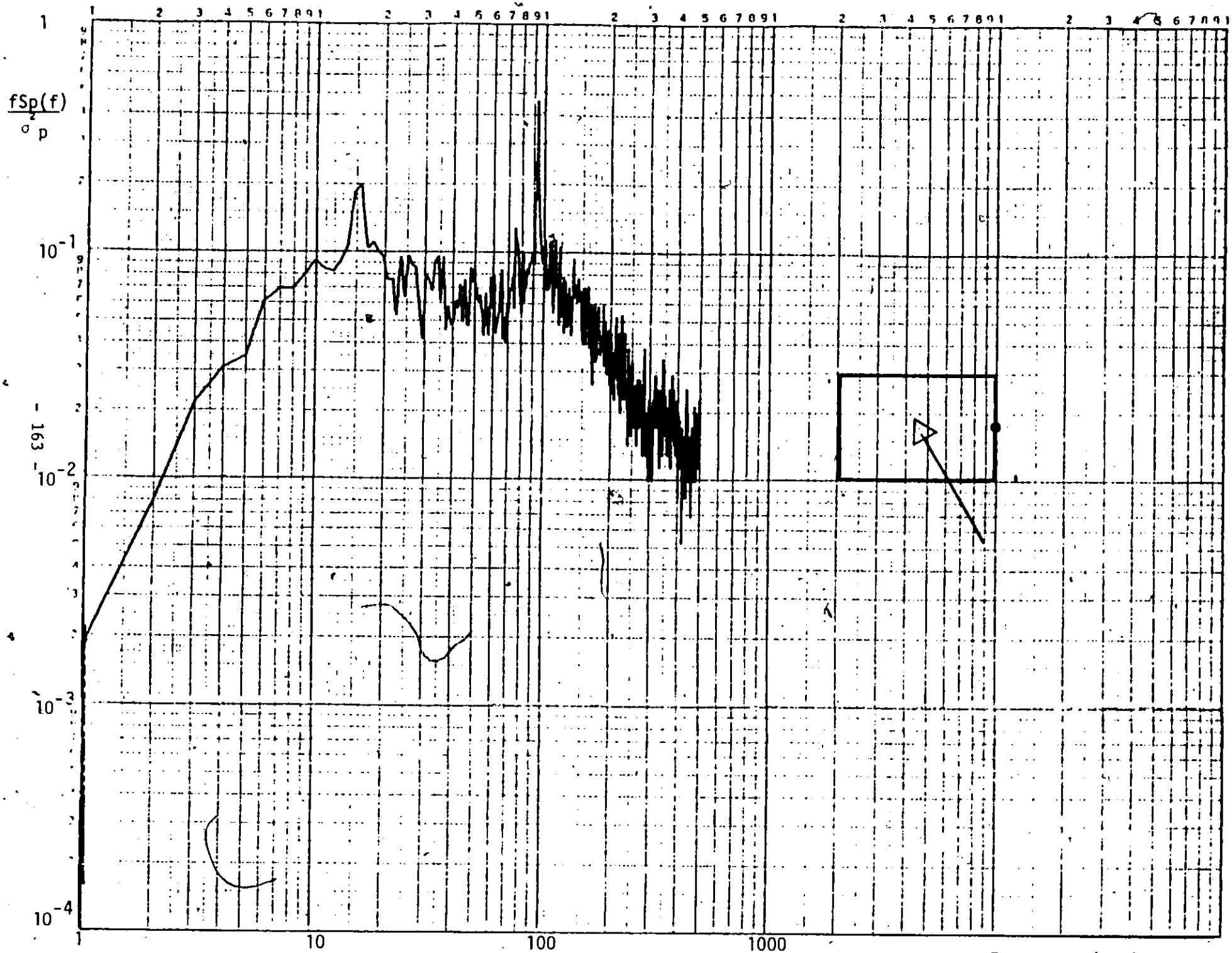

Figure 84. Pressure Spectrum for Tap No. 8, $\beta = 30$.

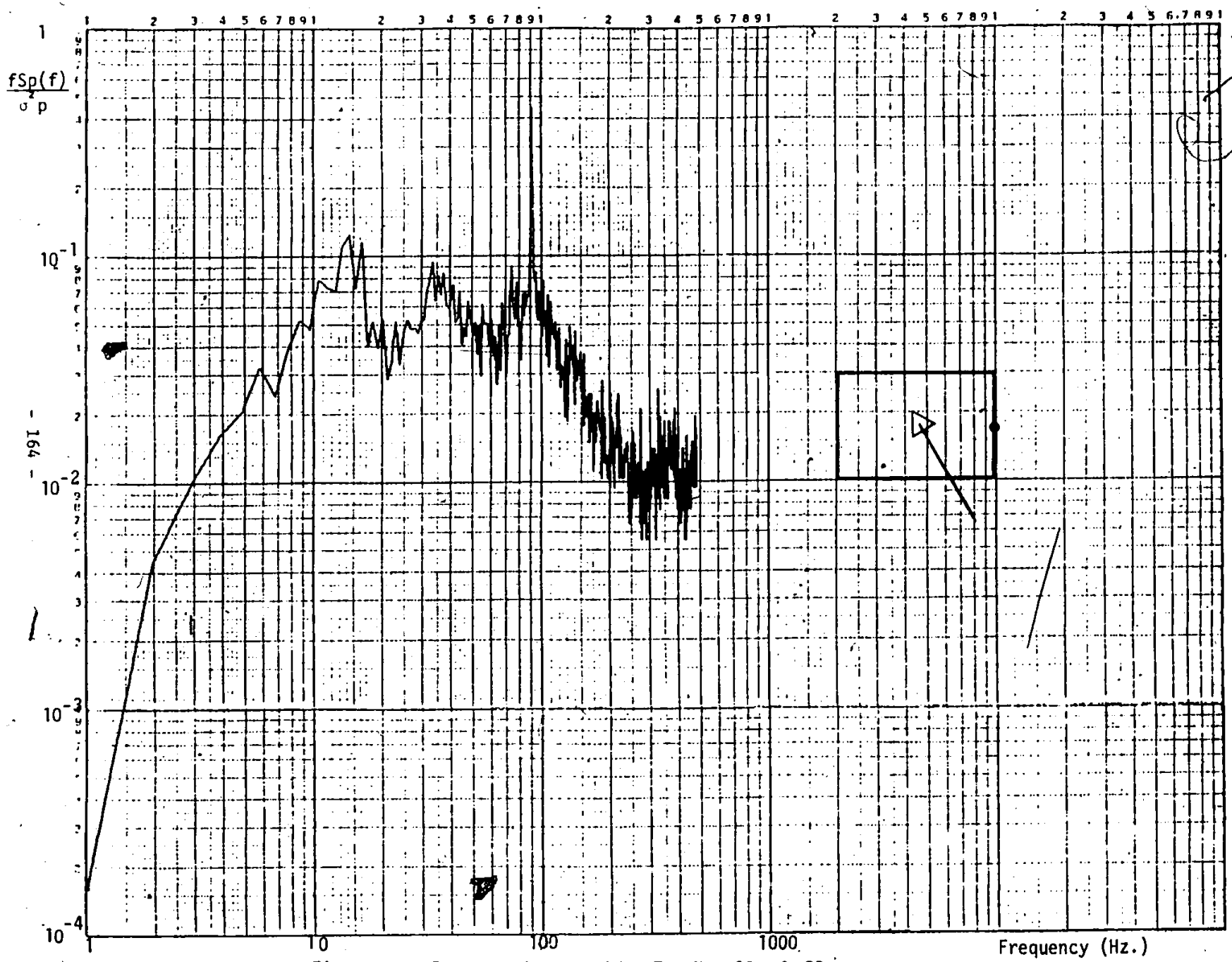

Figure 85. Pressure Spectrum for Tap No. 28, $\beta = 30$.

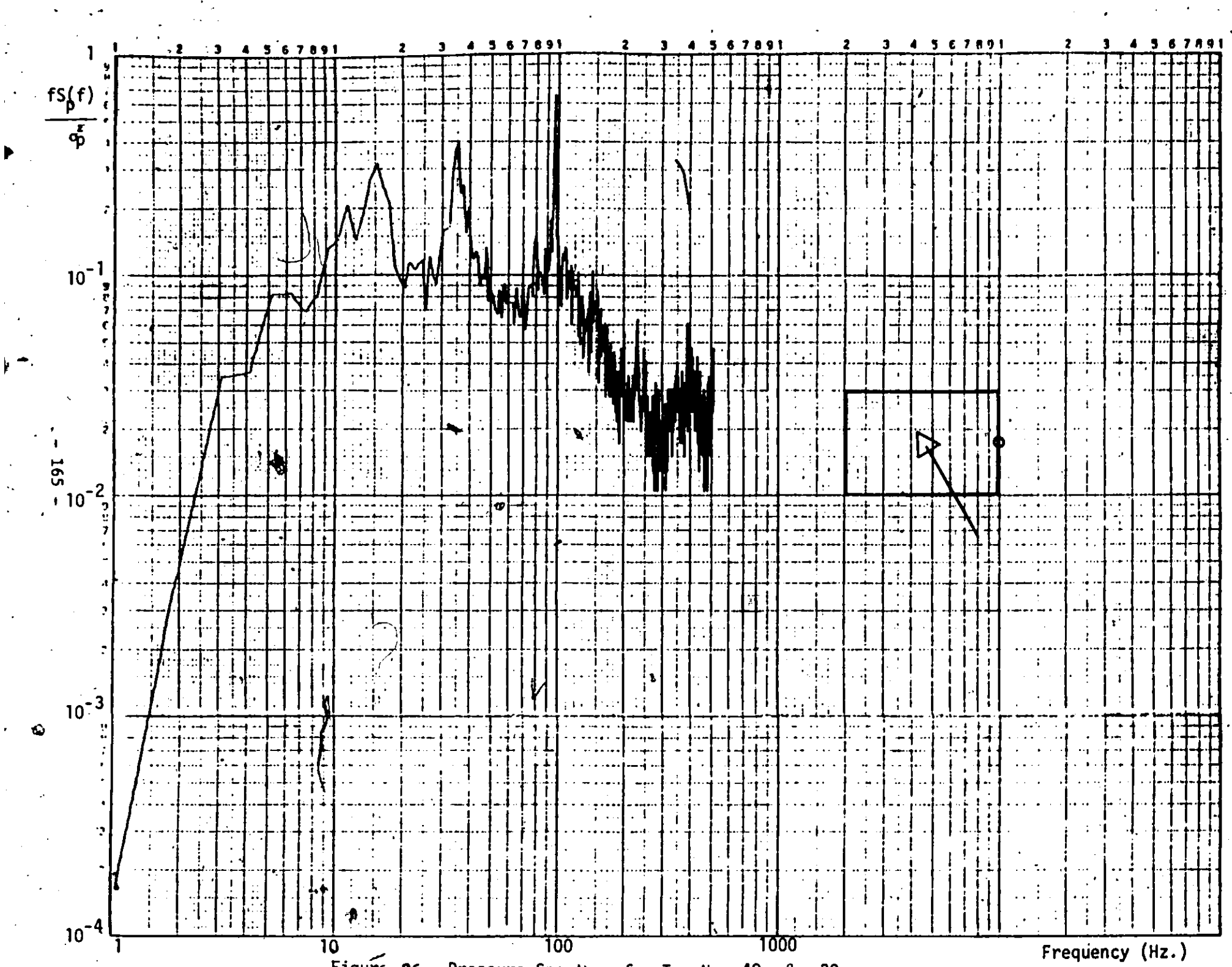

Figure 86. Pressure Spectrum for Tap No. 48, $\beta = 30$.

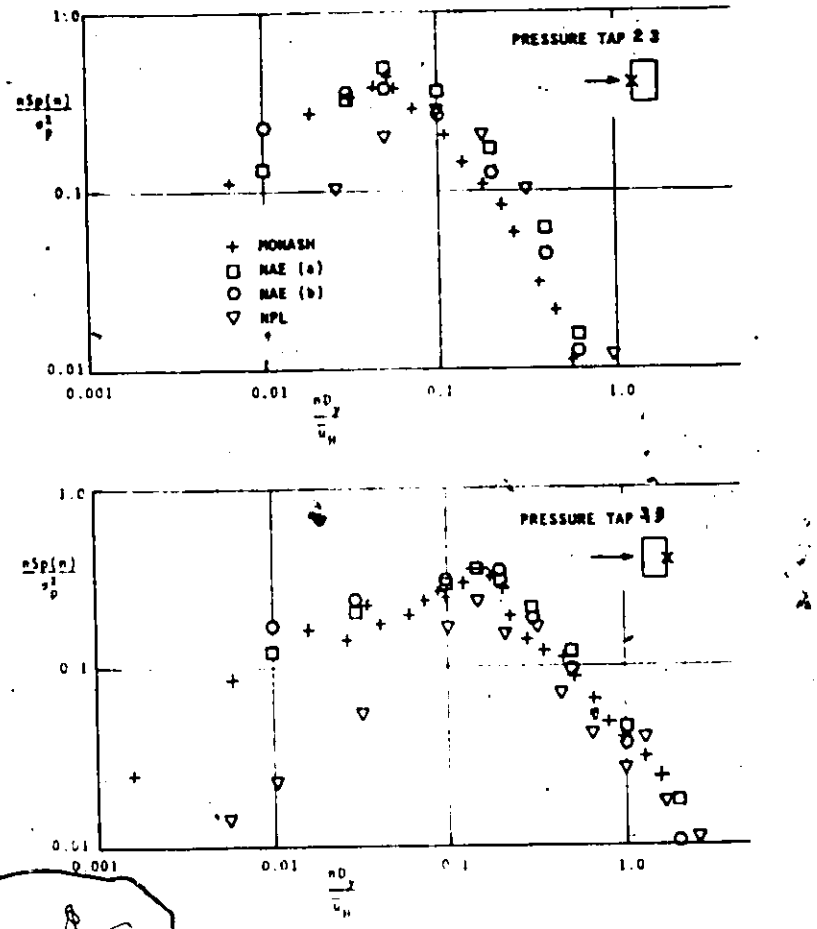

Figure 87. Pressure Spectrum for Taps No. 23 and 33 from Various CAARC Tests, (Ref.11).